Chinese Chemical Letters 36 (2025) 110100

Contents lists available at ScienceDirect

Chinese Chemical Letters

journal homepage: www.elsevier.com/locate/cclet

Recent progress on surface chemistry II: Property and characterization

Xin Li[a,1], Zhen Xu[b,1], Donglei Bu[c], Jinming Cai[d], Huamei Chen[a], Qi Chen[e], Ting Chen[f], Fang Cheng[g], Lifeng Chi[h], Wenjie Dong[a], Zhenchao Dong[i], Shixuan Du[j], Qitang Fan[i], Xing Fan[a], Qiang Fu[k], Song Gao[b], Jing Guo[l], Weijun Guo[m], Yang He[n], Shimin Hou[a], Ying Jiang[o], Huihui Kong[p], Baojun Li[q], Dengyuan Li[r], Jie Li[a], Qing Li[s], Ruoning Li[f], Shuying Li[t], Yuxuan Lin[m], Mengxi Liu[u], Peinian Liu[r], Yanyan Liu[v], Jingtao Lü[w], Chuanxu Ma[i], Haoyang Pan[b], JinLiang Pan[m], Minghu Pan[s], Xiaohui Qiu[u], Ziyong Shen[a], Qiang Sun[x], Shijing Tan[i], Bing Wang[i], Dong Wang[f], Li Wang[y], Lili Wang[z], Tao Wang[aa], Xiang Wang[f], Xingyue Wang[s], Xueyan Wang[a], Yansong Wang[a], Yu Wang[ab], Kai Wu[m], Wei Xu[ac], Na Xue[ad], Linghao Yan[h], Fan Yang[ae], Zhiyong Yang[af], Chi Zhang[ac], Xue Zhang[b], Yang Zhang[i], Yao Zhang[i], Xiong Zhou[m], Junfa Zhu[ag], Yajie Zhang[a,*], Feixue Gao[ah,*], Yongfeng Wang[a,*]

[a] *Center for Carbon-based Electronics and Key Laboratory for the Physics and Chemistry of Nanodevices, School of Electronics, Peking University, Beijing 100871, China*
[b] *Spin-X Institute, School of Microelectronics, South China University of Technology, Guangzhou 511442, China*
[c] *School of Materials and Energy, Guangzhou Key Laboratory of Low-Dimensional Materials and Energy Storage Devices, Guangdong University of Technology, Guangzhou 510006, China*
[d] *Faculty of Materials Science and Engineering, Kunming University of Science and Technology, Kunming 650093, China*
[e] *i-Lab, CAS Key Laboratory of Nanophotonic Materials and Devices, Suzhou Institute of Nano-Tech and Nano-Bionics, Chinese Academy of Sciences, Suzhou 215123, China*
[f] *CAS Key Laboratory of Molecular Nanostructure and Nanotechnology, CAS Research/Education Center for Excellence in Molecular Sciences, Beijing National Laboratory for Molecular Sciences (BNLMS), Institute of Chemistry, Chinese Academy of Sciences, Beijing 100190, China*
[g] *State Key Laboratory for Organic Electronics and Information Displays & Jiangsu Key Laboratory for Biosensors, Institute of Advanced Materials, Jiangsu National Synergetic Innovation Center for Advanced Materials, Nanjing University of Posts and Telecommunications, Nanjing 210023, China*
[h] *Institute of Functional Nano and Soft Materials (FUNSOM), Jiangsu Key Laboratory for Carbon-Based Functional Materials and Devices, Soochow University, Suzhou 215123, China*
[i] *Hefei National Research Center for Physical Sciences at the Microscale and Synergetic Innovation Center of Quantum Information and Quantum Physics, University of Science and Technology of China, Hefei 230026, China*
[j] *Institute of Physics & University of Chinese Academy of Sciences, Beijing 100190, China*
[k] *State Key Laboratory of Catalysis, Dalian Institute of Chemical Physics, Chinese Academy of Sciences, Dalian 116023, China*
[l] *College of Chemistry, Beijing Normal University, Beijing 100875, China*
[m] *Beijing National Laboratory for Molecular Sciences (BNLMS), College of Chemistry and Molecular Engineering, Peking University, Beijing 100871, China*
[n] *School of Material and New Energy, South China Normal University, Shanwei 516600, China*
[o] *International Center for Quantum Materials, Collaborative Innovation Center of Quantum Matter, Interdisciplinary Institute of Light-Element Quantum Materials and Research Center for Light-Element Advanced Materials, School of Physics, Peking University, Beijing 100871, China*
[p] *Herbert Gleiter Institute of Nanoscience, School of Materials Science and Engineering, Nanjing University of Science and Technology, Nanjing 210094, China*
[q] *Research Center of Green Catalysis, College of Chemistry, Zhengzhou University, Zhengzhou 450001, China*
[r] *Key Laboratory for Advanced Materials and Feringa Nobel Prize Scientist Joint Research Center, Frontiers Science Center for Materiobiology and Dynamic Chemistry, State Key Laboratory of Chemical Engineering, School of Chemistry and Molecular Engineering, East China University of Science Technology, Shanghai 200237, China*
[s] *School of Physics and Information Technology, Shaanxi Normal University, Xi'an 710119, China*
[t] *Department of Chemistry, Northeast Normal University, Changchun 130024, China*
[u] *CAS Key Laboratory of Standardization and Measurement for Nanotechnology, National Center for Nanoscience and Technology, Beijing 100190, China*
[v] *College of Science, Henan Agricultural University, Zhengzhou 450002, China*
[w] *School of Physics and Wuhan National High Magnetic Field Center, Huazhong University of Science and Technology, Wuhan 430074, China*
[x] *Materials Genome Institute, Shanghai University, Shanghai 200444, China*
[y] *Department of Physics, School of Physics and Materials Science, Nanchang University, Nanchang 330033, China*
[z] *State Key Laboratory of Low-Dimensional Quantum Physics, Department of Physics, Tsinghua University, Beijing 100084, China*
[aa] *Donostia International Physics Center, Centro de Fisica de Materiales CFM/MPC, CSIC-UPV/EHU, 20018 San Sebastián, Spain*

* Corresponding authors.
E-mail addresses: yjzhang11@pku.edu.cn (Y. Zhang), gaofx@nsfc.gov.cn (F. Gao), yongfengwang@pku.edu.cn (Y. Wang).
[1] These authors contributed equally to this work.

https://doi.org/10.1016/j.cclet.2024.110100

[ab] Institute for Molecular Science, National Institutes of Natural Sciences, Okazaki, Aichi 444-8585, Japan
[ac] Interdisciplinary Materials Research Center, School of Materials Science and Engineering, Tongji University, Shanghai 201804, China
[ad] Tianjin Key Laboratory of Epigenetics for Organ Development of Preterm Infants, Central Laboratory, Tianjin Fifth Central Hospital, Tianjin 300450, China
[ae] School of Physical Science and Technology, Center for Transformative Science, ShanghaiTech University, Shanghai 201210, China
[af] School of Chemical Science, University of Chinese Academy of Sciences (UCAS), Beijing 100049, China
[ag] National Synchrotron Radiation Laboratory, Department of Chemical Physics and Key Laboratory of Surface and Interface Chemistry and Energy Catalysis of Anhui Higher Education Institutes, University of Science and Technology of China, Hefei 230029, China
[ah] Department of Chemical Sciences National Natural Science Foundation of China, Beijing 100085, China

ARTICLE INFO

Article history:
Received 9 February 2024
Revised 2 June 2024
Accepted 6 June 2024
Available online 8 June 2024

Keywords:
Surface chemistry
Scanning probe microscopy
π-Magnetism
Spin qubits
Tip-enhanced Raman spectroscopy

ABSTRACT

Surface with well-defined components and structures possesses unique electronic, magnetic, optical and chemical properties. As a result, surface chemistry research plays a crucial role in various fields such as catalysis, energy, materials, quantum, and microelectronics. Surface science mainly investigates the correspondence between surface property and functionality. Scanning probe microscopy (SPM) techniques are important tools to characterize surface properties because of the capability of atomic-scale imaging, spectroscopy and manipulation at the single-atom level. In this review, we summarize recent advances in surface electronic, magnetic and optical properties characterized mainly by SPM-based methods. We focus on elucidating the π-magnetism in graphene-based nanostructures, construction of spin qubits on surfaces, topology properties of surface organic structures, STM-based light emission, tip-enhanced Raman spectroscopy and integration of machine learning in SPM studies.

1. Introduction

For bulk crystalline materials, atoms or molecules are arranged in a three-dimensional periodic arrangement, exhibiting similar properties. When they are at the surface, the periodicity in the vertical direction is broken, leading to remarkable electronic, magnetic, optical and chemical properties due to changes in the chemical environment. These lead to extensive applications in the fields of chemistry, energy, materials, and microelectronics [1–24]. For the well-defined components and structures, surfaces provide an ideal platform for theoretical investigation, such as first-principles calculations, machine learning-based potential energy surface construction [25–35]. Scanning tunneling microscopy (STM) and atomic-force microscopy (AFM) as well as other scanning probe microscopies (SPM) are powerful tools to characterize surface properties because of the capability of atomic-scale imaging, spectroscopy and manipulation at the single-atom level [36–44]. In this review, we summarize recent advances in surface electronic, magnetic and optical properties characterized mainly by SPM-based methods.

First, magnetic properties of graphene-based nanostructures are summed up. The structures are prepared in the ultra-high vacuum environment through on-surface synthesis. The origin and interaction of π-magnetism in graphene-based nanostructures are characterized by scanning tunneling spectroscopy (STS). In the second part, the construction of spin qubits on surfaces by a combination of electron spin resonance (ESR) and STM are outlined. The basic principle of single-atom ESR and its application in quantum information are described. In the third part, the theoretical and experimental progresses about the topology properties of surface organic structures are introduced. The electronic structures are detected by Angle-resolved Photoemission Spectroscopy (ARPES). In the fourth part, we survey the advances of surface optical properties mainly investigated by STM-based light emission and tip-enhanced Raman spectroscopy (TERS). Finally, we discuss the integration of machine learning in the field of STM-based studies, offering a futuristic outlook on the advancement of surface chemistry research.

2. Magnetic properties of graphene-based nanostructures

Magnetism is fundamental to both current and future spin and quantum technologies [45–47]. The traditional magnetic materials are composed of bulk metals and their oxides, where the unpaired electrons associated with the origin of magnetism are typically from *d* or *f* orbitals [48–51]. Recently, π-magnetism from carbon-based materials has attracted increasing interests [52–54]. Different from metal-based magnetism, carbon magnetism from p orbitals has a number of unique properties like large spin delocalization, weak spin-orbit coupling, long spin relaxation times, and weak decoherence, offering an ideal platform for practical applications in the future, such as quantum information technologies, new optoelectronic devices, and energy applications [55,56]. In addition, because of their highly tunable chemical structures, as represented by graphene-based nanomaterials, *i.e.*, a subtle modification on the structure could give rise to a significant change of the property, the properties of π-magnetic materials are facile to be tailored. However, due to the extremely high reactivity, the synthesis of graphene-based nanomaterials with π-magnetism has been challenging.

The recent developed on-surface synthesis has offered an unprecedented opportunity to fabricate magnetic graphene-based carbon materials [53,57–59]. In contrast to the conventional solution-phase chemistry, the inert ultra-high vacuum (UHV) condition as well as the support of a solid surface in on-surface synthesis could efficiently stabilize the reactive magnetic products. By the rational design of precursor molecules, various π-magnetic carbon materials including magnetic nanographenes, their coupled oligomers and spin chains have been synthesized in atomic precision on solid surfaces and characterized in single-molecule level with the aid of high resolution STM, non-contact AFM (nc-AFM), and STS [52,53]. The fine-tuning of π-magnetism of these structures and a systematic understanding of structure-property relationship has been achieved. Here we introduce the mechanism of π-magnetism and review the recent progress toward the synthesis, characterization, and interpretation of their properties of graphene-based magnetic nanomaterials.

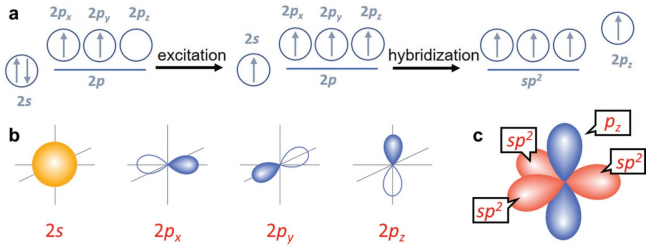

Fig. 1. (a) sp^2 orbital hybridization of carbon atoms in graphene-based nanomaterials. (b) Orbital wavefunctions of carbon atoms. (c) Orbitals of carbon atoms after sp^2 orbital hybridization.

2.1. Orbital hybridization of carbon atoms in graphene-based materials

The orbitals of the outer electrons of a carbon atom are composed of one 2s orbital and three 2p orbitals ($2p_x$, $2p_y$, $2p_z$), where 2s is doubly occupied and one electron is filled in each of $2p_x$ and $2p_y$ while $2p_z$ keeps empty (Figs. 1a and b). In graphene-based materials, these atomic orbitals hybridize into three sp^2 orbitals and one p_z orbital by going through an excitation process and each orbital becomes singly occupied (Figs. 1a and c). The three sp^2 orbitals then couple with other orbitals *via* σ bonds with a so-called "head-to-head" configuration while the p_z orbital forms a π bond with other p_z orbitals with a shoulder-to-shoulder" configuration in graphene-based structures. However, in some particular cases, driven by sublattice imbalance, topological frustration, *etc.*, the electrons in some p_z orbitals could not be paired, leading to the generation of singly occupied orbitals thus introducing π-magnetism into graphene-based materials.

2.2. Characterization of π-magnetism by STS

Similar as the conventional wet chemistry, products in on-surface synthesis are typically not homogenous, thus averaging measurement techniques for the characterization of π-magnetism of carbon nanomaterials are usually lack of precision. Therefore, SPM/STS techniques become the most popular and efficient methods for the accurate characterization of π-magnetism in single-molecule level [53]. The simultaneous measurements of different structurally similar magnetic products/byproducts on a sample in turn offer a platform for fundamental understanding of structure-property relationship of magnetic carbon nanostructures [60,61]. To data, the most widely used magnetic fingerprints in magnetic graphene-based nanomaterials are the detection of singly occupied/unoccupied molecular orbitals (SOMO/SUMO), spin excitation exchange, and Kondo resonance.

2.2.1. Singly occupied/unoccupied molecular orbitals

As mentioned above, the magnetism of graphene-based nanomaterials is contributed by unpaired p_z electrons and each unpaired electron occupies a molecular orbital, *i.e.*, SOMO. An example is shown in Fig. 2. The molecule named as Clar goblet is a well-known magnetic nanographene (the origin of magnetism will be discussed in the later section), holding two unpaired p_z spin electrons with different spin signs (Fig. 2a) [62]. Without the consideration of electron-electron interactions, each unpaired p_z spin electron would form a zero-energy state at Fermi level. However, due to electron-electron interactions, for each unpaired p_z spin electron, SOMO and SUMO are generated and gapped through on-site Coulomb repulsion U, as shown in Fig. 2a. Because only one electron is allowed to occupy in SOMO, when injecting a second electron into the SOMO, the second electron would suffer the Coulomb repulsion U from the first electron so that it will stay in SUMO at an energy U above SOMO.

Since SOMO and SUMO are originally from a same singly occupied molecular orbital, thus similar spatial distributions of the two orbitals were resolved in associated dI/dV maps, which are also in perfect match with the calculated density of states (DOS) distributions, as shown in Fig. 2b. The Coulomb gap between SOMOs and SUMOs in Clar goblet is thus determined as 1.3 eV. Note that several parameters could impact on the magnitude of Coulomb repulsion as represented by screening potential of the substrate and delocalization of electron states. Firstly, magnetic states in a molecule adsorbing on metal surfaces exhibit a smaller Coulomb gap than the same molecule adsorbing on a dielectric layer [63]. Secondly, a larger spatial electron delocalization of the SOMO will lower the Coulomb repulsion when a second electron is filled, resulting in a smaller Coulomb gap [64].

2.2.2. Spin-flip excitation

For a spin system holding more than one spin electron, spin exchange couplings from the ground state to excited states are involved. When the energy of the tunneling electron of STM is higher than the exchange energy between the ground state and corresponding excited state of the structure, the system can be excited to excited states. The inelastic spin-flip excitation process brings in additional inelastic tunneling channels from the tip to the sample, apart from the conventional elastic channel. This leads to the appearance of steps symmetrically around the Fermi level in dI/dV spectrum and peaks antisymmetrically around the Fermi level in d^2I/dV^2 spectrum, where the energy positions of steps/peaks correspond to the excitation energies. An example is given in Fig. 2c. Again for the Clar goblet molecule, an exchange energy of 23 meV is resolved in both dI/dV and d^2I/dV^2 spectra, corresponding to the spin-flip excitation from the singlet ground state to the excite triplet state [62]. The dI/dV spin excitation maps obtained at $\pm$ 23 mV matched perfectly with the DOS distribution of SOMO, indicating the origin of spin excitation is the singly occupied orbitals.

The energy of spin exchange interaction J in a two-spin system is given by the following Eq. 1, where ϕ_1 and ϕ_2 indicate the spatial wavefunctions of the magnetic states, r_{12} is the distance between the magnetic states and other parameters are a constant. Therefore, J is determined by the wavefunctions of the two magnetic states themselves as well as the overlap between them. This implies the spin exchange energy can be fine-tuned by modifying the associated magnetic states or their wavefunction overlaps, which will be discussed in later sections.

$$J = \int \phi_1^*(r_1)\phi_2^*(r_2)\frac{e^2}{4\pi\varepsilon_0 r_{12}}\phi_1(r_1)\phi_2(r_2)dr_1dr_2 \quad (1)$$

2.2.3. Kondo resonance

Apart from the spin exchange interaction between radical states in a magnetic carbon-based molecule and extended nanostructures, the exchange could also happen between the molecular magnetic states and the conduction electrons on a metallic substrate, which is called Kondo resonance [65,66]. The classical Kondo resonance refers to the spin interaction between a local $S = 1/2$ spin and conduction electrons of the metal surface. Quantum mechanically the magnetic state could either populate an empty state of the metallic substrate, or accept a second electron from the metal, in a limited time in the range of femtoseconds. After relaxing, the SOMO could have a magnetic state occupied by a single electron with a reversed spin. Such spin fluctuation of the molecular spin together with all these events of spin exchange interactions give rise to the appearance of a Kondo resonance symmetrically around the Fermi energy.

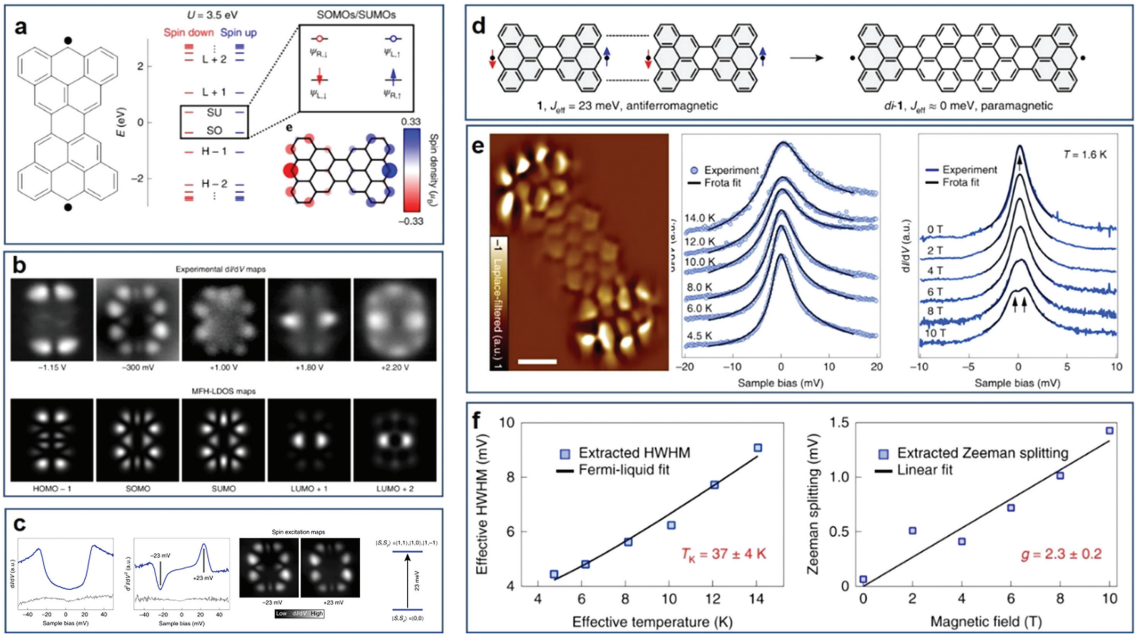

Fig. 2. (a) The chemical structure of the magnetic molecule named as Clar goblet, together with its orbital energy alignment and spin distribution. (b) Experimentally obtained and theoretically simulated frontier molecular orbitals of Clar goblet. (c) Low-energy STS showing spin excitation between singlet ground state and triplet excited states, along with the d*I*/d*V* maps measured at the exchange energy extracted from the spectra. (d) The chemical structure of the paramagnetic Clar goblet dimer obtained by the fusion of two monomers. (e) Temperature evolution and magnetic field evolution of Kondo resonances obtained on a Clar goblet dimer. (f) Left: extracted half-width at half-maximum (HWHM) of the Kondo resonance as a function of temperature, fitted by the Fermi-liquid model. A Kondo temperature $T_K = 37 \pm 4$ K is obtained from the fit; Right: extracted Zeeman splitting of the Kondo resonance as a function of magnetic field, fitted by a corresponding linear function. A Landé factor $g = 2.3 \pm 0.2$ is obtained from the fitting. Reproduced with permission [62]. Copyright 2019, Springer Nature.

The spectra of Kondo resonances can be fitted by a Frota function then the half-width at half-maximum (HWHM) can be extracted [67]. As one of the characteristic features, Kondo peaks show anomalous broadening with increasing temperature, and the trend can be described by the Fermi-liquid model, thus HWHMs extracted from Kondo peaks obtained at different temperatures eventually provide the Kondo temperature of the single spin impurity. The detailed related equations can be found [62]. Another typical fingerprint of Kondo peak is its response to a magnetic field. A Zeeman splitting of the Kondo resonance becomes observable at sufficiently strong magnetic fields [62,68].

In the example shown in Figs. 2d and e, Clar goblet dimer generated from the fusion of two monomers is paramagnetic, since the exchange coupling strength between the radical is near zero due to the large spatial distance [62]. Kondo resonance around the Fermi level was thereof resolved, as evidenced by the width broadening with temperature increasing and peak splitting in a sufficiently strong magnetic field. A Kondo temperature of 37 K and Landé factor of 2.3 were obtained from corresponding fittings (Fig. 2f). The paramagnetic character of Clar goblet dimer was also corroborated by the disappearance of the symmetric steps from exchange excitation around Fermi level as detected in Clar goblet monomer, demonstrating that no effective exchange between the two radical states locating at two sides of the dimer is involved.

Apart from the classical screened Kondo effect for the system including only an $S = 1/2$ spin impurity, an underscreened Kondo resonance with a total local spin $S \geq 1$ was also reported to be possible although the underlying mechanism is more complex [68–70]. According to various previous studies, in graphene-based magnetic nanostructures, underscreened Kondo resonances typically exhibit lower intensity and the peak splitting appears at a weaker magnetic field than those of a $S = 1/2$ counterparts. These fingerprints in STS of high-spin systems allow for differentiating them from $S = 1/2$ magnetic systems. This is particularly important when spin-flip excitations (*e.g.,* from ferromagnetic $S = 1$ to antiferromagnetic $S = 0$) are not visible in STS, either because they are too weak or the exchange energy is too high which falls into the range of molecular orbital thus cannot be resolved (inelastic tunneling is much weaker than elastic tunneling). An example showing the synthesis and characterization of nanographene **3** is presented in Fig. 3 [68]. In this example, a 2H-passivated intermediate was firstly observed on the sample, *i.e.*, **3** is passivated by two hydrogen atoms. Note that such hydrogen passivation for reactive species is common in the preparation of magnetic graphene-based nanostructures *via* on-surface synthesis. Tip induced dehydrogenation was then performed, hierarchically generating intermediate product **2** with one H passivation and final fully sp^2 hybridized product **3**. According to the associated chemical structures and calculated spin density distributions, **1** is supposed to be closed-shell; **2** holds a spin of 1/2, and **3** is an $S = 1$ system. Using a same STM tip, the d*I*/d*V* spectra obtained on these three molecules reveal that **1** has no decent signal; **2** and **3** both exhibit Kondo resonances whereas the intensity of Kondo peak on **2** is much stronger than that on **3**, implying **2** shows a fully screened Kondo effect ($S = 1/2$) while **3** presents an underscreened Kondo effect ($S = 1$), as shown in Fig. 3g. In addition, the $S = 1$ system of **3** shows an obvious Zeeman splitting of the Kondo resonance with magnetic field at 2.5 T, while no splitting is observable in the $S = 1/2$ system of **2** (Fig. 3h). In fact, according to related studies, the Kondo resonance of a $S = 1/2$ system splits linearly with magnetic fields only above a strong magnetic field $B \geq 0.5 k_B T_K / g\mu_B$, while an underscreened $S = 1$ system could conserve some magnetic moment, and its zero-bias resonance starts splitting already once $B > 0$ [71–74].

The fabrication of magnetic graphene-based nanomaterials *via* on-surface synthesis approach have been performed mostly on the Au(111) surface, due to the relatively weak charge transfer at the interface and weak hybridization between magnetic states and surface states, thus stabilizing and protecting the reactive radical states. In contrast, on more reactive and low-work-function sub-

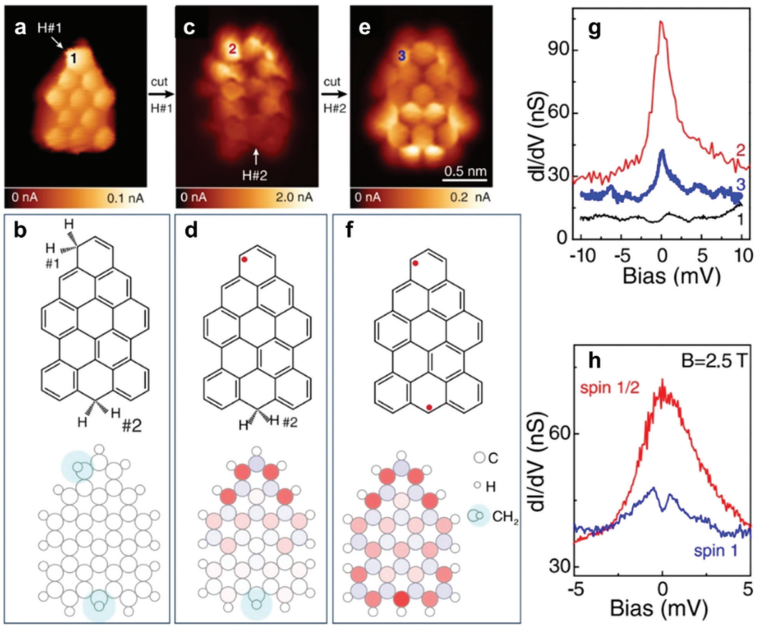

Fig. 3. (a, c, e) BRSTM images of 2H-, H-, passivated and fully sp^2-nanographenes, as marked by 1, 2, 3, respectively. (b, d, f) Corresponding chemical structures and spin distributions of the products shown in (a), (c), and (e), respectively. (g) d*I*/d*V* spectra obtained on 1, 2, 3, respectively. (h) Zeeman splitting of the Kondo resonance under a magnetic field at 2.5 T for $S=1/2$ system of molecule 2 and $S=1$ system of molecule 3. Reproduced with permission [68]. Copyright 2020, American Physical Society.

strates, such as Ag(111) and Cu(111), which were also widely used as the substrates in on-surface synthesis [58,75–80], electrons from the substrates usually transferred to the magnetic molecules [81–83], occupying the SOMO orbitals then quenching radicals. Once the radical states are quenched, the total spin of the molecule becomes to be zero, exhibiting no magnetic properties. Therefore, the majority of examples of magnetic graphene-based nanostructures shown below have been prepared on Au(111).

2.3. Origin of π-magnetism

π-Magnetism in carbon-based materials appears due to the generation of singly occupied p_z orbitals as already discussed above. The generation of unpaired p_z is attributed to several origins. They can be classified as following aspects: sublattice imbalance, topological frustration, Coulomb repulsion induced spin polarization, non-hexagonal ring integration, heteroatom doping, charge transfer, and topological end states.

2.3.1. Sublattice imbalance

Graphene-based structures are bipartite system where sp^2-hybridized carbon atoms are aligned in two alternating hexagonal sublattices. Carbon atoms in one sublattice can only covalently couple with carbon atoms of the opposite sublattice, indicating that p_z electrons in carbon atoms belonging to different sublattice have opposite spin sign. Consequently, if the two sublattices have a different number of carbon atoms in a graphene-based nanostructure, the total p_z electrons are impossible to completely bind pairwise. The electrons which do not couple with other carbon atoms become to be π-radicals with a spin of $S=1/2$. The total net spin in the ground state of a graphene-based bipartite system is described by Lieb's theorem: $S=|N_A-N_B|/2$, where N_A and N_B are the number of carbon atoms belonging to each sublattice [89].

The most well-known and studied case showing π-magnetism due to sublattice imbalance is triangulene systems. Trianguene molecule is a kind of nanographene with triangular shape holding three zigzag edges. Such particular topology makes the sublattices of triangulenes imbalanced. In Fig. 4 it displays a series of triangulenes with different sizes obtained by on-surface synthesis so far. While the smallest [2]triangulene (2T) has a single spin of $S=1/2$, other larger triangulenes are all high-spin systems whose net spins can be calculated by Lieb's theorem, as shown in Fig. 4b. The synthetic methods in on-surface synthesis for the production of triangulenes typically include annealing procedure and tip manipulation. A well-designed precursor is used for the former and the final products are formed *via* cyclodehydrogenation reaction. For the latter a bias pulse induced removal of additional hydrogen or oxygen atoms has turned out to be efficient to generate a globally sp^2-hybridized triangulene product, by using a hydrogen or oxygen substituted molecule as the precursor to stabilize it in solution-phase synthesis. In addition, the tip manipulation approach requires no catalytic performance of the substrate which can be conducted on insulating surfaces [63,84], avoiding the screening and hybridization side effect of a metal substrate during the characterization of electron and magnetic properties.

The characterization of the electronic properties of 2T is displayed in Fig. 4c [88]. Because 2T has one unpaired p_z electron, its molecular orbital includes one SOMO and one SUMO, which were clearly resolved in d*I*/d*V* spectrum and associated DOS mapping. The DOS of SOMO and SUMO exhibit similar feature, indicating their same origin, *i.e.*, splitting from a same zero-energy orbital by Coulomb repulsion. In Fig. 4d it shows the comparison of the Kondo resonances between 2T and 3T. Accordingly, with a same probe, the signal on 2T has a much stronger intensity than that on 3T, demonstrating that 2T is an $S=1/2$ system with a screened Kondo effect while 3T has a net spin of $S=1$ with an underscreened Kondo effect. It is worth noting that other than 2T and 3T, Kondo resonance on larger triangulenes have not been observed experimentally, presumably due to their higher net spins [84–87]. In addition, spin excitation steps from the ground states to excited states, as widely reported in some other π-magnetic systems, have not been resolved for all triangulenes in experiments. This is because the exchange energies of triangulenes are typically very large [90], falling in the range of frontier molecular orbitals. Since the signal of the inelastic tunneling is much weaker than the elastic

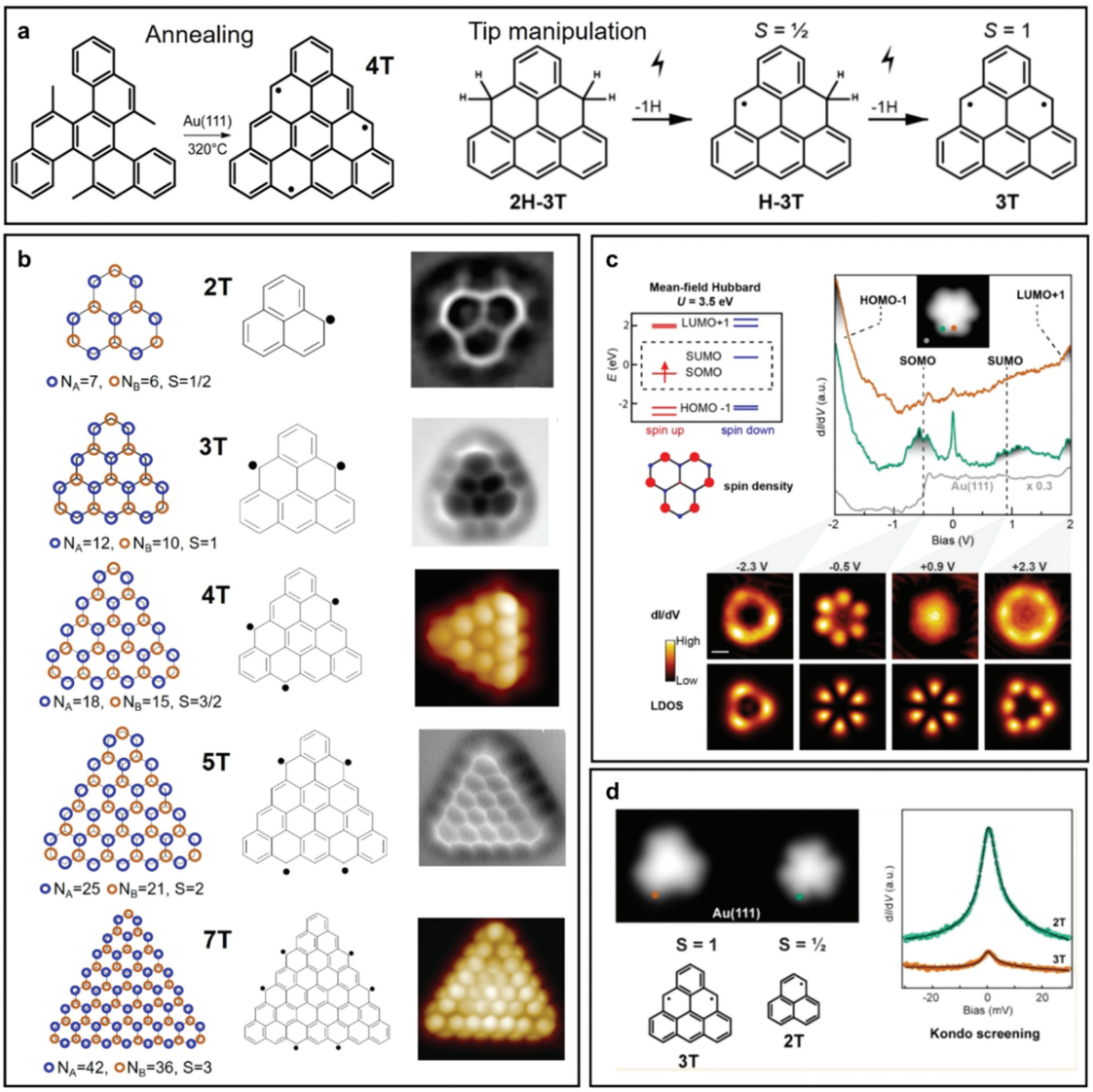

Fig. 4. (a) Typical synthetic methods for the synthesis of triangulenes on surfaces. (b) A series of triangulenes with different sizes obtained by on-surface synthesis approach. The sublattices of these triangulenes are marked in blue and red, together with their net spins as calculated by Lieb's theorem $S=|N_A-N_B|/2$. The chemical structures and the corresponding bond-resolving (BR)-STM or nc-AFM images are displayed in the right side. (c) Molecular orbital alignment, experimental dI/dV spectra and corresponding DOS obtained experimentally/simulated theoretically of [2]triangulene (2T). (d) The comparison of Kondo resonances obtained on 2T and 3T on Au(111). Reproduced with permission [84–88]. Copyright 2019, American Chemical Society; Copyright 2017, Springer Nature; Copyright 2019, CC-BY-NC 4.0; Copyright 2021, Royal Society of Chemistry; Copyright 2023, CC-BY 4.0.

tunneling, the exchange steps are probably overlaid by the signals of frontier molecular orbitals. Therefore, the detection of SOMOs and SUMOs, along with the associated theoretical calculations, has been treated as the proof of π-magnetism of large triangulenes.

Several trianguelene derivatives holding a high spin have also been successfully synthesized on surfaces, which have a similar sublattice imbalance character as trianguelenes thus following Lieb's theorem. Three examples are shown in Fig. 5. Firstly, a porous [7]triangulene, *i.e.*, [7]triangulene quantum rings ([7]TQR), were fabricated with the combination of in-solution and on-surface synthesis (Fig. 5a) [91]. [7]TQR has a same number of unpaired electrons as [7]triangulene, although six carbon atoms in the center are missing, exhibiting similar electronic properties as [7]triangulene. Secondly, two extended [3]trianguelene derivatives **1** and **2** were obtained on Au(111), as shown in Fig. 5b [68]. According to Lieb's theorem, the symmetric molecule **2** has a same number of spin-up and spin-down electrons, which is thus closed-shell ($S=0$). In contrast, the asymmetric molecule **1** shows spin imbalance with a net spin $S=1$. The conclusion is supported by the STS measurement, where an underscreened Kondo resonance was resolved in **1** while no signal appeared in **2**. Thirdly, heptauthrene, which can be thought as the combination of two [2]trianguelenes linked by a phenyl ring, were synthesized on Au(111) [69]. Because of the spin imbalance, it exhibits a net spin of $S=1$. This was corroborated by the magnetic field dependent Kondo peak splitting experimentally. A relatively weak magnetic field of 3T already apparently splits the undercreened Kondo resonance into two peaks, indicative of its high spin character. The tip manipulation experiments on the hydrogen passivated intermediate (H-heptauthrene) and sp^2-hybridized heptauthrene further support this conclusion, in which the Kondo resonance of H-heptauthrene ($S=1/2$) is much stronger than heptauthrene ($S=1$).

2.3.2. Topological frustration

In the cases of some nanographenes with a special topology, in which the sublattice is balanced but it is still impossible to find a

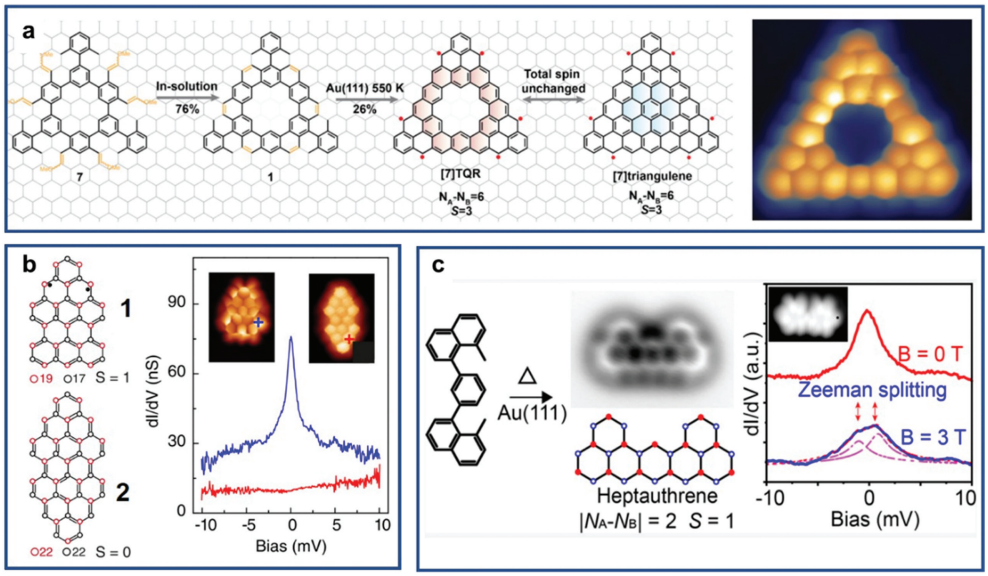

Fig. 5. (a) The synthesis of porous [7]triangulene, *i.e.*, [7]triangulene quantum rings ([7]TQR), and the BRSTM image of the product [91]. (b) Left: two extended [3]triangulene derivatives, along with their chemical structures, sublattice counting, and the associated net spins. Right: BRSTM images and Kondo resonances of the two extended [3]trianguelene derivatives [68]. (c) Left: the synthesis of heptauthrene, along with the nc-AFM image and its sublattice counting and the associated net spins. Right: the splitting of Kondo resonance of heptauthrene in a magnetic field of 3T [69]. Reproduced with permission [68,69,91]. Copyright 2020, 2021, American Chemical Society; Copyright 2020, American Physical Society.

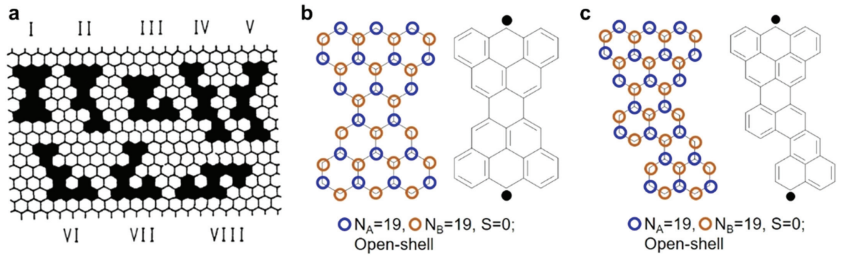

Fig. 6. (a) Smallest structures (in black) composed of eleven hexagons showing topological frustration. (b, c) Sublattice counting and chemical structure of (b) Clar goblet and (c) molecule II as shown in (a). Reproduced with permission [92]. Copyright 1990, Springer Nature.

way to draw a Kekulé structure [92,93]. Unpaired p_z electrons are necessarily included in corresponding chemical structures. Such effect as an origin of π-magnetism is called topological frustration. The smallest magnetic nanographenes originating from topological frustration was predicted to be composed of eleven hexagons, with eight different arrangement of hexagons, as displayed in Fig. 6a [92]. Clar goblet as already discussed above is the only π-magnetic nanographene synthesized to date [62], in which the amount of atoms belonging to different sublattice are both ninety, thus the net spin is zero according to Lieb's theorem (Fig. 6b). This implies the ground state of Clar goblet is either closed-shell or antiferromagnetic (open-shell). Since it is not possible to draw a closed-shell Kekulé structure, Clar goblet should have an antiferromagnetic ground state, which was confirmed by experiments. As revealed in Fig. 2, the magnetic fingerprint of spin excitation steps was observed. Other examples of magnetic graphene-based structures composed of eleven hexagons with the origin of topological frustration have not been achieved experimentally. As a prediction, we expect that, although the amount of atoms belonging to each sublattice and the ground state should be the same as Clar goblet (Fig. 6c), they are mostly asymmetric thus are expected to have different magnetic properties as Clar goblet. For instance, they may hold more localized spin density which in turn probably tunes the spin exchange energy.

2.3.3. Coulomb repulsion induced spin polarization

In fact, in most magnetic graphene structures, sublattices are balanced and no topological frustration is involved. In these cases, two resonance structures, *i.e.*, both closed and open-shell structures could be drawn (Fig. 7d). The structure exhibits magnetic character only when the open-shell resonance counterpart is energetically more favorable. The ground state is determined by the competition between hybridization energy and electrostatic Coulomb repulsion between valence electrons, where the former is responsible for the formation of HOMO and LUMO, leading to a closed-shell ground state (non-magnetic), while the latter promotes the formation of SOMOs associated with an open-shell ground state (magnetic). The open-shell ground state typically prevails in graphene structures holding rich zigzag edges [94,95]. These structures have a relatively low energy gap which can be even smaller than the Coulomb repulsion between two valence electrons in a frontier molecular orbital. Consequently, the HOMO will split into two SOMOs, thus generating net spins. One of the pioneering works is shown in Figs. 7a-c [74]. In this example, three (3,1) chiral graphene nanoribbons fused together forming junctions holding rich zigzag edges upon a high temperature annealing. The energetically symmetric steps in dI/dV spectra in Fig. 7b originate from the spin-flip excitation from $S=0$ to $S=1$, thus revealing an antiferromagnetic ground state of the junction. The low-energy

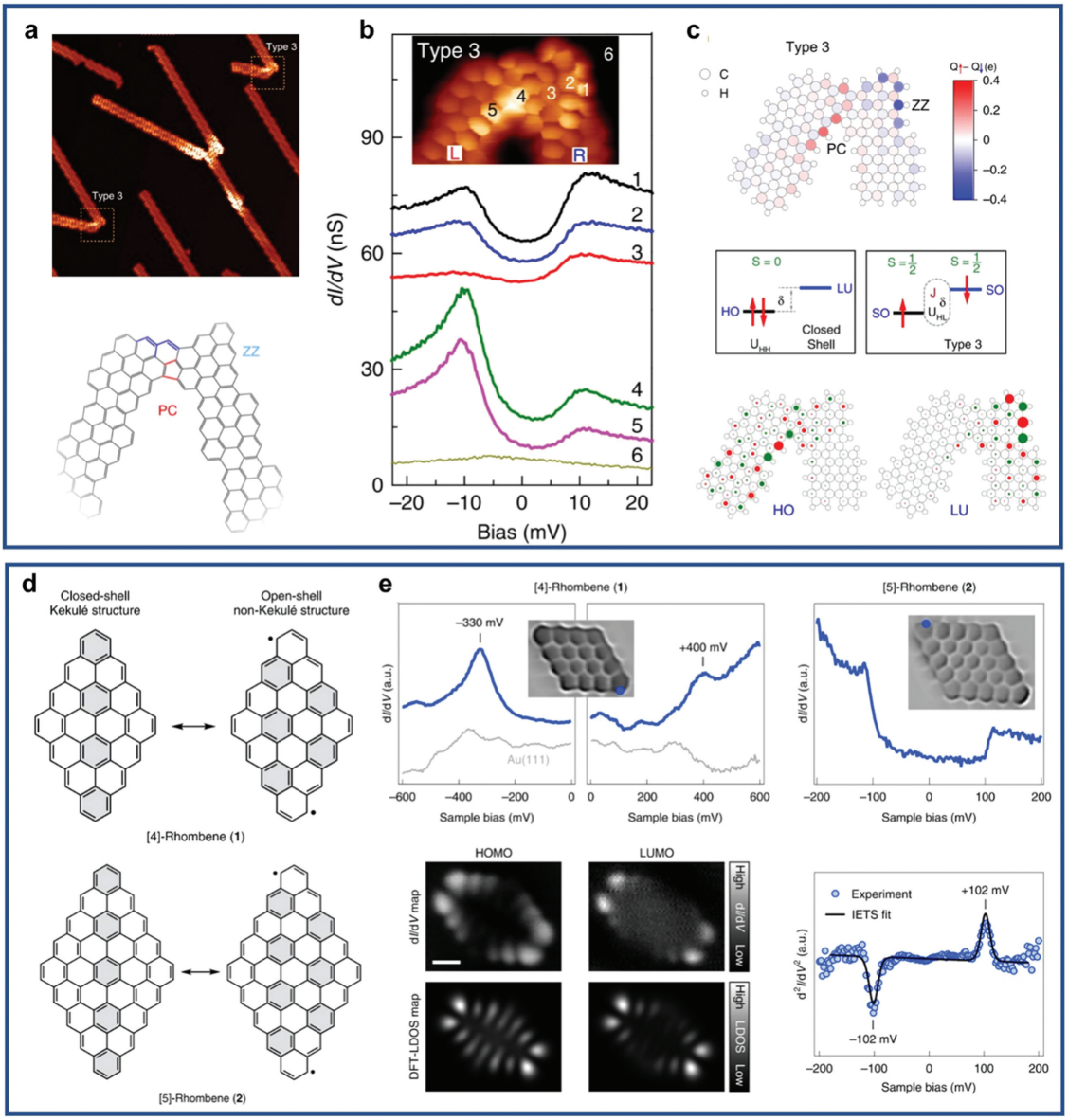

Fig. 7. (a) STM image and corresponding chemical structure of a junction formed between chiral graphene nanoribbons. (b) STS showing spin flip excitation of the electrons of the junction. (c) DFT calculated spin density distribution and the spin polarization of HOMO into SOMOs, as well as the electron localization of HOMO and LUMO. (d) Resonance structures between closed-shell and open-shell structures of [4]rhombene and [5]rhombene. (e) d*I*/d*V* spectra obtained on [4]rhombene and [5]rhombene, along with HOMO/LUMO mapping of [4]rhombene and d^2I/dV^2 spectrum of [5]rhombene associated with the spin exchange excitation. Reproduced with permission [74,94]. Copyright 2021, Springer Nature; Copyright 2019, CC-BY 4.0.

magnetic fingerprint was actually reflected by the bright contrast in the BRSTM image shown in Fig. 7a which was obtained at a low bias of 2 mV. As displayed in Fig. 7c, both HOMO and LUMO orbitals exhibit very localized electron DOS distribution, leading to a large Coulomb repulsion *U*. Once the *U* exceeds the HOMO-LUMO gap, the two electrons in HOMO find a lower-energy configuration by occupying each a different, spatially separated state, *i.e.*, SOMO. These generated two magnetic states are spin-polarized and exchange coupled antiferromagnetically, as illustrated in Fig. 7c.

Another outstanding example is rhombus-shaped nanographenes with zigzag periphery, where the closed-/open-shell ground state were precisely tailored by the design of size [94]. As shown in Fig. 7d, for both [4]rhombene and [5]rhombene, two resonance structures can be drawn. However, according to STS in Fig. 7e, the ground state of [4]rhombene turned out to be closed-shell where the DOS mappings are attributed to its HOMO and LUMO. In contrast, the symmetric steps and antisymmetric step in d*I*/d*V* and d^2I/dV^2 spectra of [5]rhombene are indicative of its antiferromagnetic ground state with a large exchange energy of 102 mV. The smaller [4]rhombene has a larger hybridization energy and energy gap, thus the Coulomb repulsion between valence electrons is not sufficient to excite the electrons into singly occupied orbitals. However, once the electron conjugation becomes higher, as in [5]rhombene, the energy gap diminishes, thus the Coulomb repulsion is large enough to overcome the energy gap and spin polarization occurs.

2.3.3.1. Counting rule. We propose an empirical counting rule to judge the ground state of a graphene-based nanostructure (closed shell *vs.* open-shell) balanced between Coulomb repulsion and orbital hybridization, where two resonance forms are involved. A closed-shell form is associated with a Kekulé structure and the open-shell form corresponds to a Clar form. For a polyaromatic hydrocarbon, it is well-known that the energetically favored res-

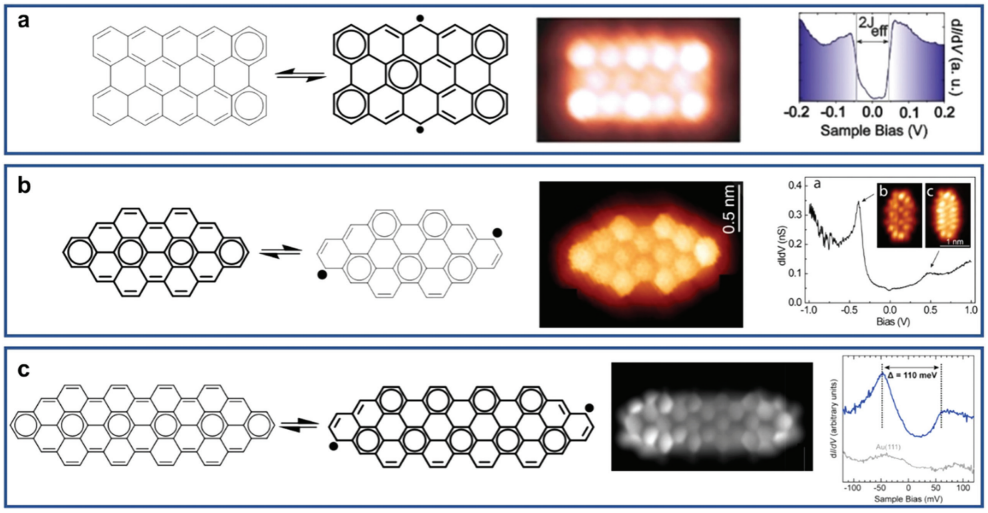

Fig. 8. Resonance structures of (a) peripentacene, (b) fused triangulene dimer, (c) fused triangulene dimer-7AGNR, and their corresponding BRSTM images and d*I*/d*V* spectra. Reproduced with permission [68,102,103]. Copyright 2020, 2021, American Chemical Society; Copyright 2020, American Physical Society.

onance structure is the structure displaying the largest number of Clar sextets, which is termed as the *Clar formula* [96]. The energy gain for aromatic stabilization per Clar sextet is about 90 kJ/mol [97,98]. On the other hand, the cleavage of a C–C π-bond (breakage of a Kekulé structure) along with the generation of two radicals needs energy about 270 kJ/mol [98,99]. Therefore, the generation of two radicals associated with the formation of an open-shell structure may be favored if three or more additional Clar sextets can be gained by this. Several examples actually confirmed that this value is the threshold to adopt the graphene-based nanostructure an open-shell configuration [52,53,100,101].

A few representative examples are shown in Fig. 8. In Fig. 8a, the open-shell resonance structure holding two radicals has three more Clar sextets than its closed-shell counterpart, thus exhibiting an open-shell ground state with the exchange energy of 40.5 meV [102]. In contrast, the fused triangulene dimer in Fig. 8b has only one more Clar sextet in its open-shell resonance structure than its closed-shell configuration, below the threshold of three additional Clar sextets, thus exhibiting a closed-shell ground state where HOMO and LUMO were resolved in d*I*/d*V* mapping [68]. However, by extending the molecular backbone, such molecule is possible to be open-shell. As displayed in Fig. 8c, the integration of a short 7AGNR section into fused triangulene dimer (fused triangulene dimer-7AGNR) makes the open-shell resonant form of fused triangulene dimer-7AGNR has three more Clar sextets than its closed-shell form, thus the ground state turned out to be open-shell with an Coulomb gap between SOMOs and SUMOs of 110 mV [103]. Therefore, a larger molecular structure generally offers more possibilities to produce a sufficient number of Clar sextets to compensate for the generation of radicals, implying a stronger tendency to be open-shell. This is in line with the basic physical picture as discussed above. In a larger system, a large π electron conjugation typically reduces the energy gap by lowering hybridization energy of valence electrons, thus the valence electrons have higher chances to be polarized and singly occupy molecular orbitals, as driven by the Coulomb repulsion.

2.3.3.2. Long acenes. However, the above proposed threshold that at least three Clar sextets should be assigned by adding two radicals in a nanographene is only indicative and there are a number of parameters influencing the prediction of the ground state. The most outstanding example is acenes. Although only one additional Clar sextet gain is involved by assigning an open-shell di-

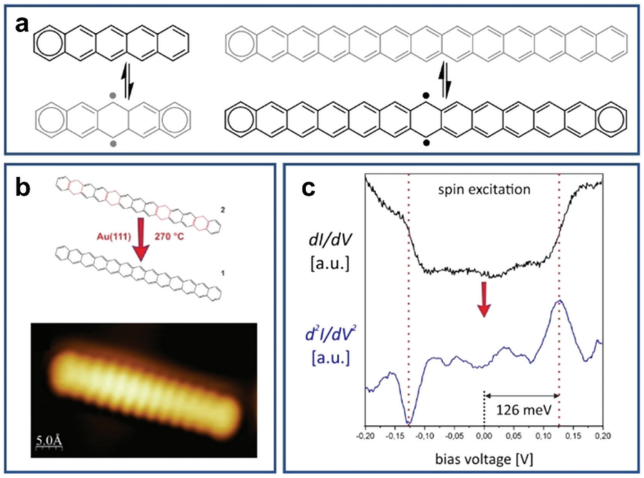

Fig. 9. (a) Resonance structure of pentacene and tridecacene, respectively. (b) On-surface synthesis procedure of tridecacene and corresponding STM image. (c) d*I*/d*V* and d^2I/dV^2 spectra obtained on tridecacene on Au(111). Reproduced with permission [112]. Copyright 2023, CC-BY-NC-ND 4.0.

radical configuration, as shown in Fig. 9a, it is still widely accepted that long acenes bear open-shell characters starting from hexacene [104–111]. In particular, in a most recent work, the spin-flip excitation with an exchange energy of 126 meV was successfully observed experimentally in tridecacene which was prepared by on-surface synthesis approach (Figs. 9b and c) [112]. In the case of an acene, the delocalization of diradical along the molecular backbone significantly decreases the energy of the additional radicals. In addition, since the Clar sextet can be assigned to every phenyl ring of an acene, the energy gain of aromatic stabilization of a Clar sextet is less than some other nanographenes, thus more Clar sextets are necessarily to be involved to lower the energy of the system, which is associated with the generation of more radicals. In fact, as predicted by theoretical studies and supported by experiments, a radical pair in a long acene may be generated per six phenyl rings [113].

2.3.4. Non-hexagonal ring integration

Above we focused on the origin of magnetism of graphene-based benzenoid nanostructures which are composed of all six-membered carbon rings. Classic Lieb's theorem and the empirical

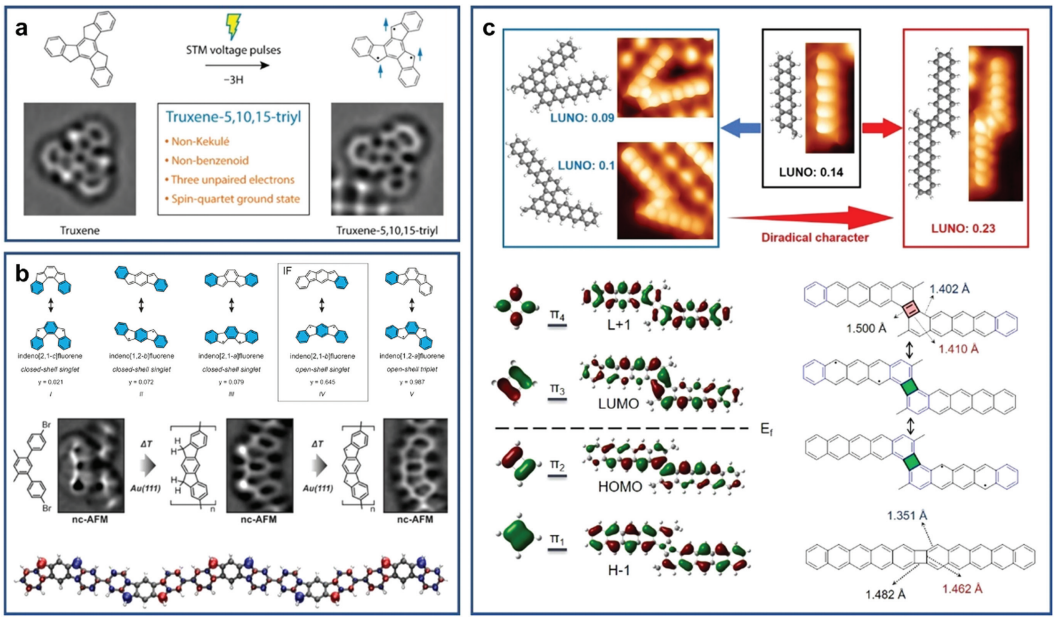

Fig. 10. (a) On-surface synthesis procedure of a high spin molecule truxene-5,10,15-triyl containing four hexagons and three pentagons, along with nc-AFM images of the precursor and product [114]. (b) On-surface synthesis of open-shell indeno[2,1-*b*]fluorene polymers, along with nc-AFM images of the precursor, intermediate, and product, as well as the spin density distribution. The open-shell characters of different isomers are also displayed on the top [115]. (c) Top: diradical character of pentacene dimers connected by a pentagon and a tetragon, respectively. LUNO: lowest unoccupied natural orbital. Down left: molecular orbital of cyclobutadiene and the pentacene dimer connected a tetragon; Down right: resonance structures and bond length analysis of pentacene dimers connected by a tetragon [61]. Reproduced with permission [61,114,115]. Copyright 2019, American Chemical Society; Copyright 2022, CC-BY-NC-ND 4.0; Copyright 2022, CC-BY 4.0.

counting rule of Clar sextet can thus be used for assessing the ground states of those structures. However, these rules are in principle invalid for the ground state evaluation of a sp^2-hybridized carbon-based nonbenzenoid systems and more parameters should be considered in these systems. The most common non-hexagonal carbon rings are five- and four-membered rings. Below we demonstrate that the character of an odd number of p_z electrons in a five-membered ring as well as the antiaromaticity of a four-membered could contribute significantly to the π-magnetism of the corresponding carbon nanostructures.

2.3.4.1. Five-membered carbon ring. Different from a six-membered ring, a five-membered carbon ring in a graphene-like structure holds five p_z electrons thus they cannot couple in pair, leaving an unpaired radical electron. This automatically brings in magnetism into the carbon-based system. Therefore, the introduction of five-membered carbon rings into graphene-based nanostructures seems to be a facile approach for the design of magnetic systems [116,117]. Truxene-5,10,15-triyl containing four hexagons and three pentagons as displayed in Fig. 10a was predicted as a polycyclic hydrocarbon holding a high spin of 3/2, which is a promising unit for the construction of extended ferromagnetic carbon nanomaterials as future spintronics. The realization of the synthesis was by tip manipulations on a precursor of truxene by removing additional hydrogens on surfaces [114,118]. The perfect agreement between experimentally and theoretically obtained SOMO/SUMO mapping supports its $S = 3/2$ ground state. The absence of Kondo resonances is probably because the Kondo temperature of this system is much lower than 4 K [118].

Indenofluorenes are a kind of polycyclic hydrocarbons containing two pentagons and three hexagons, as shown in Fig. 10b [115,119–122]. Such structure has two competing closed/open-shell resonance structures, because the two radicals from five-membered rings could either hybridize into a closed-shell structure or keep singly occupied (open-shell). This is determined by the competition between hybridization energy and Coulomb repulsion energy as already described above. According to theoretical calculations, different isomers have completely different open-shell character (Fig. 10b). Among them indeno[2,1-*b*]fluorene has been predicted to be open-shell and its on-surface synthesis was achieved by introducing two methyl groups in the precursor molecule [115]. Through Ullmann coupling upon annealing on Au(111), indeno[2,1-*b*]fluorene polymers have been fabricated, which exhibit a small bandgap of 0.4 eV and could easily fuse into porous graphene nanoribbons due to the high reactivity. However, because of the extremely weak magnetic anisotropy, no magnetic signals of indeno[2,1-*b*]fluorene were resolved in experiment.

2.3.4.2. Four-membered carbon ring. Four-membered carbon ring has an even number of p_z electrons, thus in principle they can couple in pair. Therefore, it seems the behavior of a four-membered ring for carbon magnetism should be similar as the case of a six-membered ring as discussed in detail above. However, a sp^2-hybridized four-membered carbon ring, which is called cyclobutadiene, has a strong antiaromatic character thus involving an establishing effect, as opposed to the stablishing effect of an aromatic six-membered ring [123–126]. As a result, the π electrons (associated with the double bonds) prefer localizing outside the four-membered ring. In other words, a four-membered ring in graphene-based nanomaterials favors a radialene structure other than an annulene structure. This impact originating from the antiaromaticity of cyclobutadiene would inevitably rearrange the bond alternation of the graphene-based nanostructure, which in turn possibly tunes the magnetic properties.

The most well-studied example is the staggered pentacene dimer connected by a four-membered ring. Although the pentacene monomer is a closed-shell molecule [127], both theoretical and the further experimental results supported the staggered pentacene dimer connected by a four-membered ring exhibit obvious diradical character [61,123,128]. As displayed in Fig. 10c, while the pentacene dimers connected by a five-membered ring shows a very low LUNO (lowest unoccupied natural orbital; an index de-

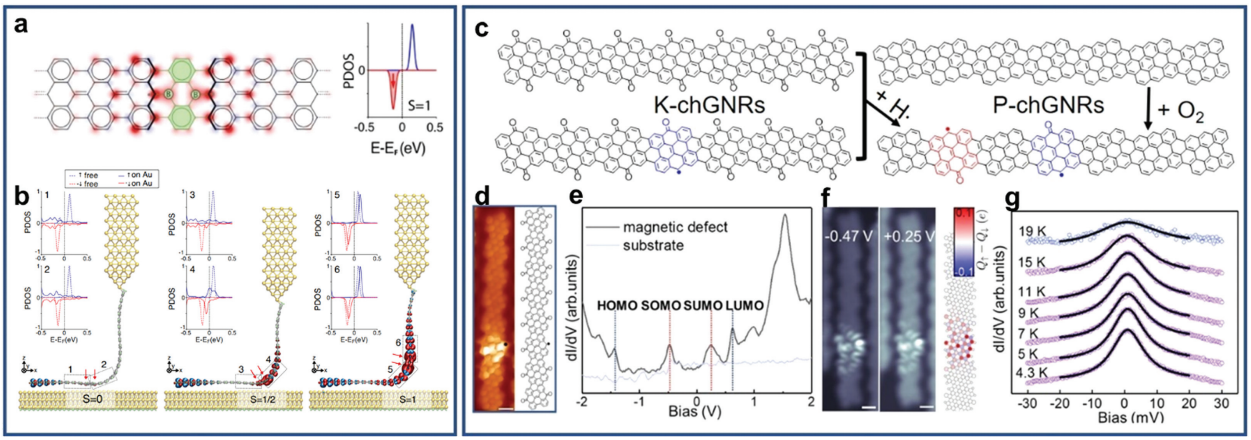

Fig. 11. (a) Spin density distribution of 2B-doped 7AGNR. (b) Simulation of tip lifting process of the 2B-doped 7AGNR from the Au(111) surface, showing unquenched net spin in each case. (c) Synthetic methods for the preparation of magnetic ketone substituted chiral graphene nanoribbon (chGNRs). (d) BRSTM image and corresponding chemical structure of ketone-chGNR with one pristine defect. (e) d*I*/d*V* spectra acquired on magnetic defect and substrate. (f) SOMO and SUMO mapping, along with the spin density calculated by DFT. (g) Temperature dependent Kondo peak broadening of ketone-chGNR with one pristine defect. All the Kondo peaks are perfectly fitted by a Frota function. Reproduced with permission [64,131]. Copyright 2020, CC-BY 4.0; Copyright 2021, CC-BY-NC-ND 4.0.

scribing open-shell character) value, which is even lower than pentacene monomer itself, the pentacene dimer connected by a four-membered ring presents a much higher LUNO value than pentacene monomer [61]. In addition, the energy gap of the pentacene dimer connected by a four-membered ring is much lower than other two dimers, further supporting its open-shell configuration [61]. Further analysis on the molecular orbital revealed that the frontier molecular orbitals of the pentacene dimer connected by a four-membered ring have very similar DOS distributions of frontier orbitals on the four-membered ring as those of cyclobutadiene, thus inheriting the antiaromatic character of cyclobutadiene. However, because the destabilizing effect of antiaromaticity, the double bonds do not localize inside the four-membered ring, leading to the bond rearrangement and the formation of two resonance structures, as shown in Fig. 10c. The similar bond length between the "double bond" of cyclobutadiene and nearest C−C bond on the phenyl ring implies the coexistence of the closed and open-shell resonance structures. In sharp contrast, the straight pentacene dimer connected by a four-membered ring does not show any open-shell character because the four-membered ring in this structure is composed of four single bonds thus no destabilizing effect of antiaromaticity is involved [128–130]. More theoretical works on staggered long acene nanoribbons connected by four-membered rings demonstrate that the four-membered ring serves as a spin switch to reverse the spin orientations of the two zigzag edges of an acene and lift the degeneracy between the two spin propagation channels, *i.e.*, spin-up and spin-down, thus being a promising platform for spin filtering and transport [123].

2.3.5. Heteroatom doping

Heteroatom doping is another efficient way to introduce π-magnetism into graphene-based nanostructures, since a heteroatom could have a different number of π electrons as carbon [90]. The introduction of heteroatoms thus possibly to make a closed-shell nanostructure to be magnetic. As an example shown in Fig. 11a, the introduction of boron atoms into non-magnetic 7AGNR makes the total π electrons in the system imbalanced, bringing in π-magnetism into the system [131]. Specifically, B atom has three σ electrons and they couple with carbon atoms covalently *via* three single bonds thus the two p_z electrons in the carbon atoms nearby are unpaired and cannot couple each other due to the separation of B atoms. Theoretical calculation predicted that 2B-7AGNR has a triplet $S=1$ ground state. Because of the strong interaction between the Au(111) surface and 2B-7AGNR, the net spin was quenched by the significant charge transfer. Nevertheless, the Kondo resonance as a magnetic fingerprint was detected by tip lifting (Fig. 11b) experiment [131] or the intercalation of silicon layers between Au(111) and 2B-7AGNR [132].

Apart from the introduction of heteroatom into precursor molecule, very recently a novel synthetic method for the fabrication of heteroatom doped magnetic carbon structures have been developed on the basis of post-oxidization or reduction reactions [64,83,133]. The oxidization reaction is by exposing the graphene-based nanostructure holding zigzag edges to oxygen gas in a UHV chamber. Because of the high reactivity of zigzag edges, the central carbon atoms can be typically oxidized into ketone groups. As a result, the introduction of a ketone group to the graphene-based nanostructure efficiently adds one p_z electron into the system, thus bringing in an unpaired π electron into the otherwise closed-shell structure. An example is shown in Fig. 11c (right part) [64], where a pristine chGNR was oxidized by two ketone groups through oxygen gas exposure, generating two π radicals. On the contrary, ketone substituted graphene-based structures can be reduced by atomic hydrogens, which equally introduces π-magnetism. In this case, the reduction of a ketone group efficiently removes one p_z electron from the system, generating one π radical. One example is again shown in Fig. 11c (left part) [64], where a ketone-chGNR with a pristine defect was obtained by partial reduction of a ketone-chGNR. The introduction of magnetism in above-mentioned ketone substituted chGNRs was confirmed by d*I*/d*V* maps of SOMO and SUMO (Figs. 11d-f), and Kondo resonance which broadens anomalously fast with temperature increasing (Fig. 11g) as well as spin-flip excitations (will be discussed below).

2.3.6. Charge transfer

Above we discussed the intrinsic π-magnetism of graphene-based nanostructures. The origins of carbon magnetism include sublattice imbalance, topological frustration, spin polarization, nonhexagonal carbon ring integration, and heteroatom doping. In fact, apart from the intrinsic magnetism, it is well-known that at the interface between an organic structure and the substrate, charge transfer could occur when the work function of the two materials cannot match [81,134]. In this case, if a spin electron (or more) transfers from the carbon structure to the surface and *vice versa*, the carbon structure possibly holds unpaired π electrons, exhibiting π-magnetism.

As pioneer works, metal-free and zinc coordinated porphyrins, which are closed-shell in their neutral form, were measured

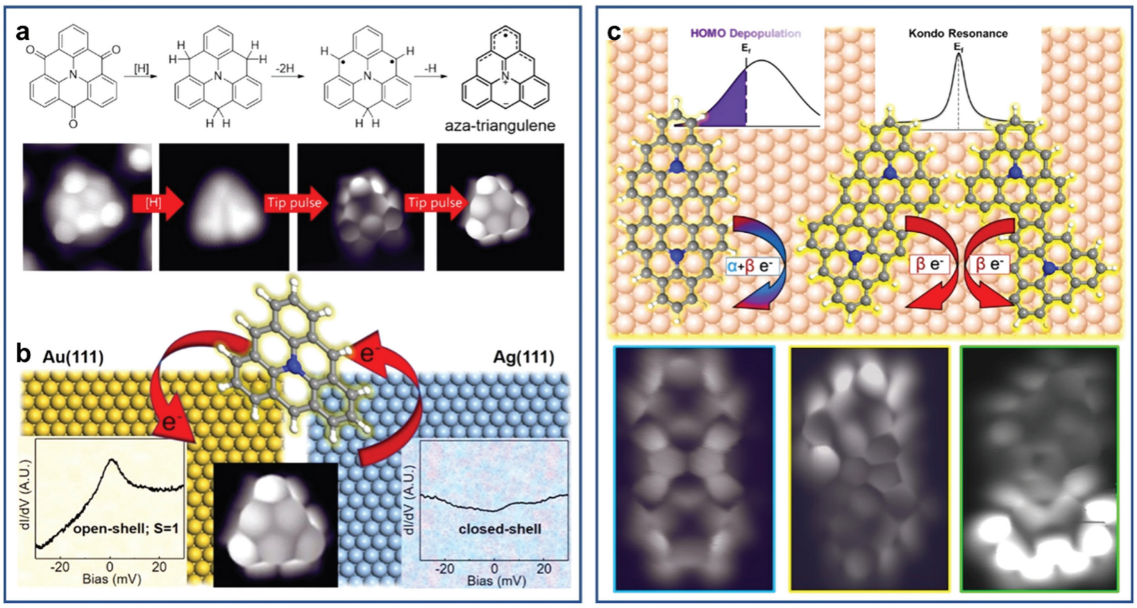

Fig. 12. (a) Synthetic approach of aza-triangulene on metal surfaces by atomic hydrogen reduction and tip manipulation, along with the corresponding BRSTM image in each step. (b) Charge transfer of aza-triangulene on Au(111) and Ag(111) respectively and the low-energy STS in both cases. (c) Schematic drawing of charge transfer behaviors of a symmetric fused aza-triangulene dimer and two asymmetric aza-triangulene dimers, along with their corresponding BRSTM images. Reproduced with permission [83]. Copyright 2022, CC-BY 4.0.

as magnetic on an Au(111) surface evidenced by the detection of Kondo resonances [135,136]. This is because the porphyrin molecules transferred an electron to the substrate, leading to the generation of an unpaired electron. Apart from the magnetization of a closed-shell structure, charge transfer at molecule-substrate interface could also efficiently tune the magnetic state of intrinsically magnetic molecules. An representative example is shown in Figs. 12a and b [83]. Aza-triangulene in its neutral form holds a ground state of $S=1/2$, by forming an two fold-symmetric (C_{2v}) zwitterionic structure as driven by Jahn-Teller distortion (Fig. 12a) [90]. It can be synthesized on surfaces by the reduction of ketone substituted aza-triangulene using atomic hydrogen in UHV as described above, followed by accurate tip manipulations, as displayed in Fig. 12a. On a high work function Au(111) surface (~5.3 eV), charge transfer happens from aza-triangulene to the substrate (Fig. 12b), leading to the formation of a ground state of $S=1$. In this case, the nitrogen atom is equal to a carbon atom after the charge contribution, thus the ground state of the positively charged aza-triangulene is same as the unsubstituted triangulene. In contrast, on a low-work function substrate Ag(111) (~4.7 eV), the charge transfer direction of aza-triangulene reversed. Ag substrate donates an electron to aza-triangulene, leading to the double occupation of all frontier orbitals below Fermi level. Therefore, the ground state of the negatively charged aza-triangulene is closed-shell.

It is worth noting that the charge transfer leading to the generation of π-magnetism is in contrast with the conventional charge transfer protocol which simply gives rise to the depopulation of frontier molecular orbitals. The π-magnetism of an otherwise closed-shell carbon nanostructure can only appear when spin-selective charge transfer occurs. In other words, the number of α and β spin electrons transferring from (to) the surface should be different, which in turn brings in non-zero net spin into the system. A recent study toward the magnetism of fused aza-triangulene dimers on Au(111) reveals the parameters influencing such spin selective charge transfer (Fig. 12c) [137]. Two kinds of aza-triangulene dimers can be obtained upon lateral fusion of aza-triangulene monomers by annealing the Au(111) sample covered by aza-triangulene monomers at a high temperature. They are all closed-shell in the neutral form. However, interestingly, the experiment on Au(111) shows that although all dimers transferred a comparable number of electrons to the Au(111) surface, only the asymmetric dimers showed magnetic fingerprints (Kondo resonance). The appearance of magnetism in asymmetric products is due to the disruption of π-conjugation patterns, which results in more localized frontier orbitals and in turn leads to a large Coulomb repulsion. A large Coulomb repulsion then promotes the spin-selective charge transfer from the asymmetric dimers to Au(111). This is in contrast with the HOMO depopulation in the symmetric dimer where the DOS distribution is delocalized, involving a smaller Coulomb repulsion. As a result, in the case of the symmetric dimer, a same number of α and β spin electrons transferred to the Au(111) substrate, thus the net spin of the positively charged dimer is still zero.

2.3.7. Topological end states

For an extended system, such as graphene nanoribbon and polymers, apart from the π-magnetism from the unitcell (nanographene) itself, the π-magnetism can appear as end states in topological nontrivial structures [141,142]. In the classical tight binding theory (SSH model) [143], the topology of a π-conjugated material is determined by the competition of electron hopping terms, *i.e.*, t_{intra} in the unitcell and t_{inter} between the unitcells, as the simplest case. As an example, in the physical picture of one-dimensional structure, if t_{intra} is larger than t_{inter}, the structure is topologically trivial. On the contrary, if t_{inter} is larger than t_{intra}, the structure will be topologically nontrivial exhibiting singly occupied end states at the terminal of the one-dimensional material. In addition, if t_{inter} is equal to t_{intra}, the material will be metallic with a zero bandgap. The bandgap is calculated as $E=2||t_{inter}|-|t_{intra}||$ [141]. Fig. 13a displays the well-known example of trans-polyacetylene with a finite length. Two resonance structures can be drawn for the trans-polyacetylene and one of them contains two radicals as the topological end states [138].

Recently by on-surface synthesis, several topologically nontrivial π-conjugated carbon materials have been fabricated and

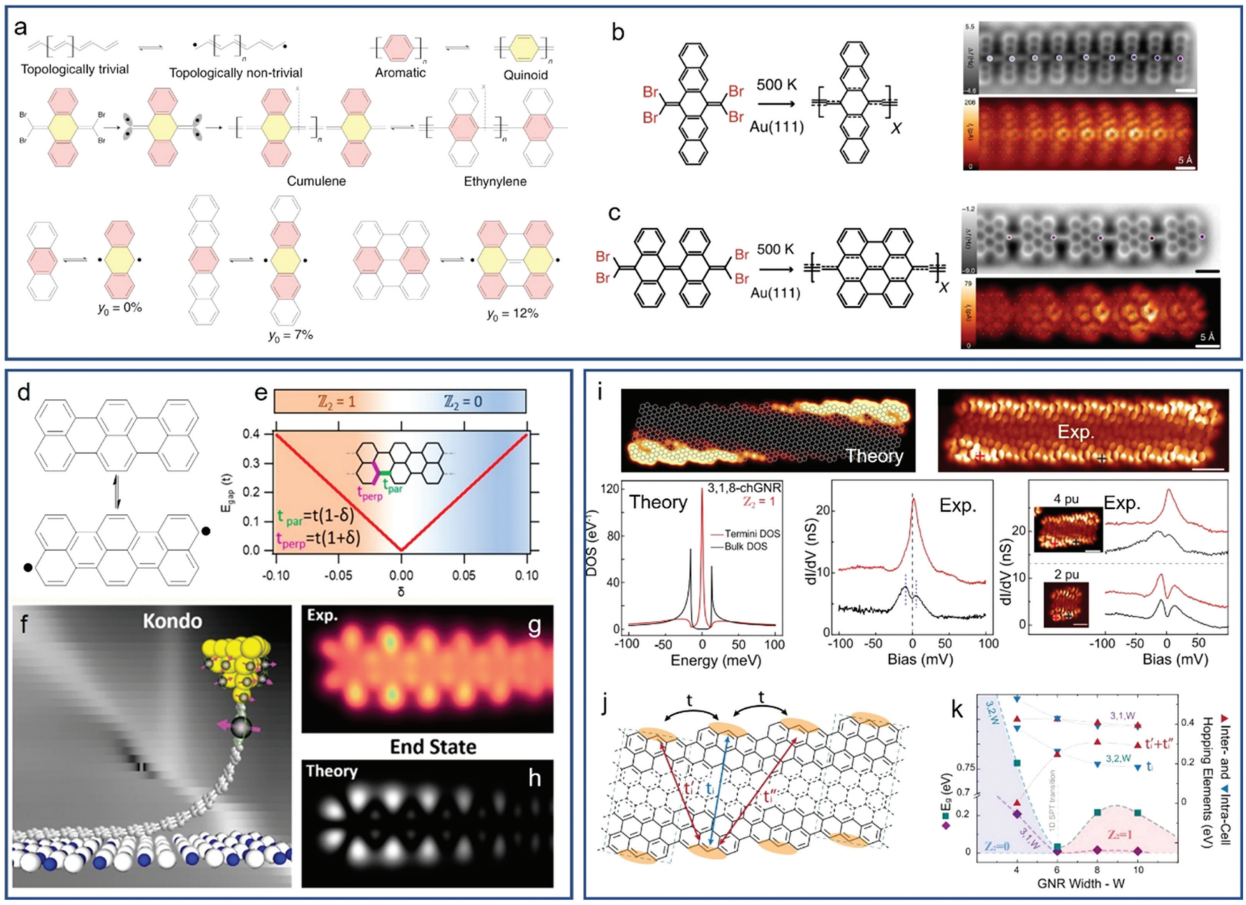

Fig. 13. (a) Top: Resonance structures of *trans*-polyacetylene and poly(*para*-phenylene). Middle: On-surface synthesis strategy for the formation of acene-based poly(*para*-phenylene). Bottom: resonant forms for anthracene, pentacene and bisanthene. The diradical character y_0 is shown below for each structure. (b, c) On-surface synthesis of topologically non-trivial quinoid poly(*para*-phenylene), using pentacene and bisanthene as the central unit, respectively. Nc-AFM and BRSTM images are shown for each case. (d) An example showing the resonance structure of 5AGNR. (e) Topological class and bandgap of 5AGNR, along with the changing of hopping term of t_{par} and t_{perp} as marked in the chemical structure. (f) Kondo resonance by lifting a 5ANGR from the NaCl/Au(111) surface. (g, h) Experimentally mapped and theoretical simulated end states of 5AGNR. (i) Theoretical and experimental end states of a wide chGNR, namely 3,1,8-chGNR. STS are shown below STM images. (j) Tight binding modelling of the electron hopping of 3,1,8-chGNR. (k) Topological class and bandgap of chGNRs as dependent on their width. Reproduced with permission [100,138–140]. Copyright 2020, Springer Nature; Copyright 2020, American Chemical Society; Copyright 2021, CC-BY 4.0.

characterized in atomic precision [100,139–142]. An outstanding example is the synthesis of quinoid poly(*para*-phenylene)s using pentacene and bisanthene as the central units (Fig. 13a) [139]. In fact, poly(*para*-phenylene)s are similar as the case of *trans*-polyacetylene, where two resonance structures can be drawn as a closed-shell aromatic form and an open-shell quinoid form (ending with acene or periacene). This works showed how the rational design of the backbone of the precursor can tune the topological class of the obtained polymers. It demonstrated that both pentacene and bisanthene based finite *para*-phenylenes were topologically nontrivial while anthracene based *para*-phenylene was topologically trivial. This is because pentacene and bisanthene have higher open-shell character thus promoting the inter-electron coupling and forming a double bond in between. As a result, a quinoid linked topologically nontrivial structure is favored which shows two end states. The appearance of end states was confirmed by the detection of zero-energy states, which actually can be seen in the BRSTM obtained at a low bias voltage (Figs. 13b and c). In contrast, anthracene is a closed-shell molecule thus the intra-electron coupling is much stronger than the inter-electron coupling thus there is only a single bond connecting the two neighboring units. Therefore, the anthracene-based poly(*para*-phenylene) is closed-shell and topologically nontrivial.

Long 5AGNRs are also topologically nontrival [140]. The corresponding two resonance structures of 5AGNR are displayed in Fig. 13d. The calculation revealed that the open-shell form prevails when t_{par} in Fig. 13e is larger than t_{perp}, which is associated with the assignment of a double bond between two neighboring unitcell as shown in Fig. 13d. The experiment confirmed that the ground state of a 5GNR with unitcell more than fourteen was open-shell and topologically nontrivial, as supported by the detection of Kondo resonances at the termini in a tip-lift experiment (Fig. 13f) and also the perfect match of orbitals' DOS between experiment and theory (Figs. 13g and h). It is worth noting that the 5AGNRs including unitcell of fourteen or less are closed-shell because the two end states will hybridize into a doubly occupied orbital when their spatial distance is sufficiently short. Similar length dependent topological phase transition was found in pentance-based polyparaphenylene, in which a Jahn-Teller effect driven by vibronic coupling is responsible for the phase transition [144].

For more complex topological systems, more hopping terms should be taken into consideration. For example, a wide chGNR, namely 3,1,8-chGNR was confirmed to be topological nontrivial experimentally as evidenced by the detection of zero-energy end states at the termini (Fig. 13i) [100]. The disappearance of end

states on ultrashort 3,1,8-chGNR composing of two units is due to their hybridization, similar as the case of short 5AGNR above. Because of the complexation of its structure, the simulation of 3,1,8-chGNR by tight binding mode necessarily include four hopping terms to precisely describe the system, as shown in Fig. 13j. Using this model, the topological class as well as the bandgap of chGNRs with different width can be nicely predicted, as displayed in Fig. 13k.

Above we discussed how π-magnetism of graphene-based nanostructures generates. For a spin system containing more than one spin electron, the spin exchange interaction is an important concept to be studied, which is in turn of great significance for the design of quantum computing, magnetic storage, and spintronics. Here we review the representative studies on spin interactions in magnetic graphene-based nanostructures, including the spin systems holding two and multiple spins.

2.4. Spin interaction

Above we discussed how π-magnetism of graphene-based nanostructures generates. For a spin system containing more than one spin electron, the spin exchange interaction is an important concept to be studied, which is in turn of great significance for the design of quantum computing, magnetic storage, and spintronics. Here we review the representative studies on spin interactions in magnetic graphene-based nanostructures, including the spin systems holding two and multiple spins.

2.4.1. Two-spin system

For a two-spin system, the two most important parameters are the strength of exchange coupling which is determined (also can be tuned) by the wavefunction overlap of the radical states, as seen in Eq. 1 above and the sign of the exchange coupling, *i.e.*, ferromagnetic ($S=1$; $J<0$) or antiferromagnetic ($S=0$; $J>0$) coupled.

2.4.1.1. Strength of exchange coupling. As mentioned above, the strength of exchange coupling *J* can be tailored by tuning the overlap between the wavefunctions of radical states [62,147]. Several parameters could influence the wavefunction overlap. A representative example is displayed in Figs. 14a–d [64]. P- and K-chGNRs refer to magnetic pristine chGNR with two ketone defects and ketone substituted chGNR with two pristine defects, respectively. S and O indicate that the pairwise radicals locate at the same or opposite side of the nanoribbon. The Arabic number is the number of unit cell of chGNR separating the two radicals. In addition, A' mark is used to distinguish the different configurations from the chirality. In this example, it is clear that, the larger the distance between the two radicals, the smaller the *J* (*e.g.*, PO2 *vs.* PO1), because the wavefunction overlap is smaller. Interestingly, the *J* shows a significant dependence on the chirality. For example, although the spatial separation of the radical pair of PO1 is larger than PO1', PO1 has a larger *J*. This is because the spin density of the radical states of P-O1 extends mostly toward the central unit between the radical pairs, whereas they dominantly extend away from each other in P-O1'. It is important to note that the *J* is also influenced by the band structure of a chGNR itself. Pristine chGNR has a much smaller bandgap than that of ketone-chGNR, thus involving greater hybridization between frontier molecular orbitals and the radical states, resulting in a larger wavefunction extension of radical states along the ribbon. This explains why PO2' and PS2 still have nonzero *J* but KO2' and KS2 become paramagnetic.

Another outstanding example on tuning the strength of exchange coupling of π-radical pairs is shown in Figs. 14e–g [146]. The two isomeric magnetic nanographenes with each holding a radical pair exhibit a dramatically large difference on *J*, *i.e.*, 20 meV for D1 and 160 meV for D2. This is attributed to their distinct symmetry of frontier molecular orbitals. The HOMO of D2 is from the bonding coupling of the two monomers' states, which promotes the wavefunction overlap whereas the HOMO of D1 is from the antibonding configuration thus reducing the wavefunction overlap.

To date, the largest exchange coupling strength of near 200 meV for open-shell nanographenes was reported, which occurs in proximity to the transition between closed-shell and open-shell states [95]. A strong hybridization energy promotes the wavefunction overlap but it is not sufficient to overcome Coulomb repulsion to make the system into a closed-shell ground states, resulting in a large exchange coupling strength. The achievement of a large *J* allows device operation at practical temperatures.

We note that besides the spin coupling in covalent carbon-based nanostructure, spin electrons on self-assembled carbon structures might also interact one another *via* intermolecular interactions. Since the construction of well-ordered supramolecular carbon nanostructures with a large size is much easier than that of covalent structures [148–153], the achievement of the construction of spin interacting self-assembled systems shows a great potential for the application of future quantum materials. An example is displayed in Figs. 14h–n, where two spin electrons interact each other *via* intermolecular hydrogen bonds [145]. All-trans retinoic acid (ReA) exhibits magnetic character with one hydrogen off, as evidenced by the detection of Kondo resonances (A in Fig. 14l). The radical delocalizes over the molecular backbone. In a self-assembled dimer structure with a specific configuration (Fig. 14k), an antiferromagnetic exchange coupling was resolved (Fig. 14l), which further splited in magnetic fields. By fitting the Zeeman splitting, a Landé *g* factor of 1.7 was obtained.

2.4.1.2. Sign of exchange coupling. For a benzenoid graphene-based magnetic structure holding a radical pair, the spin order can be typically deduced from Lieb's theorem. If the two radicals occupy the same sublattice, they hold a same spin sign, thus the ground state is ferromagnetic and the total spin is $S=1$. Similarly, the ground state is antiferromagnetic and the total spin is $S=0$ if the two radicals occupy opposite sublattices. For example, again for the case of chGNRs shown in Figs. 14a–d [64], Lieb's theorem can be used to assume the spin order of radical pairs to a first approximation because a ketone group is also sp^2-hybridized which is thus considered as an additional p_z electron on its corresponding sublattice. Therefore, according to Lieb's theorem, the carbon atoms at a same edge of the chGNRs belong to the same sublattice, whereas the carbon atoms at the opposite edge belong to the opposite sublattice. A radical pair with the two radicals locating at the same/opposite side is thereof expected to be ferromagnetically/antiferromagnetically aligned. All experimentally characterized radical pairs fit this prediction, except the case of K-S1 (Figs. 14a–d). Despite the two radical sites belonging to the same sublattice in K-S1, an antiferromagnetic ground state is undoubtably derived from the experiments and also DFT calculations. The in-depth analysis revealed the different on-site energy of the oxygen atom as a carbon atom plays a significant role for the reverse of spin order in K-S1. In this particular case, the oxygen cannot be treated as a normal sp^2 carbon electron thus the conventional assumption from Lieb's theorem and mean-filed Hubbard (MFH) calculation turns out to be incorrect. Therefore, for a heteroatom doped magnetic carbon-based system, an optimized MFH tight bonding model by considering the on-site energy of heteroatoms should be used for the prediction of spin order and ground state.

Apart from the heteroatom doping, the pentagon integration could also tune the spin order of a radial pair in graphene-based magnetic structures. An example is displayed in Fig. 15 [60]. A dimer consists of two magnetic monomers with each holding one

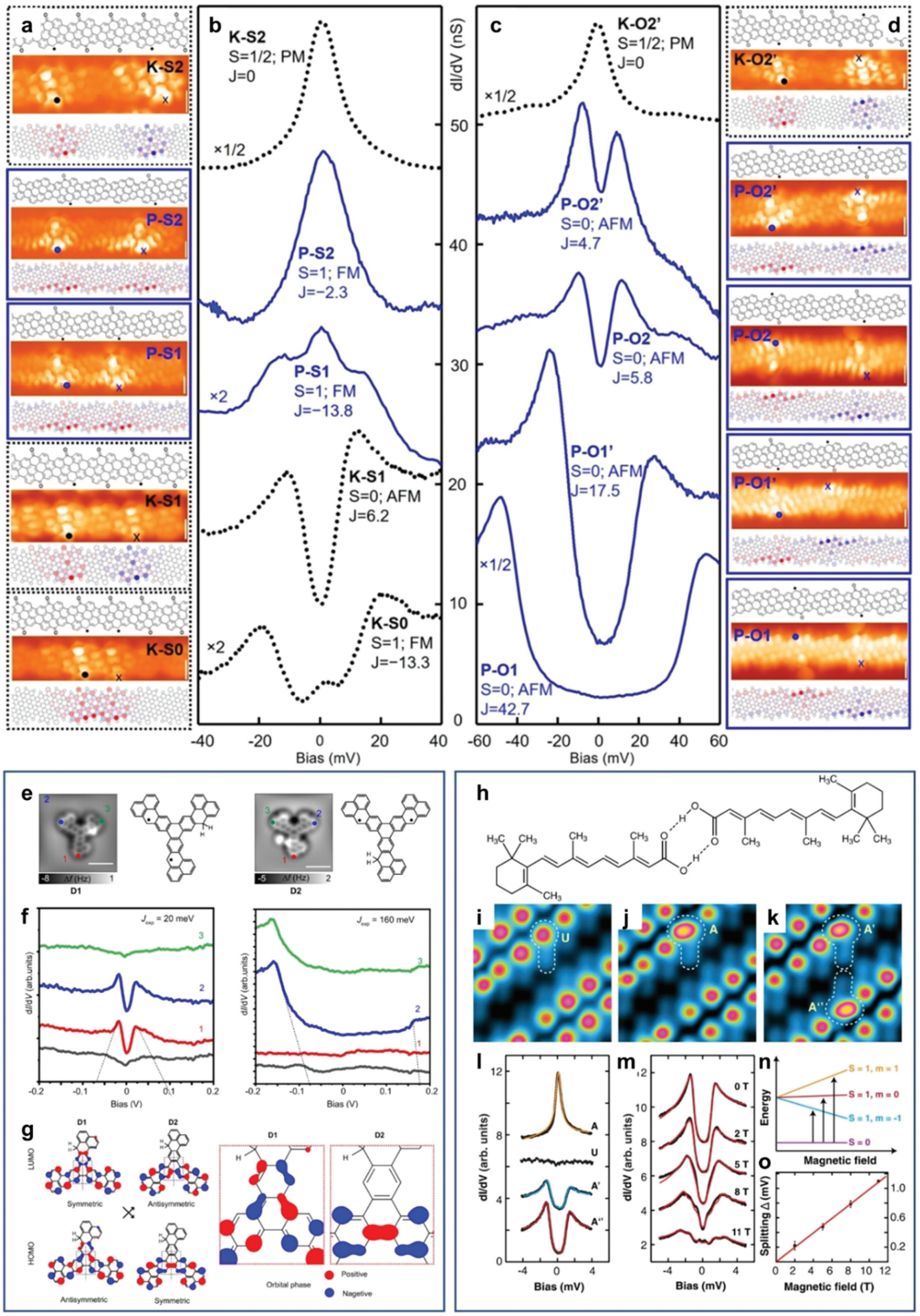

Fig. 14. (a, d) BRSTM images of experimentally obtained magnetic ketone substituted chGNRs holding radical pairs at the same side (a) or opposite sides (d) together with the chemical structure and DFT calculated spin-polarized LDOS for each case. P- and K-chGNRs corresponds to pristine chGNR with ketone defective units and ketone-chGNR with pristine defective units. (b, c) d*I*/d*V* spectra measured at the marked positions in corresponding STM images. The blue solid and black dotted curves indicate radical pairs on P- and K-chGNRs, respectively. (e) Nc-AFM images of the two trimeric magnetic nanographenes D1 and D2 containing an sp^3 carbon saturated with hydrogens for each case. (f) d*I*/d*V* spectra obtained on the two nanographenes. (g) Spin polarized DOS distribution of D1 and D2 using mean-field Hubbard (MFH) theory. (h) Molecular structure of the self-assembled all-trans retinoic acid (ReA), stabilized by hydrogen bonding. (i-k) STM images of the three supramolecular structures of ReA, with different self-assembled configurations. (l) d*I*/d*V* spectra obtained on the monomers of the three self-assembled ReA structures, respectively. (m) Zeeman splitting of the spectrum on A'' in the magnetic field. (n) Illustration of spin excitations between singlet and triplet states in magnetic fields. (o) Extracted Zeeman splitting as a function of magnetic field. Reproduced with permission [64,145,146]. Copyright 2021, CC-BY-NC-ND 4.0; Copyright 2023, CC-BY 4.0; Copyright 2022, American Physical Society.

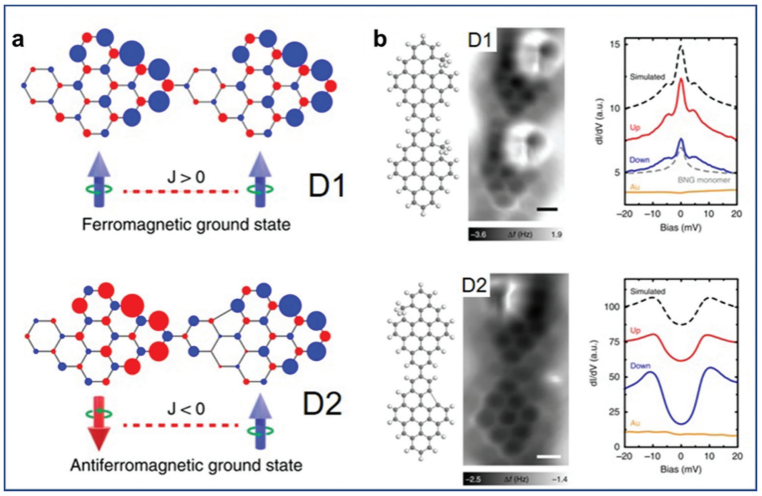

Fig. 15. (a) Spin density distribution of nanographene dimers D1 and D2. D1 consists of two equivalent benzenoid monomers and D2 consists of one such monomer and another monomer integrated with a pentagon. Spin order is marked for each case. (b) Chemical structures, nc-AFM images and d*I*/d*V* spectra obtain from experiments and simulations of D1 and D2. Reproduced with permission [60]. Copyright 2020, CC-BY 4.0.

radical. For the case of benzenoid D1, the spin order follows Lieb's theorem showing a ferromagnetic spin alignment, as evidenced by the detection of an underscreened Kondo resonance together with two spin exchange steps in STS. However, a subtle change in its structure essentially flips the spin order. D2 is formed by connecting a C−C bond in one monomer thus introducing a pentagon into the structure. As already introduced above, a pentagon carbon ring shows spin frustration because not all the electrons can be paired. As a result, it does not follow Lieb's theorem. In the case of D2, the introduction of a pentagon even reverses the ground state of D1 to be antiferromagnetic, where only two spin exchange steps were resolved in STS.

2.4.2. Multi-spin system

For a π-magnetic system containing multiple spins, the excite states will be more complicated [70,146,155–157]. Although the STM technique based on the single electron tunneling could only measure the excitation with $\Delta S = 1$, the excited states still have a number of different spin alignments. The excitation processes then exhibit as multiple spin-flip excitation steps in a d*I*/d*V* spectrum. In addition, theoretical methods based on mean-field approximations, in which the wave functions are the $\hat{S}_z$ projection instead of the eigenstates of the total spin operator $\hat{S}^2$, are insufficient to describe the many-body physical system. Higher-class calculation approach as represented by Heisenberg spin model have been used for the modelling of a magnetic carbon system involving more than two interacting spin electrons [157].

Three examples of such multi-spin systems are presented in Fig. 16. In Figs. 16a–d, an asymmetric triradical graphene trimer was synthesized on the Au(111) surface [146]. Spin exchange steps at ± 160 mV (Figs. 16b and c) were resolved at positions 1 and 2 (Fig. 16a) while a Kondo resonance was shown at position 3. According to the Heisenberg model shown in Fig. 16d, the ground state of the system is $S = 1/2$ and the spin exchange strength between 1 and 2 is much larger than that between 1 and 3 or 2 and 3. This implies that the antiferromagnetic unpaired electrons 1 and 2 are strongly correlated which is evidenced by the exchange steps in d*I*/d*V* spectrum, while 3 is almost uncoupled from other two thus exhibiting Kondo resonance. A similar phenomenon showing such asymmetric spin excitations was also observed in a triradical nitrogen-doped nanographene trimer very recently [157].

Figs. 16e–h show the characterization of a nanostar consisting of six triangulene molecules [154]. The ground state was calculated as $S = 0$ where all triangulene monomers interact with their neighbors antiferromagnetically (Fig. 16e). A Heisenberg model was used to describe the system by considering a triangulene monomer as an $S = 1$ operator. The results showed there are mainly two excitation channels from $S = 0$ to $S = 1$ (Fig. 16g), which was resolved nicely in d*I*/d*V* measurement experimentally (Figs. 16f and h). Figs. 16i–j present an example of ketone substituted magnetic chGNR holding three periodic radicals aligned ferromagnetically [64]. The d*I*/d*V* spectrum measured at the central site is obviously broader than spectra obtained at the other two sites. This implies that apart from an underscreened Kondo resonance of an $S = 3/2$ system, the central site involves more excitation channels/possibilities with higher exchange energies from $S = 3/2$ to $S = 1/2$. Theoretical calculation confirmed the supposition. It demonstrated that only the high-energy excitation contributed at the central radical site, whereas the other two sites exhibited predominantly the low-energy site, thus perfectly matching the experimental observation.

2.4.3. Spin chain

The synthesis and characterization of spin chains have been also achieved by the on-surface synthesis approach [70,156]. As shown in Fig. 17, spin chains composed of triangulene monomers was obtained *via* Ullmann coupling and cyclodehydrogenation reactions [70]. Interestingly, $S = 1/2$ edge states were detected at the chain termini when a chain is sufficiently long, as evidenced by the appearance of an underscreened Kondo resonance (Figs. 17b and c). This is attributed to the valence bond between the triangulene units, which forms an $S = 0$ state to avoid Pauli repulsion (Fig. 17d). As a result, the two spin electrons at the two terminals cannot be paired thus each leaving an $S = 1/2$ spin. A similar fractional edge excitation was observed in magnetic metal-free porphyrin chains, which only appears in the chain consisting of odd numbered porphyrin units (Figs. 17e and f) [156]. The achievement of fractional edge excitations in nanographene spin chains opens a potential path for the realization of measurement-based quantum computation.

2.4.4. Metallic graphene nanoribbon

In addition to the construction of spin chains, magnetic nanographenes can be also used for the design of metallic graphene nanoribbons, as the unit cells of a metallic GNR. According to SSH model, the periodic integration of local spins into a GNR

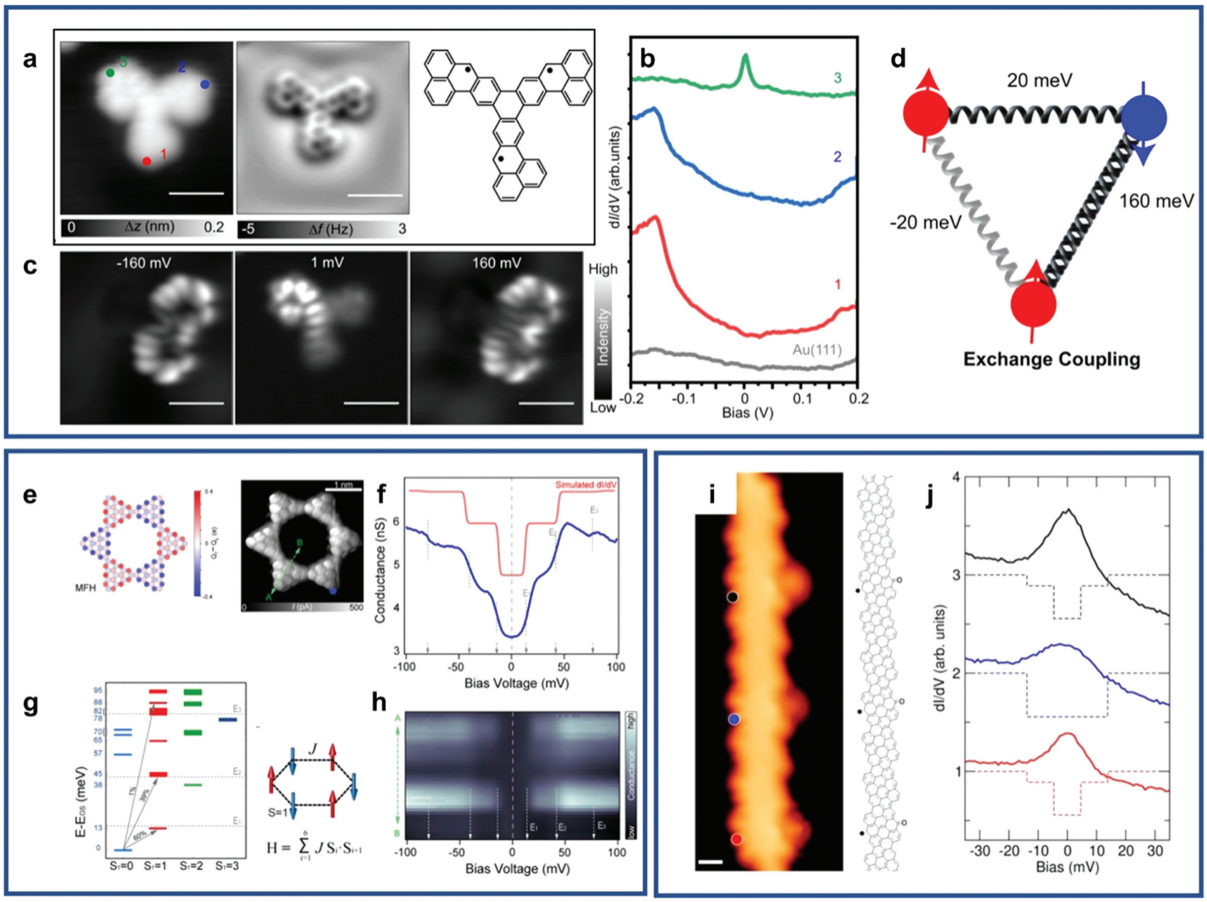

Fig. 16. (a) STM, nc-AFM images and the chemical structure of a magnetic nanographene trimer holding three radicals. (b) d*I*/d*V* spectra obtained on different sites on the trimer, as marked in the STM image in (a). (c) d*I*/d*V* maps obtained at the resonant energies in the d*I*/d*V* spectra. (d) Spin interaction model of the trimer. (e) BRSTM image of a star-sharp nanographene composing of six triangulene monomers, along with the spin distribution. (f) Experimental d*I*/d*V* spectrum obtained on the nanostar, along with the simulation. (g) Excitations of the collective spin states ($S=0$ to $S=1$) obtained from a Heisenberg mode. (h) d*I*/d*V* spectral line measured across a triangulene monomer unit as indicated in the STM image in (e). (i) STM image and corresponding chemical structure of a magnetic ketone substituted chGNR holding three periodic radicals. (j) d*I*/d*V* spectra obtained at different sites on the chGNR, along with the theoretically calculated spin exchange steps. Reproduced with permission [64,146,154]. Copyright 2023, CC-BY 4.0; Copyright 2021, John Wiley and Sons; Copyright 2022, CC-BY-NC-ND 4.0.

leads to equivalent hopping term t between neighboring unit cells, thus resulting a zero bandgap [158]. However, it should be noted that the hopping term should be large enough to avoid spin polarization, keeping a robust/wide metallic band.

In Fig. 18, it displays two metallic GNRs synthesized to date on the Au(111) surface [158,159]. Firstly, sGNRs and 5-sGNRs were obtained *via* cyclodehydrogenation and Ullmann coupling of precursor **1** [158]. Upon this, one π radical was generated in every unit cell. Since the nanographene monomer is asymmetric, the arrangement of these magnetic units lacks of periodicity. Nevertheless, a few periodically aligned magnetic units can be observed on the sample, enabling the detailed characterization by STS. In this case, sGNRs showed a ferromagnetic ground state due to the spin polarization, whereas 5-sGNRs turned out to hold a robust metallic band, as confirmed by the prefect matching between experiments and DFT calculations (Figs. 18d–g). This is because the hopping term between magnetic states on sGNRs is much smaller than that on 5-sGNRs, leading to a narrow width of metallic band thus suffering from the spin polarization. In contrast, the introduction of five-membered rings into the latter disrupts the sublattice-relevant distribution of zero modes, in turn increasing the corresponding wavefunction overlap associated with a large hopping term.

Nevertheless, the sGNR shown above lacks a long order periodicity. To overcome this shortage, another precursor molecule was used for the synthesis of olympicene metallic GNR 5-oGNR (Figs. 18h and i) [159]. The precursor **2** is structurally symmetric which thereof imposes periodic magnetic units into the GNRs, with each unit holding one π radical. A high-yield olympicene metallic GNR sample was thus obtained (Figs. 18j and k) on an Au(111) surface. The achievement of the synthesis of metallic GNRs opens a door for device interconnects and create new opportunities for exploring exotic physical phenomena like one-dimensional Luttinger liquids, plasmonics, superconductivity and so on [160,161].

2.5. Decoupling spins from metal substrates

As mentioned above, the on-surface synthesis of graphene-based nanostructures is typically based on metal surface–assisted chemical reactions, where the strong screening and Fermi level pinning effects of the metallic substrates can not only alter the designer bulk electronic band structures but also let the spin states become either quenched or highly untunable with external gates [62,162,163]. Therefore, decoupling the spins from the high density of low-energy electronic states inherent to a metal substrate is necessary for detailed property characterizations or prototypical device fabrications.

The weakened screening effect from the metal substrate due to decoupling significantly increases the on-site Coulomb repulsion *U*

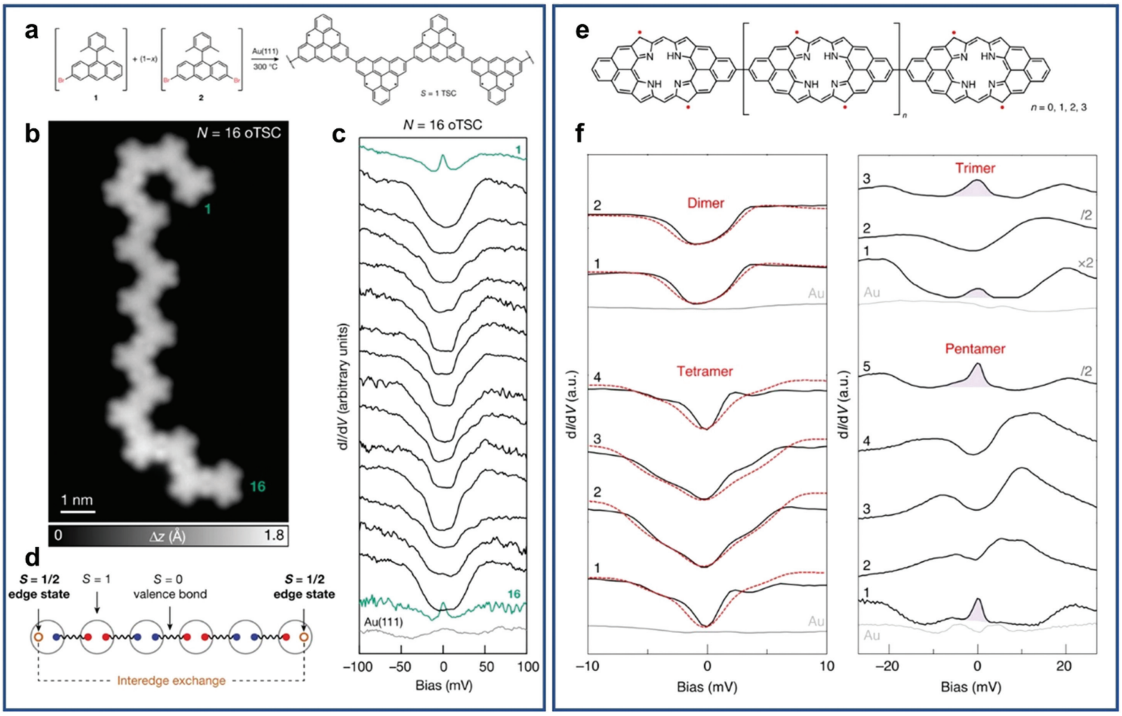

Fig. 17. (a) Synthetic approach for the formation of the spin chains composed of triangulene monomers. (b) STM image of a spin chain consisting of 16 triangulene monomer units. (c) dI/dV spectra obtained at different units on the spin chain. The starting and ending units are marked as no. 1 and 16, respectively. (d) Representation of triangulene as two $S=1/2$ spins (blue and red circles) projected over the $S=1$ triplet state. Wavy lines indicate valence bonds, which couple two spin electrons from neighboring triangulene monomers into an $S=0$ singlet state. (e) Chemical model of the spin chain composed of magnetic metal-free porphyrins. (f) dI/dV spectra measured on the porphyrin chain with different length. Reproduced with permission [70,156]. Copyright 2021, 2023, Springer Nature.

of the system (Fig. 19). The Coulomb repulsion U can effectively lift the degeneracy of the zero-energy states *via* spin polarization and open an energy gap that separates SOMO and SUMO. U is given by Eq. 2, where ε indicates the dielectric constant and $\langle\rangle$ indicates the average Coulomb energy.

$$U = \frac{1}{4\pi\varepsilon}\left\langle\frac{e^2}{r_{12}}\right\rangle \tag{2}$$

Thus, U can be increased by introducing a dielectric layer with a small ε. Currently, several methods for decoupling spins from metal substrates have been reported, such as tip lifting, transferring nanostructures onto insulating layers by tip-assisted manipulation, growth on semiconducting substrates and direct growth of second-layer GNRs.

2.5.1. Tip lifting

As a direct and effective *in situ* STM technology to measure the conductance properties of nanostructures on metal surfaces [140,162,164], STM tip lifting is naturally used for decoupling spins from metal substrates to measure the intrinsic magnetism of graphene-based nanostructures. A few representative examples are shown in Fig. 20. In the example shown in Figs. 20a–c [131], while the eventual magnetic ground state was quenched by the significant charge transfer between the 2B-7AGNR and Au(111) surface, the Kondo resonance as a magnetic fingerprint was detected by picking individual 2B-7AGNRs from one end and lifting them off to lie freestanding between the tip and sample.

Another outstanding example of measuring the intrinsic magnetism of graphene-based nanostructures by tip lifting is shown in Figs. 20d–f [165]. Substitution of two trigonal planar C-atoms in each subunit with nitrogen atom pairs along the backbone of chevron-type GNRs, and a pair of surplus π-electrons will be introduced into each subunit. Because of charge transfer between the GNRs and substrate, each subunit along the backbone of N_2-cGNRs donates a single electron to the Au substrate, leaving a chain of highly localized radical cations behind, forming one-dimensional (1D) Kondo spin chains (Figs. 20d and e). STM tip lift-off transport measurements revealed robust exchange coupling between neighboring spin centers after the effective screening of the unpaired radical cation was locally reduced (Fig. 20f).

2.5.2. Transfer to insulating layers

Transfer the nanostructures to the insulating surface by later tip-assisted manipulation is another effective *in situ* STM-based method to decouple the spins from the metal surface, which has been widely adopted to produce quasifreestanding features [41,140,166,167]. In fact, several monolayered NaCl islands are commonly used as decoupling layers. The manipulation steps are shown in Fig. 21a as an example of a ribbon on Au(111). First, pick up the ribbon at one terminus with the STM tip and retract the STM tip; move the tip (together with ribbon) laterally toward the NaCl island; release the ribbon by a bias pulse, leaving the ribbon partially adsorbed on NaCl and partially on the metal surface; finally, lateral position the ribbon fully onto NaCl by the STM tip. By following this method, (7, n) GNRs were first fabricated on Au(111), and then a submonolayer of NaCl was deposited (Figs. 21b–e [166]). Subsequently, STM manipulation was applied to transfer a (7, 20) GNR onto a NaCl island (Fig. 21c). Electronic decoupling of the edge states at the zigzag termini by transferring (7, n) GNRs onto the NaCl island establishes a large energy splitting between occupied and unoccupied edge states (Figs. 21d and e), which is missing completely in (7, n) GNRs on Au(111). In Figs. 21f–i it shows a similar example of efficient electronic decoupling from a metal substrate that transferred a short 7AGNR exhibiting a single edge extension onto a NaCl monolayer island [168]. Hubbard-split singly occupied and unoccupied states of the

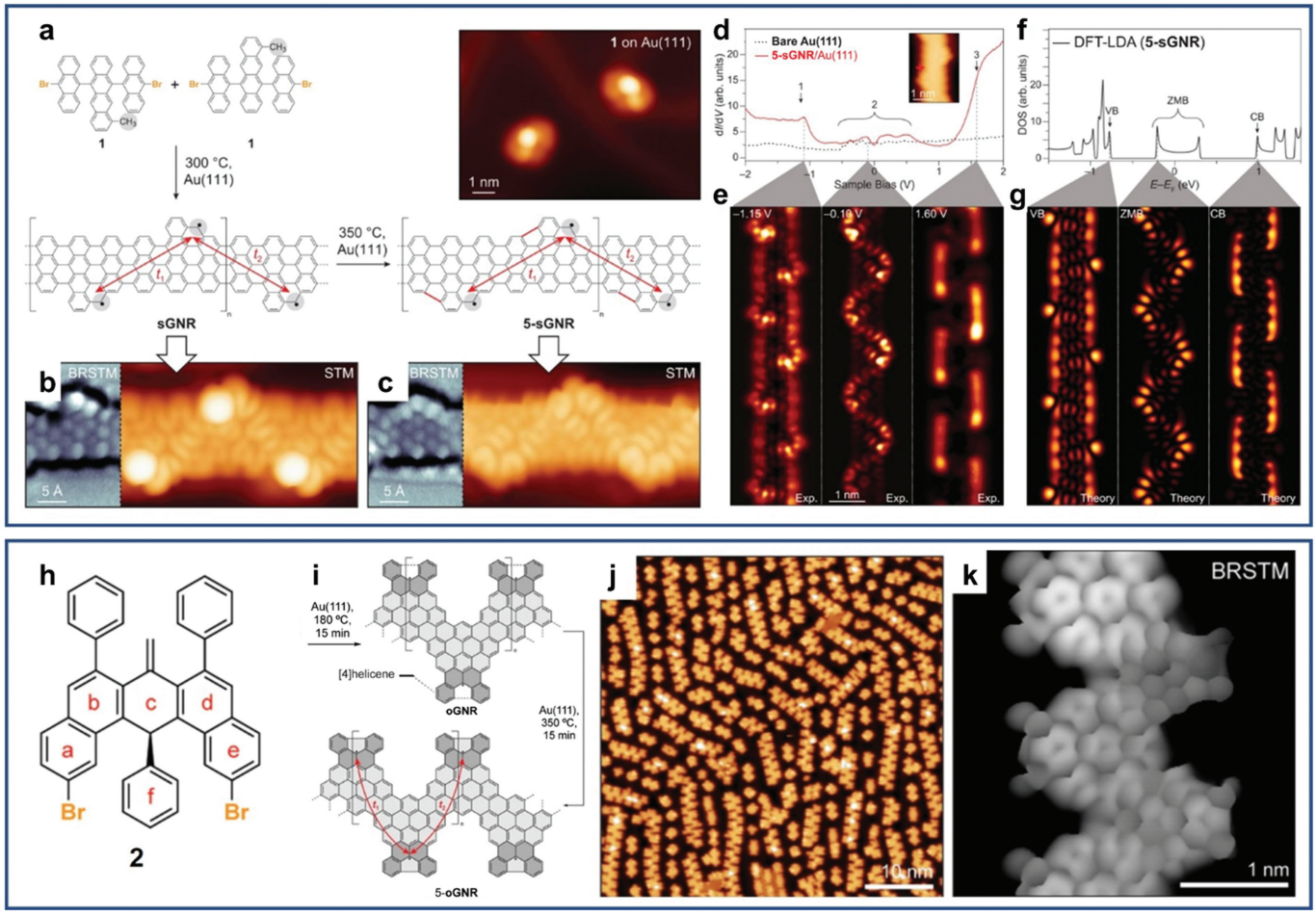

Fig. 18. (a) Synthetic approach for the formation of metallic GNR (5-sGNR) on Au(111). (b, c) BRSTM and conventional STM images of the intermediate sGNR and the final product 5-sGNR. (d, e) STS obtained on 5-sGNR and d*I*/d*V* maps at resolved resonances. (f, g) Theoretical calculated DOS and simulated d*I*/d*V* maps of 5-sGNR. (h) Chemical structure of the precursor for the synthesis of olympicene metallic GNR (5-oGNR). (i) Reaction scheme for the synthesis of 5-oGNR on Au(111). (j, k) Large-scale and BRSTM images of the sample of 5-oGNRs. Reproduced with permission [158,159]. Copyright 2020, Association for the Advancement of Science; Copyright 2023, CC-BY 4.0.

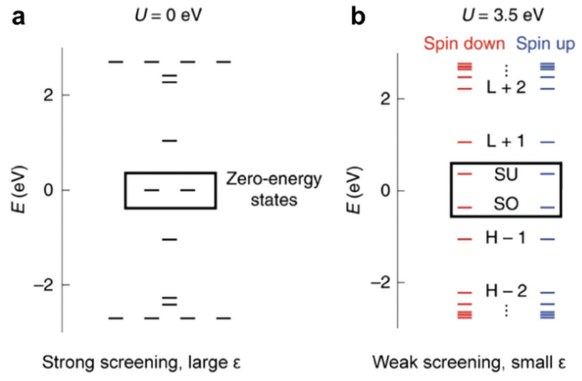

Fig. 19. General strategy for decoupling spins from metal substrates. Reproduced with permission [62]. Copyright 2019, Springer Nature.

zigzag edge extension were observed, which have the same origin as the zigzag end state of the 7AGNR.

2.5.3. Growth on semiconducting substrates

Growing magnetic graphene-based nanostructures directly on an insulating or semiconducting substrate is a great ideal method for achieving decoupling from a metal substrate, which provides a significant route for intrinsic fundamental physics explorations and future device applications. An outstanding example is displayed in Figs. 22a–c [169]. Atomically precise 7AGNRs were synthesized directly on TiO_2, a semiconducting metal oxide surface, relying on highly selective and sequential activations of carbon-bromine (C-Br) and carbon-fluorine (C-F) bonds (Fig. 22a). Two zigzag end resonances, showing a quasiparticle gap of approximately 2.45 eV, were localized within the energy gap of bulk 7AGNR states (Fig. 22c), in excellent agreement with previous reports about (7,n) GNRs on NaCl [166]. The measured quasiparticle gap was near the values expected for the freestanding system, revealing a weak interaction between the 7AGNRs and the TiO_2 substrate. Very recently, 7AGNRs as well as other large nanographenes synthesized on TiO_2(110) have also been reported [170]. Despite the low coverage and efficiency, these examples of successful on-surface synthesis of graphene nanostructures provide perspectives for the direct synthesis of magnetic graphene-based nanostructures on semiconductors or insulators.

2.5.4. Growth of second-layer GNRs

The above methods of decoupling spins from metal substrates actually face the common problem of low yields. Recent progress reported a strategy of direct growth of second-layer GNRs, utilizing the inert first layer to act as a self-decoupling layer between the second-layer GNRs and the metal substrate, as shown in Fig. 23 [171]. By rationally designing bowtie-shaped precursor molecules and taking advantage of strain-promoted domino-like cyclodehy-

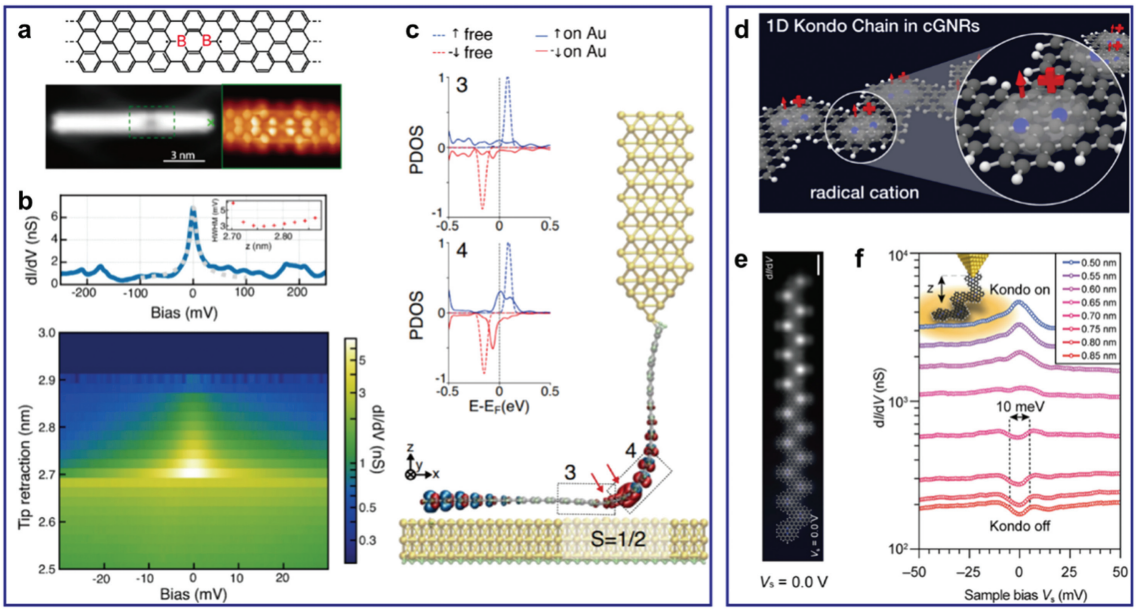

Fig. 20. (a) The chemical structure and STM images of 2B-doped 7AGNR. (b) Conductance through 2B-doped 7AGNR as a function of V_b and z, showing a narrow zero-bias resonance. (c) Simulation of the tip lifting process of the 2B-doped 7AGNR from the Au(111) surface, showing unquenched net spin. Model (d) and constant height d*I*/d*V* map at $V_s = 0.0$ V of N_2^+-cGNR (e), showing a 1D Kondo chain. (f) STS lift-off experiment performed on N_2^+-cGNRs. Reproduced with permission [131,165]. Copyright 2020, CC-BY 4.0; Copyright 2022, American Chemical Society.

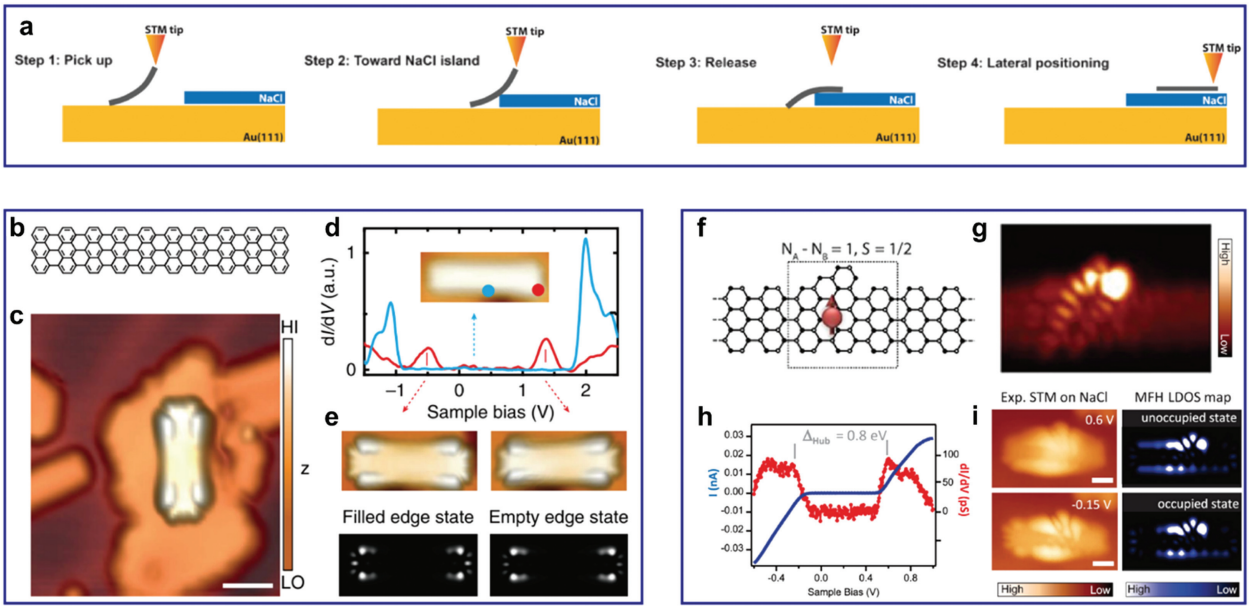

Fig. 21. (a) Sketch of the later tip-assisted manipulation procedure to transfer a ribbon from the Au(111) surface to a NaCl island. (b) Chemical structure of a (7,20) GNR. (c) STM topography image of a (7, 20) GNR transferred onto a NaCl monolayer island through STM manipulation. (d) Differential conductance spectra of the decoupled (7, 20) GNR. (e) Experimentally obtained and theoretically simulated filled and empty edge states. (f) Schematic structure of the proposed asymmetric edge extension (indicated by a dashed rectangle) along a 7AGNR backbone, which induces a local sublattice imbalance of 1 and a resulting total spin $S = 1/2$. (g) STM image obtained from the corresponding structure on Au(111). (h) Differential conductance (d*I*/d*V*-*V*) and simultaneously acquired current (*I*-*V*) spectra recorded above the edge extension, revealing a Hubbard gap of ~0.8 eV. (i) Experimentally obtained and theoretically simulated STM images. Reproduced with permission [166,168]. Copyright 2016, CC-BY 4.0; Copyright 2020, American Chemical Society.

drogenation reactions, the growth of second-layer 5/7-AGNRs is remotely triggered from the GNR parts directly adsorbed on the Au substrate *via* consecutively programmed C_{sp2}-C_{sp2} and C_{sp2}-C_{sp3} couplings (Figs. 23a and b). The quasifreestanding nontrivial nature of the second-layer 5/7-AGNRs was confirmed by measuring the quasiparticle energy gap of topological bands and the tunable Kondo resonance from topological end spins. The magnetic field evolution of the Kondo resonance at the end and the zero-energy map (Figs. 23c and d) indicated that the decoupling effect of the first-layer GNRs can provide suppressed but strong enough screening to induce the Kondo resonance, which is consistent with previous results of magnetic molecules on GNRs [172]. The achievement of the synthesis of second-layer GNRs may open an avenue toward diverse second-layer graphene nanostructures with different spin states and topological states for quantum computing and quantum sensing.

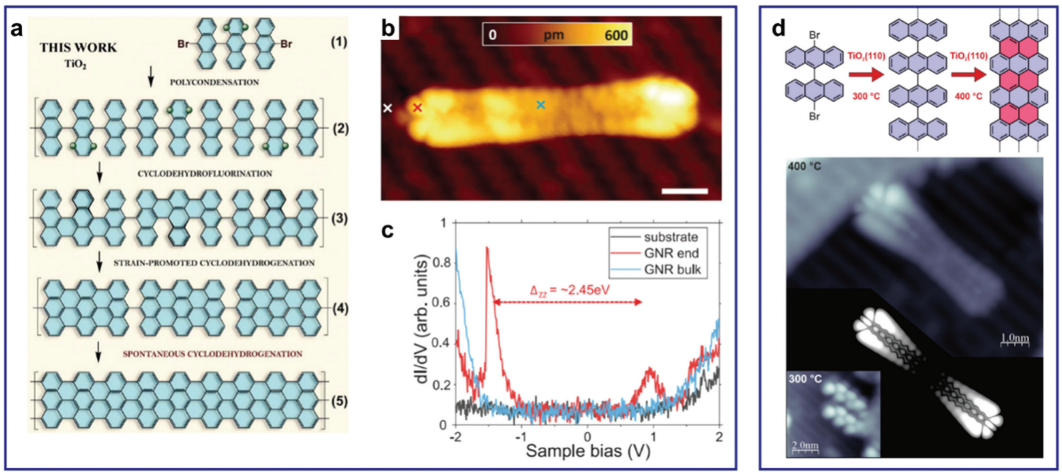

Fig. 22. (a) Multistep metal oxide surface-assisted strategies for the formation of extended GNRs. (b) High-resolution STM image of a 7AGNR synthesized on rutile (011). (c) d*I*/d*V* spectra obtained in locations marked in (b), showing that two resonances correspond to occupied and unoccupied zigzag end states. (d) Schematic illustration of synthetic paths and STM image of a 7AGNR fabricated on TiO_2(110). Reproduced with permission [169,170]. Copyright 2020, American Association for the Advancement of Science; Copyright 2023, CC-BY 4.0.

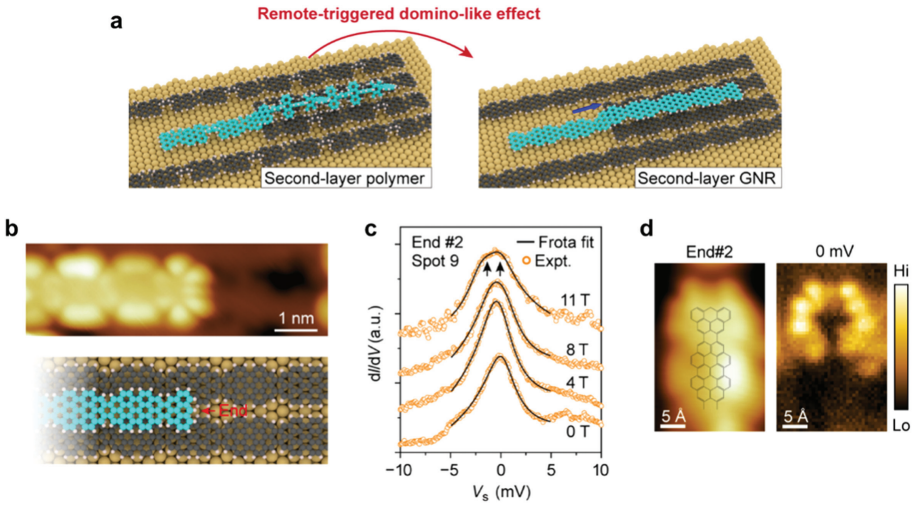

Fig. 23. (a) Sketch of the second-layer growth of the polymer and GNR following a domino-like effect. (b) STM image of the second-layer 5/7-AGNR end and the corresponding structural model. (c) Magnetic field evolution of the Kondo resonance at 4.2 K, showing splitting at 11 T. (d) STM image of the second-layer 5/7-AGNR end and the corresponding d*I*/d*V* maps at 0 meV. Reproduced with permission [171]. Copyright 2023, American Chemical Society.

3. Quantum information exploited by combining ESR and STM

3.1. Background of single-atom ESR

Over the past two decades, STM has been intensively used for studying individual and tailored spins carried by magnetic atoms or molecules. On surfaces, atomic/molecular spins can be assembled by STM tip with sub-nanometer precision to build artificial spin systems [173–175]. Together with magnetic field-dependent STS and spin-polarized (SP) techniques [176], the STM-based toolbox enables a variety of investigations of spin physics. In addition, single atomic spins are the smallest classical bit for data storage, which have attracted huge attention. In particular, great progress has been made in the study of spin excitation [177], which usually emerges when decoupling buffers, *e.g.* insulating thin films, are inserted between spins and the metallic substrate [178–180]. Spin on decoupling buffers is less affected by conduction electrons from the substrate, preserving spin states from scattering events and thus enhancing the spin lifetime. Loth *et al.* introduced direct-current (DC) pump-probe scheme to STM for measuring spin relaxation time T_1, paving the way for probing spin dynamics in the time domain [181].

Despite the fruitful achievements in this field, the quantum nature of spins has not been fully harnessed. Spin excitations studied by STM rely on inelastic tunneling, which is an incoherent process. Besides, the energy resolution of spin-flip spectroscopy is limited by temperature due to thermal broadening, typically ~1 meV. These shortcomings were overcome by the combination of ESR and STM (Fig. 24a), in which a microwave source was connected to the tunnel junction. The first STM-ESR was obtained on a Fe ($S=2$) atom adsorbed on bilayer MgO films [182]. ESR transition was driven between the lowest two energy levels when the frequency of the radio-frequency (RF) signal matched the Zeeman energy. ESR signal was detected by using SP-tip and lock-in techniques, similar to DC pump-probe scheme [181,183]. The authors observed a linear dependence between the resonance frequency f_0 and *z*-component (perpendicular to the sample plane) of the external magnetic field B_z (Fig. 24b). The typical linewidth (FWHM) of ESR spectra is ~10 MHz, which is four orders of magnitude better than spin-flip spectroscopy. Moreover, the coherence time T_2 of the

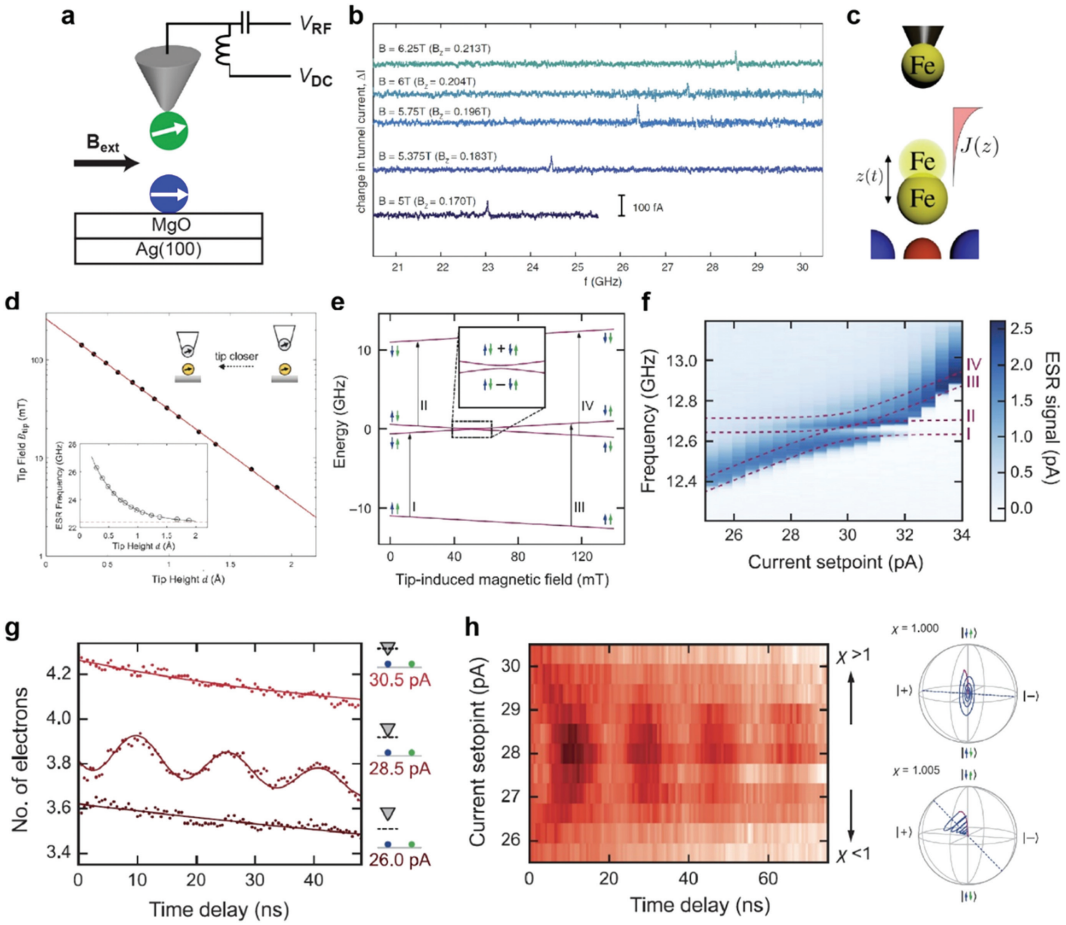

Fig. 24. (a) Simplified diagram for continuous-wave (CW) ESR. Radio-frequency (RF) signal V_{RF} is added to V_{DC} and transferred to the STM tunnel junction. A spin-polarized (SP) tip is used for the readout of the ESR signal. (b) ESR spectra of a single Fe atom under different external magnetic fields [182]. (c) The exchange-driven mechanism of single-atom STM-ESR. Two ingredients are AC electric field V_{RF} and exchange coupling $J(z)$ between SP-tip and the atom, both do not rely on a specific crystal field or a sizable spin-orbit coupling [185]. (d) Effective magnetic field $B_{tip} = J(z)/(g\mu_B S_{Ti})$ from the spin-polarized tip affects the Ti atom's resonance frequency when tip height is changed [189]. (e) Energy diagram and eigenstates of two coupled spin-1/2 particles as a function of B_{tip}. Near the tuning point, Zeeman product states $|10\rangle$ and $|01\rangle$ are coupled into superposition states $|+\rangle$ and $|--\rangle$ by the flip-flop interaction $J - D$. (f) ESR spectra at various tip heights, the tuning point appears at about $I_{DC} = 29$ pA. Dashed lines mark ESR transitions. (g) DC pump-probe measurements on a Ti dimer, with setpoints above, below, and at the tuning point. At the tuning point $I_{DC} = 28.5$ pA, $|+\rangle$ and $|--\rangle$ are formed and the identical Larmor frequencies of two Ti spins induce flip-flop oscillations. (h) Left: DC pump-probe measurements at different tip heights. Right: Free evolutions of the state vector on the Bloch sphere at different detuning ratios [190]. Reproduced with permission [182,185,189,190]. Copyright 2015, 2021, American Association for the Advancement of Science; Copyright 2017, American Physical Society.

spin can be estimated from the linewidth, which enables access to the quantum-coherent aspect of the spin [184].

The driving mechanism of STM-ESR is sketched in Fig. 24c. Two ingredients are AC electric field V_{RF} and exchange coupling $J(z)$ between SP-tip (with magnetic atoms at the apex) and the measured atom. When applying V_{RF} to the tunnel junction, the atom moves vertically and creates a small displacement Δz. The exchange coupling $J(z)$ is thus modulated due to its high sensitivity to the tip-atom distance and its gradient $\partial J(z)/\partial z$ drives ESR transitions [185], which is called piezoelectric coupling (PEC) mechanism. This mechanism is in analogy to what was used in electrically-driven ESR of quantum dots [186] and is well-supported by follow on experimental and theoretical works [31,187,188]. Notably, these two ingredients of STM-ESR do not rely on a specific crystal field or a sizable spin-orbit coupling, indicating that ESR-STM techniques can be applied to other systems as discussed below.

3.2. Magnetic interaction between coupled atomic spins

The unprecedented energy resolution and exquisite spatial resolution make ESR-STM an outstanding tool for probing magnetic interactions at the atomic scale. As discussed in Section 3.1, the SP-tip also has an exchange coupling $J(z)$ with the atom, which affects the resonance frequency f_0 of single-atom ESR when $J(z)$ is varied. Such tip effect was modeled as an effective magnetic field $B_{tip} = J(z)/(g\mu_B S_{Ti})$ (Fig. 24d), thus the total magnetic field B experienced by the atom is $B = B_{tip} + B_{ext}$. It should be noted that the magnetic atoms on the tip apex were treated classically in this simplified model, which holds in most cases [189]. An exception is introduced in Section 3.5.

When driving ESR of a Ti ($S = 1/2$) dimer, only the one underneath the SP-tip experiences B_{tip}, the system Hamiltonian can be written as:

$$H = g_1\mu_B\left(B_{tip} + B_{ext}\right)\cdot S + g_2\mu_B B_{ext}\cdot S + (J + 2D)S_{1z}S_{2z} + (J - D)\left(S_{1x}S_{2x} + S_{1y}S_{2y}\right) \quad (3)$$

where S is the spin operator of each Ti spin, J and D are the exchange and dipolar coupling strengths, B_{tip} only affects Ti-1 underneath the tip and adds to the Zeeman energy of Ti-1. The direction of B_{ext} is defined as the z-axis because $B_{ext} >> B_{tip}$. By choosing the Zeeman product basis: $|00\rangle$, $|10\rangle$, $|01\rangle$ and $|11\rangle$, the eigenstates and eigenvalues of this Hamiltonian are:

$$|00\rangle,\ E_{00} = \frac{J + 2D}{4} - \frac{\mu_B}{2}\left[g_1\left(B_{tip} + B_{ext}\right) + g_2 B_{ext}\right] \quad (4)$$

$$|+\rangle, E_+ = -\frac{J+2D}{4} + \frac{1}{2}\sqrt{(J-D)^2 + \left[\mu_B g_1\left(B_{tip}+B_{ext}\right) - \mu_B g_2 B_{ext}\right]^2} \quad (5)$$

$$|-\rangle, E_- = -\frac{J+2D}{4} - \frac{1}{2}\sqrt{(J-D)^2 + \left[\mu_B g_1\left(B_{tip}+B_{ext}\right) - \mu_B g_2 B_{ext}\right]^2} \quad (6)$$

$$|11\rangle,\ E_{11} = \frac{J+2D}{4} + \frac{\mu_B}{2}\left[g_1\left(B_{tip}+B_{ext}\right) + g_2 B_{ext}\right] \quad (7)$$

Although $|00\rangle$ and $|11\rangle$ are still eigenstates of H, $|10\rangle$ and $|01\rangle$ are mixed into superposition states $|+\rangle = \cos(\xi/2)\ |10\rangle + \sin(\xi/2)\ |01\rangle$ and $|-\rangle = \sin(\xi/2)\ |10\rangle - \cos(\xi/2)\ |01\rangle$, in which the mixing parameter $\xi = \arctan[\frac{J-D}{\mu_B g_1 (B_{tip}+B_{ext}) - \mu_B g_2 B_{ext}}]$ is determined by the ratio between flip-flop coupling $J-D$ and the difference of two Zeeman energies $\mu_B g_1 (B_{tip}+B_{ext}) - \mu_B g_2 B_{ext}$. Using ESR-STM, Yang *et al.* have demonstrated that B_{tip}, J and D can be determined and tuned, which allows for engineering eigenstates of the coupled spin system [189]. For instance, both J and D can be adjusted by tip manipulation to build strongly or weakly-coupled dimers. Besides, B_{tip} on one spin is easily varied by changing I_{DC}, enabling tuning the mixing parameter ξ to form Zeeman product states ($|10\rangle$ and $|01\rangle$) or singlet-triplet states ($|+\rangle$ and $|-\rangle$) Fig. 24f).

Singlet-triplet states were used for the demonstration of free coherent evolution of a weakly-coupled Ti dimer [190]. By precisely placing Ti spins on different bridge binding sites on MgO, the authors observed different g-factors between vertically and horizontally oriented Ti spins. In this case, a finite B_{tip} can compensate the Zeeman energy difference and thus reach the perfect tuning point $\xi = \arctan[\frac{J-D}{0}] = \pi/2$, where single-triplet states are formed and two Ti spins share the identical Zeeman energy. When performing DC pump-probe measurement at the tuning point, the state vector undergoes a Larmor precession in singlet-triplet state space, giving rise to oscillations at the flip-flop frequency $(J-D)/h$ (Figs. 24g and h). Note that the measurement utilized incoherent DC pulses to initialize and probe the quantum state of only one spin, observation of the two-spin state coherent evolution was essentially enabled by carefully designing the eigenstates using ESR-STM techniques. In addition, singlet-triplet states also have been utilized to construct clock transitions for longer coherence time [191], because the single-triplet subspace has zero magnetic quantum number and is thus robust to the magnetic noise.

On the other hand, when the mixing parameter $\xi = 0$, *i.e.* flip-flop coupling is much larger than the Zeeman energy difference, $|10\rangle$ and $|01\rangle$ become eigenstates of Eq. 3. The two spins are disentangled so that DC pump-probe measurement can only yield a simple exponentially decaying curve, corresponding to the relaxation process from $|10\rangle$ to $|00\rangle$. However, Zeeman product state is an essential ingredient when implementing multi-qubit operations to spins on a surface (see Section 3.6).

3.3. Hyperfine interaction of a single atom

Nuclear spin holds robust quantum coherence against noise from the environment, constituting an important candidate for quantum science and information processing [192–194]. In addition, analyzing the electron-nuclear interaction, *i.e.,* hyperfine interaction, provides information on the local electronic structure. In conventional STM/STS works, signals from the nucleus were obtained by detecting molecular motions and the energy resolution was not good enough to resolve hyperfine interaction [195,196]. In contrast, ESR-STM allows for the detection of hyperfine interaction within a single atom. The Hamiltonian is written as:

$$H = g_1 \mu_B B \cdot S + S \cdot A \cdot I + g_2 \mu_N B \cdot I + I \cdot P \cdot I \quad (8)$$

where S and I are electron and nuclear spin operators, A and P are hyperfine and electric quadrupole tensors, respectively. In this section, the nuclear Zeeman energy term $g_2 \mu_N B \cdot I$ is ignored because it is much smaller than other terms. Willke *et al.* observed 2-peak ESR spectra on 5 out of 147 Fe atoms, close to the natural abundance of 2.1% for ^{57}Fe ($I = 1/2$) [197]. Besides, isotopes ^{47}Ti ($I = 5/2$) and ^{49}Ti ($I = 7/2$) were also identified from the 6-peak and 8-peak ESR spectra, respectively. As shown in Fig. 25a, adjacent ESR peaks share the identical splitting Δf when measuring on bridge site Ti, indicating that P is negligible here. Interestingly, Δf decreased dramatically when Ti was moved to the oxygen site by atom manipulations and recovered upon moving back to the bridge site (Fig. 25b). This result suggests that hyperfine interaction reveals changes in the local chemical environment.

Moreover, two groups independently observed similar B field angle (θ)-dependent hyperfine interaction of Ti atoms on two different bridge binding sites. As shown in Fig. 25c, results measured on vertical and horizontal bridge sites show clear differences, which can be interpreted by considering anisotropies of the A tensor and g-factor. Since the principal values of A and g-factor can be obtained by fitting ESR spectra, Kim *et al.* and Farinacci *et al.* were able to determine the shape of the electron ground state using DFT simulations and a point-charge-based model, respectively [198,199]. These two methods reached a good agreement, paving the way to determine the local electronic structure at the single-atom level.

Resolving hyperfine interaction provides opportunities to address nuclear spin [193], which rarely interacts with the environment and is hence difficult to manipulate directly. ESR spectra of Cu, including both ^{63}Cu ($I = 3/2$) and ^{65}Cu ($I = 3/2$), show hyperfine interactions that are two orders of magnitude larger than Ti [200]. DFT calculations show that the strong hyperfine interaction originates from the large s-electron density at the nucleus, which induces hybridizations between eigenstates (Zeeman product states). As shown in the upper panel of Fig. 25d, there are eight eigenstates $|i\rangle$ (i =1 to 8), and two types of hybrid states under V_{DC} = -22 mV: (i) hybridizations between ($|1\rangle$, $|7\rangle$), ($|2\rangle$, $|6\rangle$) and ($|3\rangle$, $|5\rangle$), labeled as dashed arrows, during which the spin of the tunneling electrons is conserved ($\Delta\sigma = 0$) (ii) hybridizations between ($|1\rangle$, $|8\rangle$), ($|2\rangle$, $|7\rangle$), ($|3\rangle$, $|6\rangle$) and ($|4\rangle$, $|5\rangle$), labeled as solid arrows, during which the spin of the tunneling electrons is reversed ($\Delta\sigma = \pm 1$). Under a negative bias, the SP-tunnel current mainly consist of spin-up state electrons with $\sigma = 1/2$, which induce angular momentum transfer $\Delta\sigma = +1$ from the upper to the lower sector (Fig. 25d, upper panel). The combined $\Delta\sigma = 0$ and $+1$ process transfer the state population to $|4\rangle$, corresponding to the large peak in the ESR spectrum. When applying a positive bias V_{DC} = +22 mV, the population transfer becomes opposite and $|8\rangle$ has the predominant population, as shown in the lower panel of Fig. 25d. The authors achieved ~17 times enhancement over the thermal equilibrium at 1 K, which corresponds to an effective temperature of 200 mK. Because of the strongly polarized states, the authors were able to measure NMR spectra, in which three peaks were resolved (Fig. 25e). NMR signals are detected by the change of electron spin polarization induced by NMR transitions. This work demonstrates the polarization, driving, and detection of nuclear spin, which highlights the potential of ESR-STM in manipulations of electron-nuclear systems.

3.4. Coherent manipulations of a single atomic spin-qubit

With the development of modern information technology, the miniaturization of devices reaches the nanometer scale [201]. In

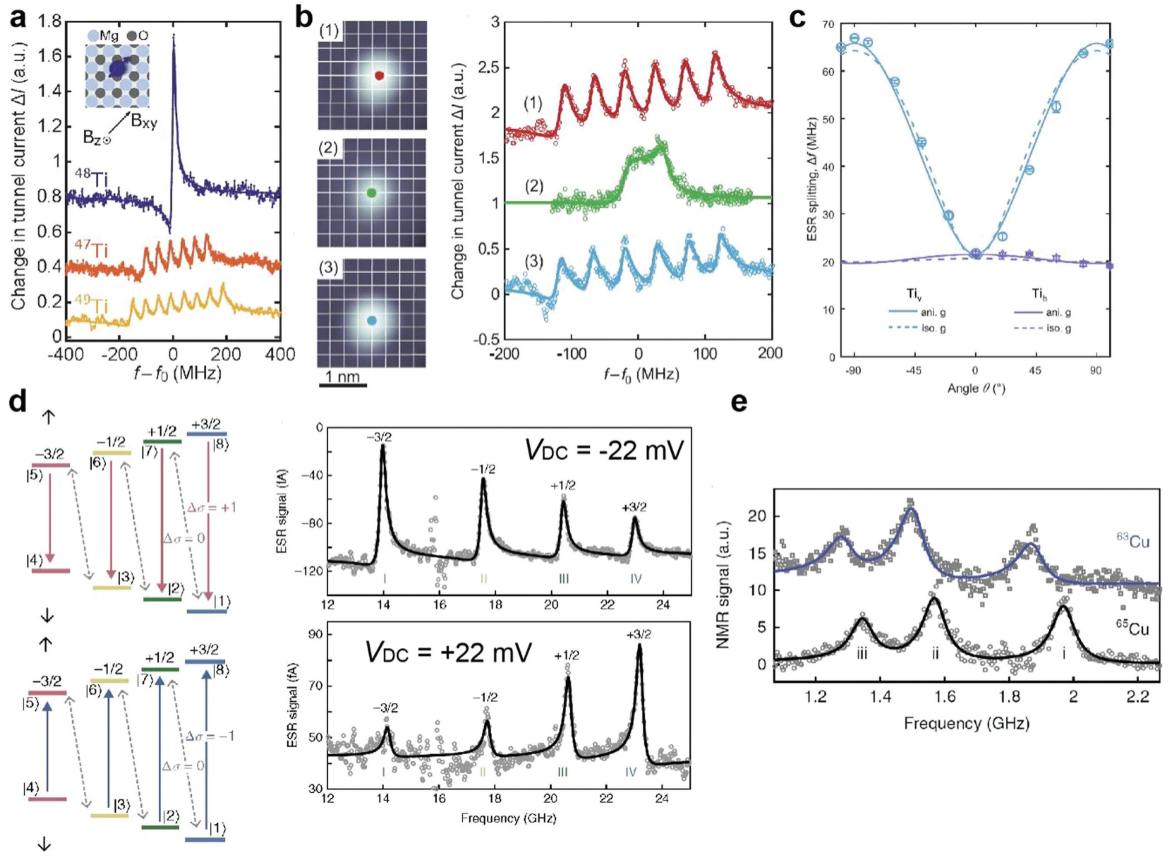

Fig. 25. (a) Resolving hyperfine interaction from ESR spectra, measured on ^{48}Ti (blue, $I=0$), ^{47}Ti (red, $I=5/2$), and ^{49}Ti (orange, $I=7/2$) on bridge site. The splitting Δf between adjacent peaks is identical, suggesting zero interaction from electric quadrupole P. (b) Site-dependent hyperfine interaction. The splitting Δf decreased dramatically when Ti was moved to the oxygen site by atom manipulations and recovered upon moving back to the bridge site [197]. (c) Anisotropic hyperfine interaction from fitting ESR spectra under varying angles θ of the external magnetic field B. ESR spectra are measured on Ti_v (vertical bridge site) and Ti_h (horizontal bridge site), showing different behaviors due to the change in local environments [198]. (d) Polarization of nuclear spin by SP-tunnel current, under positive (upper panel) and negative (lower panel) bias. Two types of hybridizations are labeled by dashed and solid arrows. (e) NMR spectra of ^{63}Cu and ^{65}Cu. The transitions are at slightly different frequencies although the two isotopes both have $I=3/2$ [200]. Reproduced with permission [197,198,200]. Copyright 2018, Springer Nature; Copyright 2018, American Association for the Advancement of Science; Copyright 2022, CC-BY 4.0.

light of the quantum phenomenon occurring at such a length scale, quantum information processing (QIP), which utilizes the quantum-coherent properties of individual spins, defects, or photons, has stood out as a new class of information technology [202]. In the recent three decades, many qubit platforms have been developed and used for the demonstration of quantum computing. On the other hand, spins on surfaces can be arranged into on-demand nanostructures with Å precision and are natural candidates for QIP. However, realizing quantum control of the spin states remains a challenge.

By using ESR-STM, the quantum nature of spins becomes accessible as discussed above. For the next step, resonant ESR pulses are required to perform coherent spin manipulations. The experimental setup of single-spin pulsed ESR measurements is sketched in Fig. 26a, in which a vector RF generator is gated by an arbitrary waveform generator (AWG). The duration and phase of RF pulses are controlled through programming AWG and each RF pulse corresponds to a single-qubit rotation. Considering an RF pulse with duration τ and phase φ, it performs a single-qubit rotation $R_\varphi(\theta=\Omega\tau)$ on the Bloch sphere, as shown in Fig. 26b. Start from the ground state $|0\rangle$, the state vector is rotated by $\theta=\Omega\tau$ about the axis defined by the angle φ to the x-axis in the x-y plane, reaching to the state: $\cos(\theta/2)|0\rangle+e^{i\varphi}\sin(\theta/2)|1\rangle$. Here Ω is the Rabi rate and φ is defined by the phase difference between two RF pulses (see below).

The first pulsed ESR result [203] was measured on Ti spin ($S=1/2$) with phase-fixed RF pulses ($\varphi=0$). Rabi oscillations were observed by varying pulse duration at the resonance frequency, the signal can be fitted to an exponential decaying cosine function:

$$\Delta I = I_0 \cdot \exp\left(-\frac{\tau}{T_2^{Rabi}}\right)\cdot\cos(\Omega\tau)+I_{\text{offset}} \tag{9}$$

As shown in the left panel of Fig. 26c, Rabi oscillations with increasing V_{RF} show a linear dependence between Ω and V_{RF}, as observed in other qubit platforms. Besides, the coherence time T_2^{Rabi} decreases when increasing I_{DC}, which is induced by decoherence effects from tunneling electrons. Qubit performance was characterized by Ramsey and spin echo measurement. The coherence time $T_2^{Echo}=190$ ns is much longer than $T_2^{*}=40$ ns, revealing that the slow magnetic field fluctuation is another decoherence source [204].

Yang *et al.* attributed the pulsed ESR signal ΔI to homodyne detection (the right panel of Fig. 26c), in which x and y-components of the spin state were probed by V_{RF} [203]. In contrast, a recent work demonstrated that DC detection which probed the z-component of the spin state through V_{DC}, was the predominant mechanism in pulsed ESR [205]. Such distinction is probably from the different B_{tip} orientations, which determine the ratio between DC and homodyne signals. For simplicity, we assume an SP-tip that is suitable for DC detection. The pulsed ESR signal ΔI of an arbi-

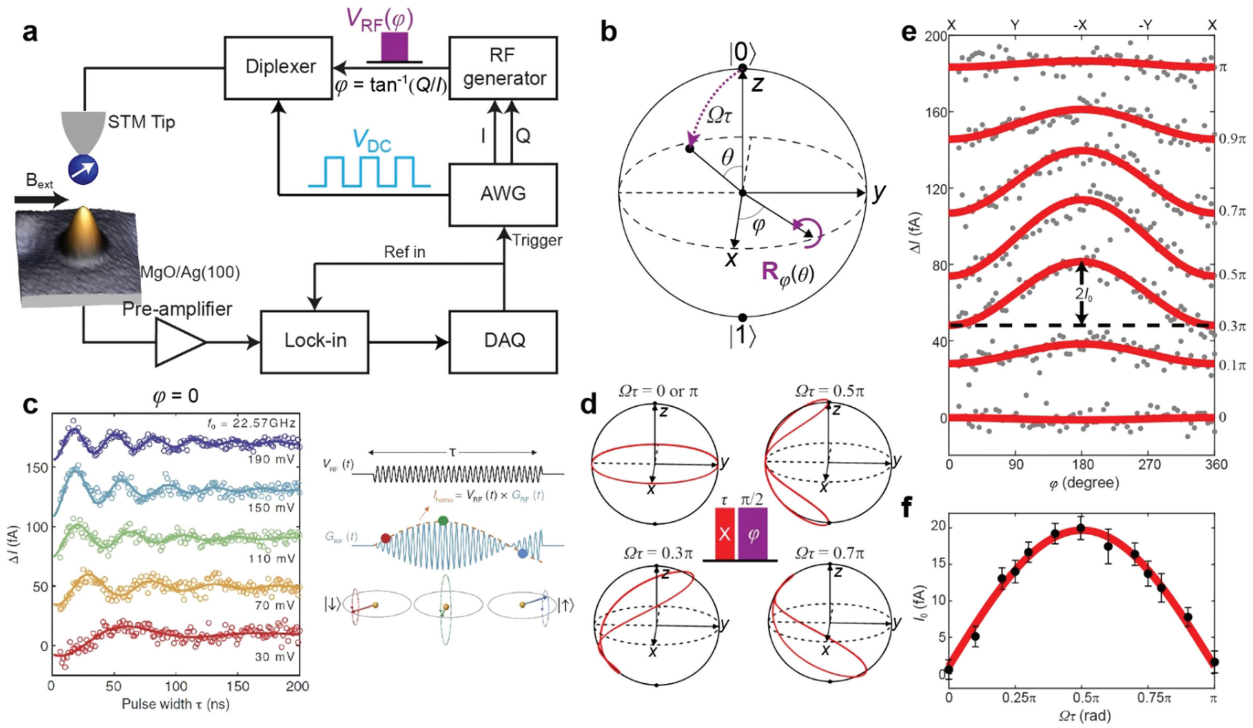

Fig. 26. (a) Experimental setup for quantum control of an atomic spin qubit. A vector RF generator is used for generating phase-controlled RF signals. (b) A single-qubit rotation $R_\varphi(\theta)$ of $\theta = \Omega\tau$ about an axis of angle φ from the x-axis. θ and φ are determined by the pulse duration and the phase difference between two RF pulses, respectively. (c) Left: Rabi oscillations measured with a varying V_{RF}, qubit is rotated about the x-axis on the Bloch sphere ($\varphi = 0$). Right: Homodyne detection of the Rabi signals. G_{RF} is the instantaneous tunnel conductance when V_{RF} is on [203]. (d) Pulse sequence for two-axis control where the phase φ of the second pulse (purple) is swept between 0 and 2π. Four simulated trajectories (different durations of the red pulse) of the qubit's final state are illustrated on the Bloch sphere. (e) ESR signals measured with the sequence in (d) for 7 different $\Omega\tau$ (labeled at right side). Solid curves are cosine functions $\Delta I = -I_0\cos\varphi$. (f) I_0 as a function of $\Omega\tau$, extracted from the fits of 13 curves. Solid curve is a sinusoidal fit [205]. Reproduced with permission [203,205]. Copyright 2019, American Association for the Advancement of Science; Copyright 2023, CC-BY 4.0.

trary single-spin state is:

$$\Delta I \propto \left|\cos(\theta/2)\right|^2 - \left|e^{i\varphi}\sin(\theta/2)\right|^2 = \cos\theta \tag{10}$$

Showing an agreement with Rabi signals in Fig. 26c. Note that ΔI is independent of RF phase φ, which is a trivial result due to the arbitrariness of φ in a single wave.

Implementing phase-controlled RF pulses requires a two-pulse sequence, in which the first pulse "defines" the x-axis ($\varphi = 0$) and the phase difference between two pulses determines φ. An example is illustrated in Fig. 26d, a sequence with two control parameters: duration $\tau \in [0,\pi]/\Omega$ of the first pulse and the phase $\varphi \in [0,2\pi]$ of the second pulse. The simulated trajectories of the spin's final state with respect to φ are shown on the Bloch sphere, demonstrating significant differences between $\Omega\tau = 0$ or π, 0.3π, 0.5π and 0.7π cases. Spectra measured by such sequence are illustrated in Fig. 26e, solid curves are $\Delta I(\varphi) = -I_0\cos\varphi$ [206]. From Fig. 26d, the height $2I_0 = |\Delta I(\pi) - \Delta I(0)|$ of each curve varies with the duration τ and the maximum height occurs when $\Omega\tau = 0.5\pi$ ($|0\rangle$ and $|1\rangle$), in agreement with the result in Fig. 26e. Moreover, the results for $\Omega\tau$ and $(\pi - \Omega\tau)$ are equivalent to each other under DC detection, *e.g.* results correspond to $\Omega\tau = 0.7\pi$ and 0.3π. The authors further plotted I_0 extracted from 13 curves against $\Omega\tau$, as shown in Fig. 26f. Data shows a clear $\sin\Omega\tau$ dependence (red curve) as predicted from the simulations. Obviously, varying the two control parameters τ and φ can lead to any quantum state on the Bloch sphere [207], demonstrating the ability to generate arbitrary single-qubit superposition states.

3.5. Molecular qubits

We have introduced complete qubit control of a single atomic spin (Ti) by ESR-STM in Section 3.4, making an important step forward in utilizing spins on surface for QIP. Extending the same technique to other spin-carrying species is desirable. To this end, Zhang *et al.* deposited iron phthalocyanine (FePc) molecule onto bilayer MgO films and found FePc was $S = 1/2$ species and suitable for ESR-STM measurements [208]. DFT calculations suggested that when adsorbed on MgO, FePc molecule was charged by one electron from Ag substrate and formed a $S = 1/2$ system. The local DOS of charged FePc highlighted the unpaired d_{z^2} orbital, which was different with Ti spin. Besides, the charged FePc orbital configurations on MgO were similar with those in vacuum, which demonstrated a weak interaction between FePc and substrate.

ESR measurement on single charged FePc (in the following simply referred to as FePc) revealed that FePc had a magnetic moment of 1 μ_B, similar to Ti spin [189]. In contrast, measurements on FePc dimers demonstrated different results from those on Ti dimers. As shown in Fig. 27a, FePc molecules have two orientations on MgO, forming two types of FePc dimers: (3, 4) and (5, 0). From STM images at left, two dimers share the same Fe-Fe distance but have different lobe-lobe distance. When measuring ESR under a pure $\boldsymbol{B}_z$ field, the authors observed significant different peak splitting on the two dimers, as shown at the right of Fig. 27a. By rotating $\boldsymbol{B}$ field, the exchange and dipolar coupling strength of (3, 4) dimer were extracted from ESR spectra: $J = 133$ MHz and $\boldsymbol{D} = 16$ MHz. The result suggested that the exchange coupling was the dominant interaction in FePc dimers, which should be identical in (3, 4) and (5, 0) dimers.

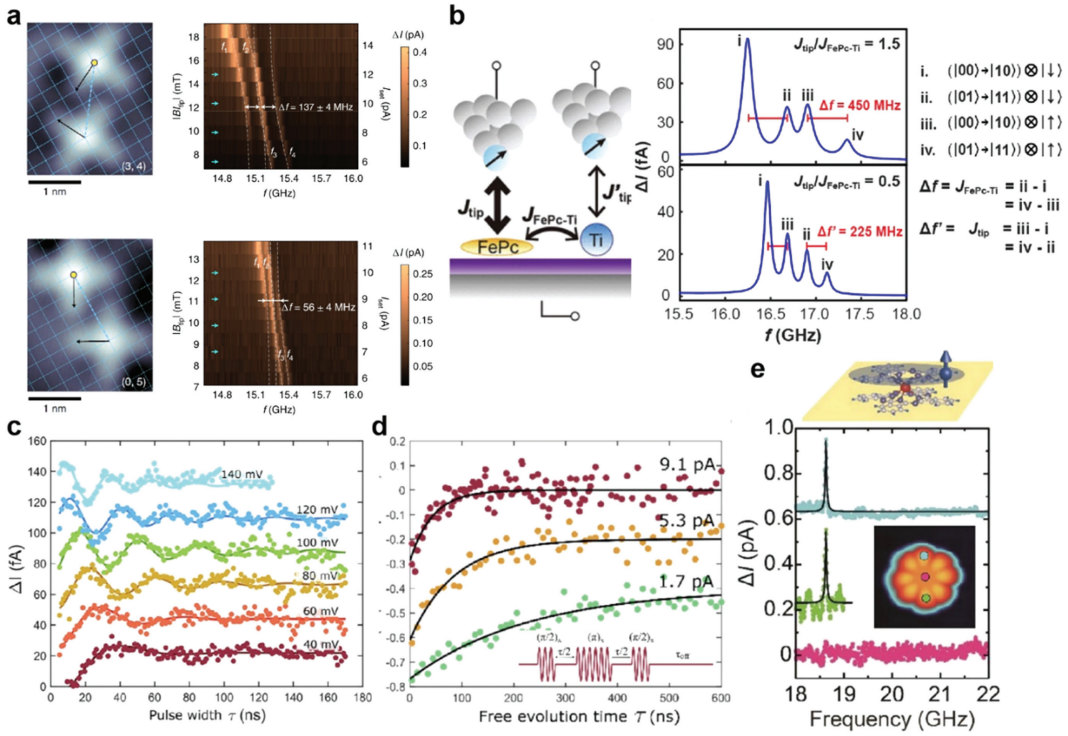

Fig. 27. (a) ESR spectra of FePc dimers in configuration (3, 4) (upper) and (0, 5) (lower). These dimers share the same Fe-Fe distance (dashed lines) but different lobe-lobe distance. The grids indicate the oxygen sites of MgO surface. ESR spectra plotted in a color scale measured at different B_{tip} (I_{set}), showing clearly the difference in the coupling strength [208]. (b) Tip-dependent ESR splitting measured on FePc-Ti heterodimers. The difference in Δf is caused by a different interaction energy between the tip and each spin of the dimer [210]. (c, d) Rabi oscillations (c) and spin echo measurements (d) of a single FePc molecule. Experimental setup is the same as Fig. 26a [211]. (e) ESR signal of a π-radical spin located on the lobes of a $TbPc_2$ molecule adsorbed on NaCl films [213]. Reproduced with permission [208,210,211,213]. Copyright 2023, American Chemical Society; Copyright 2021, Springer Nature; Copyright 2021, 2022, CC-BY-NC-ND 4.0.

However, unlike atomic spins, FePc cannot be treated as point magnet due to spin distributions on the lobes. DFT calculations revealed that d_{z^2} orbital of the central Fe had 71% spin distributions and 29% contributions were from the ligands and other orbitals. The authors claimed that the non-negligible spin density on the outer ligands of the molecule might produce such a difference by generating additional coupling path for the intermolecular magnetic interaction. The result implies that the distance between nearby ligands plays a crucial role in magnetic coupling energy. Since the ligands can be functionalized by chemical methods [209], this result also allows for building more flexible magnetic nanostructures on a surface.

In a follow on work, in which FePc-Ti hetero dimers were measured, the authors observed that the splitting Δf of the FePc-Ti dimer appeared to differ significantly depending on whether the tip was located on Ti or FePc [210]. By measuring dozens of FePc-Ti dimers with various tips, they found roughly 50% of the ESR-active tips showed identical ESR splitting within the error bars on either spin. While for the other ESR-active tips, the splitting Δf reduced by ~50% when the tip was positioned on the Ti atom (Fig. 27b). Notably, such tip-dependent splitting Δf only appeared in FePc-Ti hetero dimers while Δf obtained on homo dimers (Ti-Ti and FePc-FePc) revealed no tip-dependence. A model was established for interpretation, in which the SP-tip was modeled as S_{tip} rather than B_{tip} in Eq. 3. Two states of S_{tip} ($|\downarrow\rangle$ and $|\uparrow\rangle$) were considered, which doubled the ESR transitions. The number of observed peaks in ESR spectra was reduced by the degeneracies, leading to misinterpretation of magnetic interaction. The reason that tip-dependent Δf only appeared FePc-Ti dimers was because of the different exchange coupling between tip and each spin. As shown in Fig. 27b, the ratio between tip-induced exchange coupling J_{tip} and measured FePc-Ti coupling $J_{FePc\text{-}Ti}$ determined the alignment of ESR transition. When $J_{tip}/J_{FePc\text{-}Ti} = 0.5$, ESR transitions correspond to $|\downarrow\rangle$ and $|\uparrow\rangle$ states becomes overlapped, the spitting Δf between adjacent peaks, which is the conventional way for extracting magnetic interactions, yields incorrect results. Although only half of the SP-tip in this work showed such tip-dependent Δf, the S_{tip} model provided a comprehensive reference for characterizing tip features in ESR-STM measurements especially for hetero-spin systems.

The works on FePc-FePc and FePc-Ti dimers lay the foundation for studying molecule-based spin systems or metal-organic coordination networks using ESR-STM. The $S = 1/2$ nature of FePc on MgO also allows for coherent spin manipulation [211], as is demonstrated on single Ti spin. Rabi oscillations measured with increasing V_{RF} on a single FePc are shown in Fig. 27c. The result is similar to Ti Rabi oscillations in Fig. 26c, despite of the different orbitals. Spin echo measurements at varying I_{DC} show a clear dependence between T_2^{Echo} and I_{DC}, in agreement with previous works. The authors further measured T_2^{Echo} as a function of the number of neighbored molecule, showcasing the use of ESR-STM on studying expanded spin systems.

Efforts to search new ESR-active spin species are ongoing, alkali metal dimers [212] and π-radical on $TbPc_2$ [213] have both enabled ESR-STM measurements. In particular, unlike alkali metal dimers and FePc, which changed from $S = 1$ to $S = 1/2$ upon deposition on bilayer MgO, the π-radical that located on the lobes of $TbPc_2$ has been preserved on bilayer NaCl. This result demonstrates that STM-ESR does not rely on specific substrate like MgO and the $S = 1/2$ Ti on MgO may originate from the same charge effect. Resolving ESR of the delocalized π-radical on the lobes highlights the potential of extending ESR-STM techniques on other π-radical systems, such as nanographene [70].

3.6. A multi-qubit platform on a surface

As introduced in Sections 3.4 and 3.5, ESR-STM has enabled coherent control of a single electron spin that yet to be achieved by conventional STM/STS techniques. The SP-tip plays a crucial role in both driving and detecting STM-ESR, but also limits this technique to a single spin in the tunnel junction. Utilizing spins on surfaces for QIP requires driving and detecting multiple qubits that outside of the tunnel junction, which is remained elusive. To this end, efforts are made on developing new ESR driving method within the frame of PEC mechanism, in which the key ingredients are ac electric field V_{RF} and tip-atom exchange coupling $J(z)$. Although V_{RF} is thought to have a radiation range of tens of nanometers, $J(z)$ is extremely localized and only affects the spin in the tunnel junction. A nearby Fe atom was placed 0.6-0.8 nm away from a Ti spin to provide exchange coupling [203]. The authors observed a non-zero Rabi rate Ω_0 when the tip was nearly retracted. The Ω_0 was found to be strongly dependent on Fe-Ti distance and enhanced when an additional Fe was placed nearby. This work demonstrated that the J provided by Fe on the surface was sufficient to substitute that from the SP-tip, opening an avenue for driving ESR transitions of spins that remote from the tunnel junction.

Based on this effort, a recent work has achieved bottom-up construction, qubit operations, and readout of multiple electron-spin qubits using an ESR-STM [214]. The qubit architecture is sketched in Fig. 28a: a Ti spin is driven and detected by SP-tunnel current as in other works, serving as the sensor qubit; each remote qubit is constructed by positioning an Fe atom ∼0.6 nm away from Ti for ESR driving [203]. For detections of remote qubits, eigenstates were engineered to nearly pure Zeeman product states (Fig. 28b) and pulsed double electron-electron resonance (pDEER) technique was implemented. As shown in Fig. 28c, a sequence consist of two RF pulses was used for pDEER, including a control pulse (red) and a sensing pulse (blue) acting on the remote and sensor qubit, respectively. The control pulse was applied first and its frequency f_R was swept, followed by the sensing pulse applied at f_1 (f_2) to monitor the population of state $|0\rangle$ ($|1\rangle$) of the remote qubit. When f_R matched f_3 or f_4, the population change induced by the control pulse resulted in a detectable increase (decrease) of the sensing pulse applied at f_1 (f_2). The pDEER technique enabled measuring resonance frequencies of the remote qubit although the SP-tip was positioned on the sensor qubit.

Due to the constant qubit-qubit coupling, single-qubit (unconditional) operation that independent of other qubit's states requires driving all the ESR transitions (f_3 and f_4) simultaneously. Since the eigenstates were Zeeman product states, f_3 and f_4 were driven with the same strength to realize single-qubit operation, as shown in Fig. 28d. In addition, the authors performed unconditional two-axis control of the remote qubit, which allowed for arbitrary single-qubit gates in the two-qubit system. In contrast, controlled (conditional) operation was straightforward because only one ESR transition of the remote qubit had to be excited.

Knowing the CNOT time from controlled operation, the authors further coherently controlled both sensor and remote qubits to demonstrate a CNOT gate. In Fig. 28e, it illustrates the result of controlled rotations of the sensor qubit by driving f_1 (blue) and f_2 (cyan), corresponding to qubit rotations conditional on $|0\rangle$ and $|1\rangle$ states of the remote qubit, respectively. The measurement was performed at ∼0.4 K and predominant population was in the state$|0\rangle$, resulted in visible oscillations only in the blue curve which was conditional on $|0\rangle$ state of the remote qubit. When a CNOT was applied at f_3, the population of the state $|0\rangle$ was transferred into the state $|1\rangle$ and thus induced opposite trends of the oscillations (Fig. 28f). This result is the first demonstration of a CNOT gate with spins on a surface, together with the single-qubit operation, it is now in principle possible to generate two-qubit entangled states, *e.g.* by applying a Hadamard gate to the sensor qubit followed by a CNOT gate acting on the remote qubit.

Controlled-controlled operation in an extended system has also been demonstrated. Using atom manipulation, a three-qubit system composed of a sensor qubit and two remote qubits (referred to as RQ1 and RQ2) was constructed, as sketched in Fig. 28a. The eigenstates were again engineered to nearly pure Zeeman product states by precisely placing atoms and a vector magnetic field. An energy level diagram and ESR transitions used for controlled-controlled operation are shown in Fig. 28g. The transition $|0\rangle|00\rangle \leftrightarrow |0\rangle|10\rangle$ (red arrow) was driven to rotate RQ1 when the sensor qubit and RQ2 are both in the state $|0\rangle$. The signal was sensed by all the four ESR transitions of the sensor qubit (blue arrows), appearing as two oscillations curves and two featureless curves, as shown in Fig. 28h. Apparently, the two oscillating curves were detected by sensing pulses that read the population change of remote qubits' state $|00\rangle$ (magenta) and $|10\rangle$ (orange). While the other two curves reflected population changes in state $|01\rangle$ and $|11\rangle$, which were not involved in controlled-controlled operation ($|0\rangle|00\rangle \leftrightarrow |0\rangle|10\rangle$).

Lastly, the relaxation and coherence properties of the remote qubit were characterized in a two-qubit system. By performing an inversion recovery measurement, the relaxation time T_1 of the remote qubit was obtained as 166 ± 14 ns, showing slight improvements over the conventional DC pump-probe result. The latter was potentially affected by the scattering events between tip and substrate although the tunnel current was almost zero. The authors further observed I_{DC}-independent ${T_2}^{Echo}$ from spin echo measurements. In particular, the result ${T_2}^{Echo} \approx 300$ ns approached the theoretical limit of $2T_1 \approx 330$ ns, suggesting that the coherence time after noise-filtering was limited by the short relaxation time, which can be easily enhanced by using thicker MgO layers.

4. Topology properties of surface organic structures

The discovery of graphene has inspired a fast-growing field of two-dimensional (2D) materials [215–219]. In particular, 2D topological insulators have received significant attention because symmetry protected conducting edge states provide promising platforms for exploring fundamental sciences as well as for the realization of multifunctional topological devices in spintronics, quantum computation and information processing [215,220–225].

The nontrivial band topology is currently received significant attention in the study of 2D TIs. The band topology can be identified by calculating its topological invariant. Each band has a topological invariant that is zero for topologically trivial cases and nonzero for topologically nontrivial cases. It is predicted that both Dirac and flat bands have a so-called nontrivial band topology. The Dirac and flat bands generally arise in 2D lattices with special lattice symmetry. It is known that the Dirac band generally arise in a 2D honeycomb lattice [222], and the flat band usually forms in a geometrically frustrated lattice, such as Kagome (corner-shared triangle) and Lieb (edge-centered square) lattices [226–230], as shown in Figs. 29a–c.

We start with generic tight-binding (TB) models in the three basic 2D lattices to understand the relation between lattice symmetry and band structure as well as their associated intriguing quantum states. Neglecting the on-site energy difference between the sublattices and considering only nearest-neighbor (NN), the TB spinless Hamiltonian can be simply written as:

$$\hat{H} = \sum_i \varepsilon_i c_i^\dagger c_i - t_{ij} \sum_{ij} \left(c_i^\dagger c_j + H.c. \right) \tag{11}$$

where ε_i is on-site energy at the i^{th} site. $c_i^\dagger$ and c_i are electron creation and annihilation operators at the i^{th} site, respectively. $<i, j>$ denotes the NN hopping with hopping parameter t_{ij}.

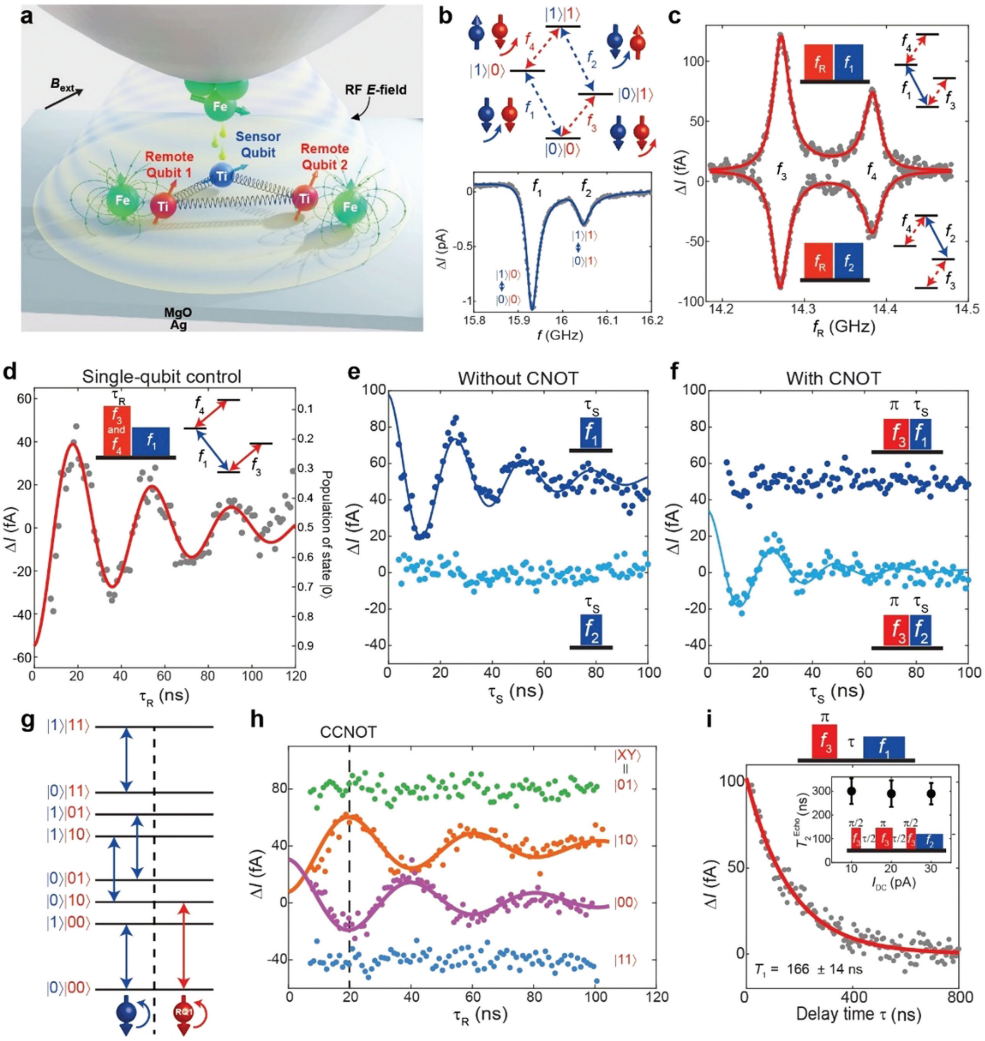

Fig. 28. (a) Schematic of a multi-qubit platform on a surface: A sensor spin qubit (Ti, blue) is in the tunnel junction and used for readout. Each remote qubit is composed of a Ti atom (red) and a Fe atom (green). (b) Upper: Energy diagram and ESR transitions of a two-qubit system. Lower: ESR spectrum of the sensor qubit. (c) ESR spectra of the remote qubit measured with the tip positioned on the sensor qubit. Sensing pulse (blue) reads the population change of the joint state induced by control pulse (red). Insets: Pulse sequences and involved transitions. (d) Single-qubit control of the remote qubit, realized by driving both transitions (f_3 and f_4) with the same driving strength. (e, f) Controlled rotations of the sensor qubit without (e) and with (f) a CNOT gate at $f_R = f_3$ on the remote qubit. The CNOT gate transferred the predominant population from state $|0\rangle|0\rangle$ to state $|0\rangle|1\rangle$, thus causing the opposite trends of the oscillations. (g) Energy diagram of a three-qubit system and ESR transitions used for the measurement in (h). (h) Controlled-controlled operation of RQ1 performed by driving the transition $|0\rangle|00\rangle \leftrightarrow |0\rangle|10\rangle$ (red arrow in (g)). Four different frequencies of the sensor qubit were used for sensing the four remote qubit states (blue arrows in (g)), the detected states of the remote qubits are labeled. (i) Inversion recovery measurement of a remote qubit, yielding a relaxation time T_1 of 166 ± 14 ns. Inset: Results of spin echo measurements with different I_{DC} (tip height). The coherence time $T_2^{Echo} = 300 \pm 54$ ns is independent of I_{DC} and approaching the theoretical limit of $2T_1$. Reproduced with permission [214]. Copyright 2023, American Association for the Advancement of Science.

TB model of a honeycomb lattice gives rise to two Dirac bands, as shown in Fig. 29d. After considering spin-orbital coupling (SOC) effect, a nontrivial gap opens at the Dirac points, changing the system from a topological semimetal into a TI. The band structure of a Kagome lattice exhibits three bands with one flat band located either below or above two Dirac bands depending on the sign (positive or negative) of lattice hopping (Fig. 29e). Similarly, further including of SOC effect, the Dirac points at K(K′) and band degenerate point at Γ will be gapped, leading to TI states. In addition to the Kagome lattice, Lieb lattice also hosts Dirac and flat bands (Fig. 29f). Ideal Lieb band structure shows one perfect flat band crossing the middle of Dirac bands only if it has same on-site energies for the corner and edge-center sites and negligible second nearest-neighbor lattice hopping. For this reason, realistic materials host Lieb band structures are quite rare.

The 2D organic frameworks have the advantages of low cost, easy fabrication and mechanical flexibility, becoming a hot topic in on-surface chemistry. With the rapid progress in synthesis chemistry, there exists a very large family of 2D organic materials [231–238]. Many of them exhibit high-symmetry lattices, such as honeycomb [239], Kagome [240], Lieb lattice [241] and rhombus lattices [242], which is promising to host non-trivial band topology, as shown in Fig. 30.

Especially, considering the extraordinary diversity of coordination chemistry that will provide countless combinations of metal ions and organic linkers, to offer a rich variety of lattice, orbital, and spin symmetries [243]. Moreover, strongly correlated localized *d* and *f* electrons of metal ions and diffusive *s* and *p* electrons of molecular linkers, leading to more exotic topological and magnetic properties. Furthermore, the substitution of the metal atoms with other metal atoms of different oxidation provides a platform to tune the location of topological states without extra electron or hole doping.

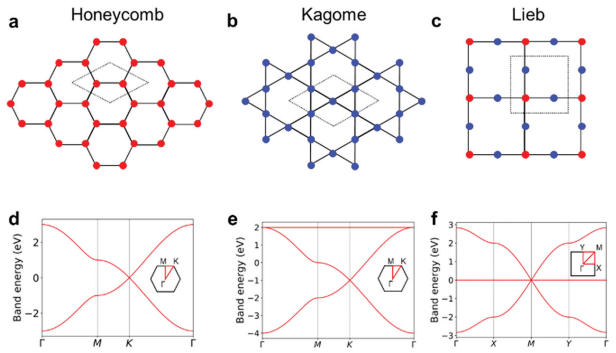

Fig. 29. TB models and electronic properties of three basic 2D lattice. (a-c) Lattice structures of honeycomb, Kagome and Lieb lattices, respectively. Corresponding band structures calculated with the nearest-neighbour tight-binding model and insets are the Brillouin zones. The on-site energy is set to be zero, and nearest neighbour hopping strength t is set to be 1 eV. (d-f) Band structures of honeycomb, Kagome and Lieb lattices, respectively.

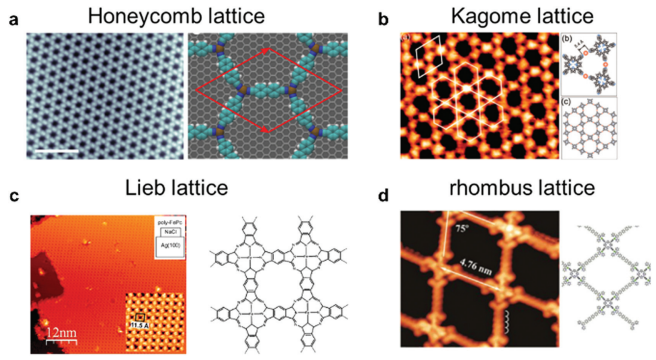

Fig. 30. Experimental synthesized MOFs in (a) honeycomb [239], (b) Kagome [240], (c) Lieb [241] and (d) rhombus lattices [242]. Reproduced with permission [239–242]. Copyright 2009, 2011, American Chemical Society; Copyright 2014, Royal Society of Chemistry; Copyright 2018, CC-BY 4.0.

In the following, we will focus on reviewing recent studies of 2D organic topological and quantum materials, in particular metal-organic frameworks (MOFs) featured with topological Dirac and flat bands, as well as intriguing topological quantum states they host, *e.g.*, quantum spin Hall and quantum anomalous Hall states.

4.1. Honeycomb lattices

The first organic TI (OTI) was theoretically predicted by Wang *et al.*, in the honeycomb lattice of $Bi_2(C_6H_4)_3$ and $Pb_2(C_6H_4)_3$ [244]. Theoretical calculations indicate that $Pb_2(C_6H_4)_3$ has a buckled honeycomb structure in which the *para*-Pb atoms are displaced alternately up and down out of the plane of the benzene rings (Fig. 31a). The honeycomb lattice gives rise to Dirac band. The band structure displays a gapless Dirac cone at the K point without SOC, but a gap of ~8.6 meV opens up when SOC is considered (Figs. 31b and c). The non-trivial topology is confirmed by non-zero topological invariant Z_2 number and edge states connecting the conduction and valence edge (Fig. 31d). The $Bi_2(C_6H_4)_3$ also has non-trivial topological properties and a Dirac-cone SOC gap as large as ~43 meV (Figs. 31e and f). However, its topological gap is 0.31 eV above the Fermi level because Bi has two extra electrons than Pb.

This original work aroused much attention and subsequently a number of theoretical OTIs by replacing the metal atoms with In [245], Mn [244], Tl [246] and so on [247]. For example, when Pb is replaced by magnetic Mn this family can exhibit a QAH effect (Fig. 32). The ground state of the $Mn_2(C_6H_4)_3$ lattice is found to be ferromagnetic with a magnetic moment of $4\,\mu_B$ per unit cell. The $Mn_2(C_6H_4)_3$ lattice is a half semimetal due to the spin-up (red dashed line) and spin-down (blue solid line) bands are completely split away from each other, and only the spin-down band is left around the Fermi level, as shown in Fig. 32a. $Mn_2(C_6H_4)_3$ lattice exhibits a gapless chiral edge state within the Dirac gap and is shown to have a nonzero Chern number (Figs. 32b and d). The physical origin of its quantum anomalous Hall effect (QAHE) due to both the intrinsic SOC and strong magnetization provided by Mn atoms.

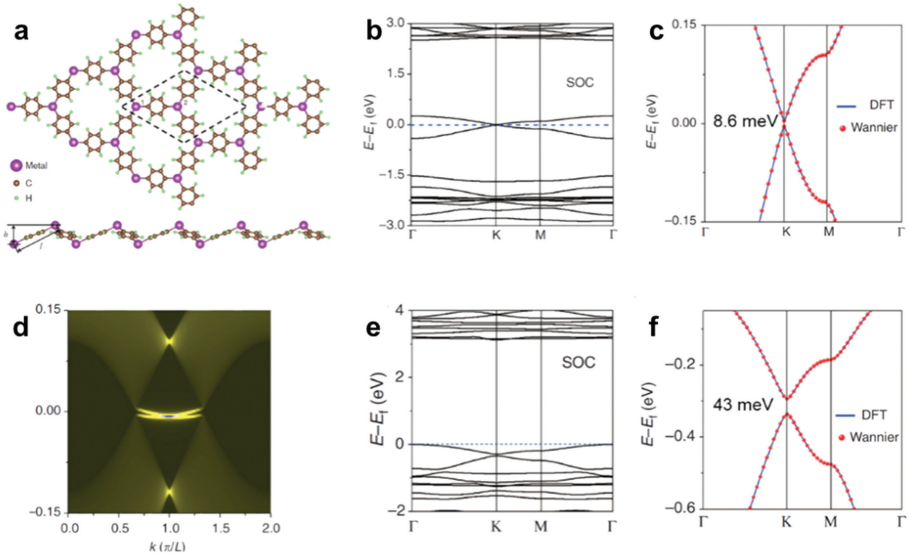

Fig. 31. Atomic structure and electronic properties of monolayer $Pb_2(C_6H_4)_3$ and $Bi_2(C_6H_4)_3$ in a honeycomb lattice. (a) Top and side views of the $Pb_2(C_6H_4)_3$ and $Bi_2(C_6H_4)_3$ lattice. Dashed lines show the unit cell. *l* and *h* are distance and height difference between the two metal atoms. (b, e) Band structures of $Pb_2(C_6H_4)_3$ and $Bi_2(C_6H_4)_3$ lattice with spin-orbit coupling (SOC). The dashed line indicates the Fermi level. The Γ, K, M and K' are the high symmetric k-points. (c, f) Zoom-in band structures of $Pb_2(C_6H_4)_3$ and $Bi_2(C_6H_4)_3$ lattice calculated by first-principles and Wannier functions around the Dirac-cone. (d) Energy and momentum-dependent local density of state (LDOS) of the zigzag edge of the semi-infinite lattice, *L* is the unit cell length along the edge. Copyright 2013, American Physical Society.

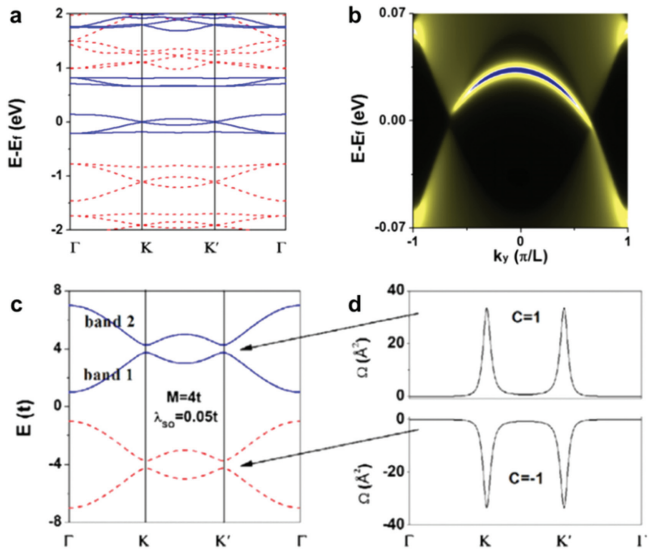

Fig. 32. Electronic and topological properties of monolayer $Mn_2(C_6H_4)_3$ in a honeycomb lattice [244]. (a) Band structure of $Mn_2(C_6H_4)_3$ lattice without SOC. Dashed red lines (solid blue lines) denote spin-up (spin-down) bands. (b) Semi-infinite edge states inside the Dirac gap of the $Mn_2(C_6H_4)_3$ lattice. (c) Tight-binding (TB) band structure with $M = 4t$ and $\lambda_{SO} = 0.05t$. (d) Berry curvatures by setting the Fermi level within the intrinsic SOC gap indicated by the arrows and the resulting Chern numbers. Reproduced with permission [244]. Copyright 2013, American Physical Society.

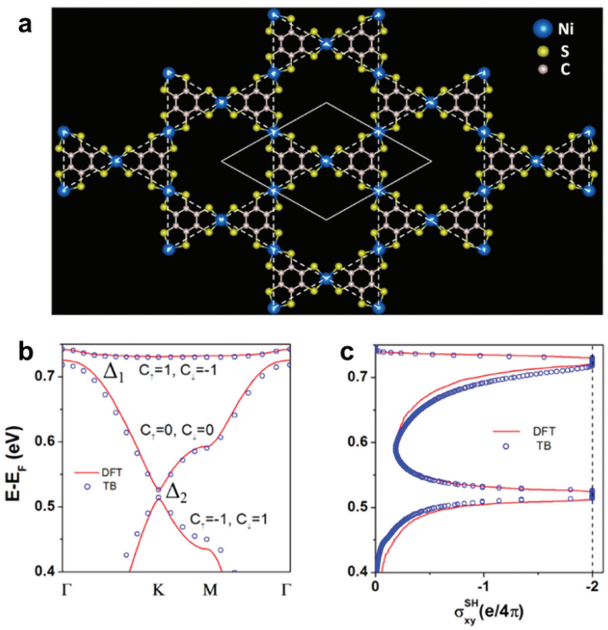

Fig. 33. Atomic structure and topological properties of $Ni_3C_{12}S_{12}$ Kagome lattice [248]. (a) Atomic structure of $Ni_3C_{12}S_{12}$ Kagome lattice. The solid lines show the unit cell, and the dashed lines outline the kagome lattice. (b) A comparison between first-principles and single-orbital TB band structures for the flat and Dirac bands. Calculated spin Chern number of each band is labeled. (c) Same as a for the quantized spin Hall conductance within the energy window of the two SOC gaps. Reproduced with permission [248]. Copyright 2013, American Chemical Society.

4.2. Kagome lattices

2D $Ni_3C_{12}S_{12}$ lattice is theoretically predicted to be a π-conjugated Kagome lattice, as shown in Fig. 33a [248]. The bands near Fermi level shows typical Kagome band feature (Fig. 33b): two Dirac bands near E_F with a gap of Δ_1 =13.6 meV, and a flat band lying above the upper Dirac band with a band gap of $\Delta_2 = 5.8$ meV. Both Δ_1 and Δ_2 vanish in the absence of SOC. To confirme the nontrivial topology of the $Ni_3C_{12}S_{12}$ lattice, the spin Chern number and spin Hall conductance are calculated, as marked in Figs. 33b and c. For both spins, the flat band and the bottom Dirac band have a nonzero Chern number (± 1), while the top Dirac band has a zero Chern number. Thus, within the SOC gap of Δ_1 or Δ_2, the spin Chern number is -1, and quantized spin Hall conductance ($(-2e/4\pi)$) both indicated that the $Ni_3C_{12}S_{12}$ lattice is topologically nontrivial. However, the topological gap (Δ_1 and Δ_2) is above Fermi level, thus $Ni_3C_{12}S_{12}$ lattice is not intrinsic. Electron doping is needed to move the Fermi level into the gap. It motivates the predictions of intrinsic 2D OTIs in Kagome lattices so that topological states can be measured directly without doping or gating.

Subsequently, a $Cu_2(DCA)_3$ Kagome lattice is predicted to be an intrinsic OTI [249]. As shown in Fig. 34a, 2D $Cu_2(DCA)_3$ lattice has a honeycomb lattice formed by the Cu atoms (red dash line), and a Kagome lattice by the DCA molecules (blue dash line). The lone pair in the CN group enables DCA molecule can easily form strong coordination bonds with Cu atoms. Recently, 2D $Cu_2(DCA)_3$ Kagome lattice has been successfully fabricated on Cu(111) (Fig. 34b) [250] and on $NbSe_2$ [251]. The adsorption configuration observed in experiment is well consistent with theoretically predicted $Cu_2(DCA)_3$ Kagome lattice in Fig. 34c. The $Cu_2(DCA)_3$ Kagome lattice exhibits a typical type of Kagome band around Fermi level (Fig. 34d). According to the PDOS, the Kagome bands mainly come from the p_z-orbital of the DCA molecule. Most importantly, a band gap ($\Delta_1 = 2.9$ meV) opens after SOC effect is considered and the Fermi level is exactly inside the SOC gap, indicating the feature of an intrinsic TI (Fig. 34e). The non-trivial topology is confirmed by nonzero Chen number and edges states connecting the bulk band edges (Fig. 34f).

Recently, Liu *et al.* proposed that a coloring-triangle (CT) lattice (Fig. 35a) can also host the Kagome band [252]. Soon after, 2D $Cu_2(DCB)_3$ CT lattice (Fig. 35b) has been predicted to be an OTI that host QAHE [253]. The $Cu_2(DCB)_3$ CT lattice has ferromagnetic (FM) ground state with a magnetic moment of 2 μ_B per unit cell. The spin-up (red line) and spin-down (black line) bands split, and the Fermi level is exactly between the flat band and top Dirac band (Fig. 35c). When the SOC is taken into account, band gap ($\Delta_1 = 2.0$ meV) opens between the flat band and the top Dirac band, and the Dirac point around -0.2 eV also opens a gap of $\Delta_2 = 0.6$ meV. However, the two SOC gaps are rather small. In order to increase the SOC gaps, Cu atoms are replaced by Au atoms. A global band gap is opened ($\Delta_1 = 10.9$ meV), due to larger SOC of Au than Cu. It separates the chiral edge states from the bulk states, which can be highly desirable in practical applications.

The thermal stability of the FM ordering of these local magnetic moments can be evaluated using Monte Carlo simulations within the Ising model, which exhibits a Curie temperature of about 100 K, as illustrated in Fig. 35d. Moreover, the nontrivial properties of the $Cu_2(DCB)_3$ CT lattice are confirmed by the calculated nonzero Chern number, the quantized Hall conductivity, and the gapless chiral edge states (Fig. 35e).

4.3. Lieb lattices

Different from D_{6h} symmetry protected honeycomb and Kagome lattices, the Lieb lattice having the D_{4h} group symmetry. The most representative Lieb lattice is metal-phthalocyanine (MPc) family, due to the organic ligand has 4-fold-coordination. Although MPc systems are widely studied [254–256], most experimental and theoretical studies didn't focus on their topological properties.

Recently, Jiang *et al.* investigated the electronic and topological properties of MPc materials of Lieb lattices [257]. The crystalline structure of MPc-MOF shows that the corner sites are occupied by the MPc ligand while the edge-center sites are occupied by the benzene ring, as illustrated in Fig. 36a. The band structure

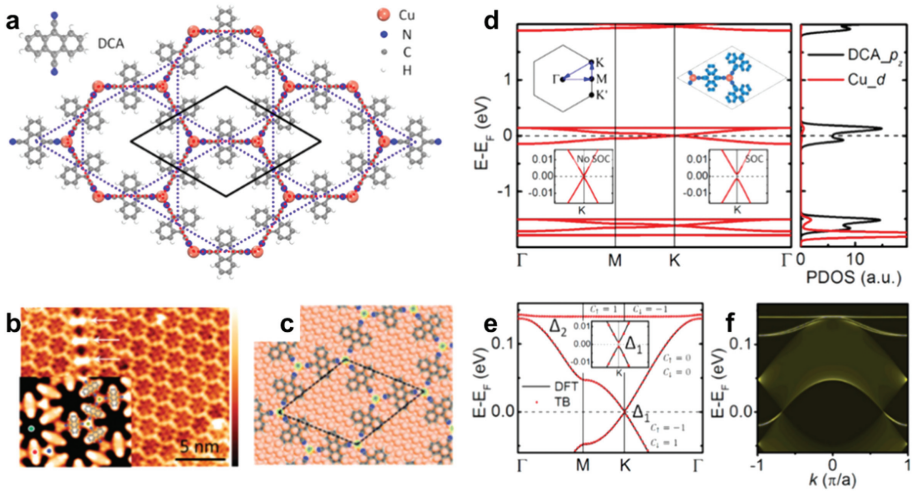

Fig. 34. The atomic structure and electronic properties of 2D $Cu_2(DCA)_3$ [249]. (a) A top view of the atomic structure. The red dashed, blue dashed, and black lines outline the honeycomb lattice of the Cu atoms, the Kagome lattice of the DCA molecules, and the unit cell, respectively. (b) STM image of self-assembled structure of DCA on Cu(111) after deposition at room temperature. Inset: high resolution STM image measured with a DCA modified tip [250]. (c) Proposed model of the adsorption configuration in (b). (d) Band structures and PDOS, where the top right inset indicates the charge distribution around the Fermi level, and the bottom two insets show the zoom-in bands without and with SOC, respectively. (e) Band structures around two SOC gaps (Δ_1 and Δ_2) calculated by the first-principles and single-orbital TB calculations. (f) The semi-infinite Dirac edge states within the SOC gaps. Reproduced with permission [249,250]. Copyright 2014, Royal Society of Chemistry; Copyright 2016, American Chemical Society.

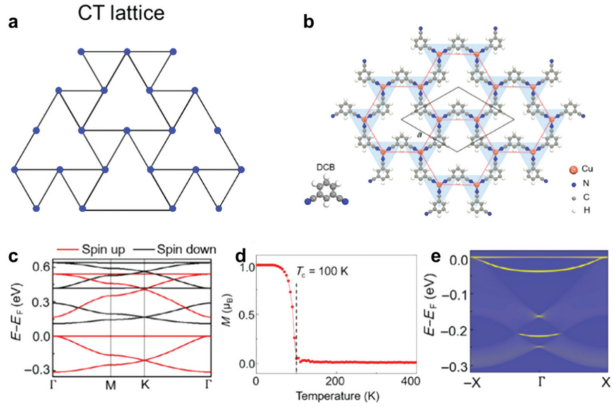

Fig. 35. The structure and electronic properties of 2D $Cu_2(DCB)_3$ CT lattice [253]. (a) Illustration of CT lattice model. (b) Atomic structure of $Cu_2(DCB)_3$ CT lattice. The red dashed line and black rhombus outline the honeycomb lattice of Cu atoms and the unit cell, respectively. The blue shadows represent the CT lattice of the DCB molecules (c) Band structure without SOC. (d) Temperature dependence of magnetic moment calculated by using Ising model. (e) The semi-infinite chiral edge states within the SOC gaps. Reproduced with permission [253]. Copyright 2020, Springer Nature.

of Zn-Pc is shown in Fig. 36b, which contains four bands around the Fermi level with a noticeable band gap (≈0.35 eV). The Fermi level locates right in the gap between the bottom Dirac band and the middle band.

The system is a topologically trivial insulator due to the on-site energy of the corner site, which is lower than that of the edge-center site. TB model analysis shows that a topological transition can be achieved by reversing the on-site energy difference between the corner and edge-center sites in the Lieb lattice, *i.e.*, increase the on-site energy of corner state and/or decrease the on-site energy of edge-center states. By applying biaxial strain, we can vary the on-site energy and achieve a topological phase transition (Figs. 36c and d).

4.4. Flat band in two-dimensional organic framework

A flat band (FB) presents a strongly interacting quantum system, has predicted in many two-dimensional (2D) lattice models and drawn increasing interest recently [258]. From the perspective of momentum space, the ideal flat band is nondispersive, and the electron kinetic energy is quenched, resulting in an infinite effective mass. Therefore, Coulomb interaction will play a dominant role, leading to a large number of exotic physical phenomena, such as quantum anomalous Hall effect [259], anomalous Landau levels [260], strongly correlated Chern insulators [261], Wigner crystallization [262], anomalous ferromagnetism [263]. FB features have been observed on the surfaces of transition metal compounds [264–266], twisted bilayer graphene [267], and the heterostructures [268], all of which contain one atomic layer manifesting a 2D FB lattice model, most typically the Kagome lattice. However, due to the elusive growth and synthesis of monolayer FB materials, experimental realization of topological FB has always been challenging, especially in the ideal form of monolayer materials originally proposed based on 2D lattice models.

4.4.1. Growth of mesoscale ordered 2D organic framework

2D organic frameworks, which include metal organic frameworks (MOFs) [245,248,269,270], covalent organic frameworks (COFs) [271–275], hydrogen-bond (H-bond) organic frameworks (HOFs) [276], *etc*. With the development of STM and qplus nc-AFM based on ultra-high vacuum technology, many organic reactions in solutions have been transplanted to the surface in recent years. Due to its unique reaction environment and ultra-high vacuum (UHV) conditions, surface synthesis has shown unprecedented advantages in preparing functionalized low dimensional nanostructures. Through the development of surface synthesis methods, researchers have successfully synthesized new carbon-based nanostructures represented by graphene nanoribbons and organic framework, which have enormous potential application value in electronic devices and other fields.

In ordered 2D structures synthesized on the surface, the self-assembly is a phenomenon in which monomers spontaneously recognize and assemble to form specific geometric structures under intermolecular interactions, including van der Waals forces, hydrogen bonds, and other non-covalent bond forces. The size of self-assembled structures can be in the order of micrometers or even millimeters. Lobo-Checa *et al.* prepared Cu-coordinated TPyB metal-organic network on Cu(111) surface (Figs. 37a-c) and studied the modification of the surface electrons by the inter-

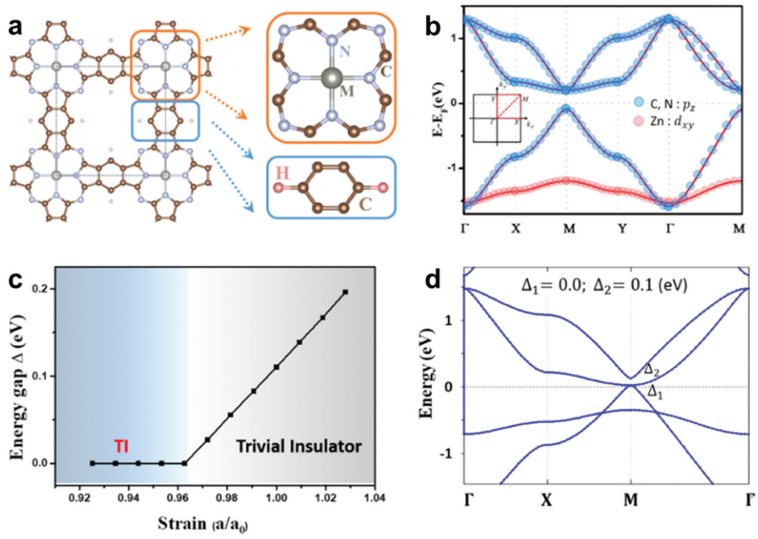

Fig. 36. The structure and electronic properties of 2D Zn-Pc Lieb lattice. (a) Crystal structure of MPc, where the corner and edge-center units are highlighted in the enlarged orange and blue rectangles, respectively. (b) Band structure of ZnPc Lieb lattice. The blue and red circles show the different orbital contribution to the bands around the Fermi level. (c) Topological phase transition as a function of biaxial strain. (d) Band structure of Zn-Pc under 6% compressive strain. Reproduced with permission [257]. Copyright 2020, American Chemical Society.

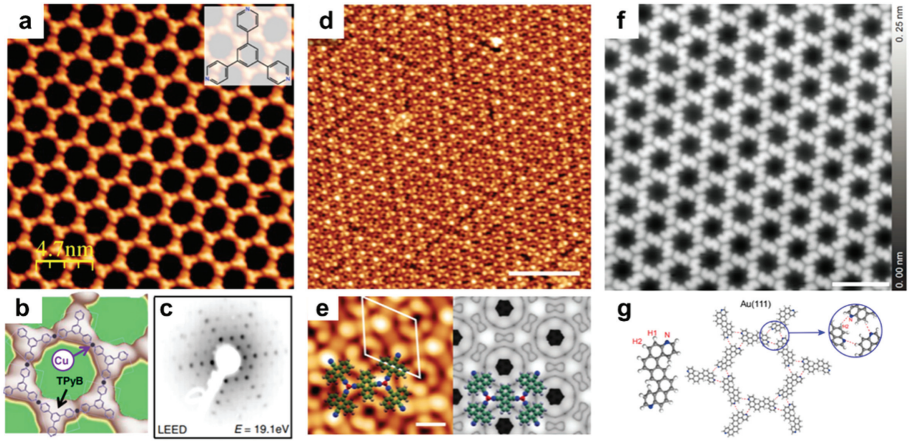

Fig. 37. Topographic characterization of ordered 2D Organic Framework. (a) High-resolution STM image of the single domain Cu-coordinated TPyB-Cu hexagonal QD array grown on Cu(111). The inset shows the precursor molecule. (b) Enlargement into the hexagonal porous structure with a superimposed structural model. (c) LEED pattern of TPyB-Cu network [277]. (d) STM overview image of a DCA_3Cu_2 MOF on G/Ir(111) surface. (e) High-resolution STM image and DFT-simulated STM image of DCA_3Cu_2 MOF [278]. (f) Hydrogen-bond network of 2N-S7 on Au(111). (g) Molecular models of 2N-S7 network on Au(111) [279]. Reproduced with permission [277–279]. Copyright 2019, American Physical Society; Copyright 2021, CC-BY 4.0; Copyright 2022, CC-BY 4.0.

action [277]. In 2021, Liljeroth *et al.* fabricated a 2D monolayer Cu-dicyanoanthracene MOF with long-range order on epitaxial graphene surface [278]. The ordered DCA_3Cu_2 network shows a structure combining a honeycomb lattice of Cu atoms with a Kagome lattice of DCA molecules and is predicted to be a 2D topological insulator (Figs. 37d and e). Yu *et al.* reported hydrogen-bonded molecular networks with tunable helical conformation on metal surfaces (Figs. 37f and g) [279]. Their results provide a distinctive access to molecular architecture with tunable helical conformation driven by H-bond interaction on surfaces.

4.4.2. Observation of flat bands using ARPES

As previously mentioned, flat bands, dispersionless in the whole Brillouin zone, have attracted extensive attention since it can be an ideal playground to study strong correlation physics [280]. Many 2D organic frameworks exhibit nontrivial topological states in both a Dirac band and a flat band [281]. In recent years, the band structure of organic systems has been characterized by ARPES [282,283], and this method has also been proved to be suitable for mesoscale 2D organic frameworks. Lobo-Checa *et al.* formed a long-range ordered mixed honeycomb-Kagome lattice on Cu(111) (Fig. 38a), which is predicted to be an organic topological insulator [284]. Kagome multi-band was experimentally determined through ARPES (Fig. 38b). Because of the interface interaction between substrate surface and 2D organic framework, it can be obviously observed from ARPES that FB inevitably overlaps with many dispersive bands from other atomic layers.

A recent experiment has successfully grown ordered 2D π-conjugated polymer Kagome lattices on Au(111), as shown in Fig. 38d, where Dirac bands can be clearly observed [153]. However, the FB, which was supposed to be presented with a Kagome sublattice, cannot be directly observed because it is located ~1.0 eV above Fermi level. In 2023, Pan *et al.* reported the growth of a self-assembled monolayer of 2D HOFs of 1,3,5-tris(4-hydroxyphenyl)benzene (THPB) on Au(111) [285]. High-resolution STM shows mesoscale, highly ordered, and uniform THPB-HOF domains (Fig. 38e), while ARPES highlights a FB over the whole Brillouin zone (Figs. 38f-h). More interesting, two dispersive bands

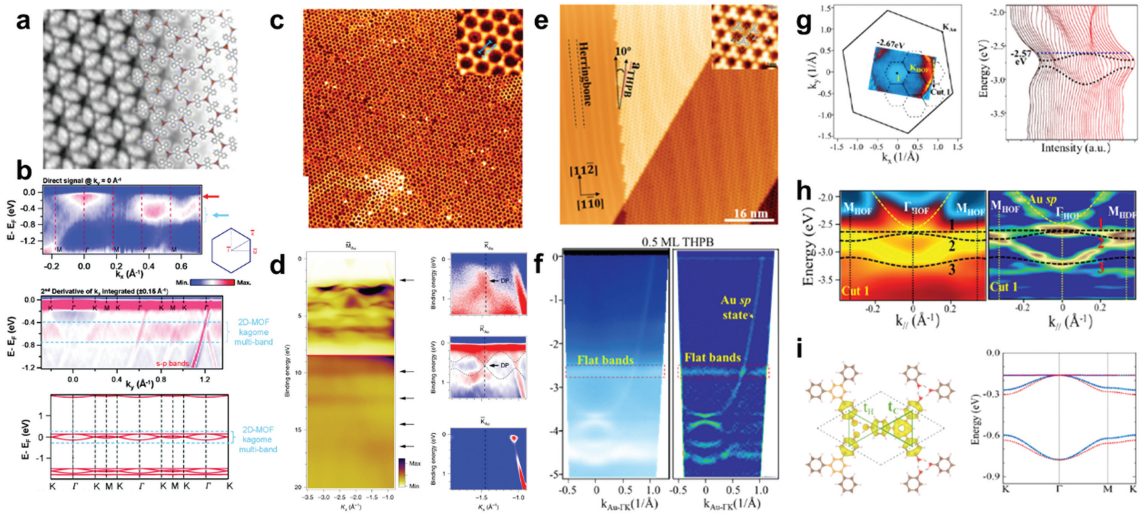

Fig. 38. 2D organic framework and its band structure. (a) STM image of DCA metal-organic network on Cu(111) surface. (b) Band structure of DCA-Cu network [284]. (c) STM image of P^{2}TANG on Au(111). (d) ARPES data for P^{2}TANG/Au(111) measured with photon energies of 30 eV [153]. (e) Large-scale topographic STM image of THPB/Au(111). (f) ARPES spectra and the second-derivative plot from a 0.5 ML THPB film. (g) Constant-energy contour and the energy distribution curves. The yellow dashed lines indicate the line cut taken for ARPES measurements in (h). (h) High-resolution ARPES and second-derivative plot [285]. (i) (left) The optimized lattice structure ovelaid with partial charge density derived from the top three valence bands belonging to the breathing-Kagome lattice formed by CBRs of THPB molecules. The brown/orange, red and pink balls represent C, O and H atoms, respectively. (Right) The fit of the top three valence DFT-LDA bands by the TB breathing-Kagome lattice model (red-dotted lines) and Wanner bases (cyan-dotted lines) [285]. Reproduced with permission [153,284,285]. Copyright 2020, Springer Nature; Copyright 2021, CC-BY-NC 4.0; Copyright 2023, American Physical Society.

appearing with the FB band, are separated with a gap at the K point instead of jointed, which indicates an effective "breathing" Kagome lattice. Further DFT calculation and d*I*/d*V* image show the THPB-HOF is a breathing-Kagome band structure with a highly degree of breathing of electronic hopping but without a breathing atomic structure, due to the intra-THBP corner benzene ring (CBR)-CBR hopping (t_C in Fig. 38i) *via* covalent bonds is much stronger than the inter-THBP CBR-CBR hopping (t_H in Fig. 38i) *via* H-bonds, even though the measured intra-THBP CBR-CBR distance ($d_C = 7.4$ Å) is about the same as the inter-THBP CBR-CBR distance ($d_H = 7.2$ Å). Additionally, this result also indicates that the advantage of H-bonds which are weaker but more flexible than the organometallic and covalent bonds, can be used to assemble large-scale monolayer structures with high uniformity. This finding demonstrates that self-assembly of HOFs provides a viable approach for synthesis of 2D organic topological materials, paving the way to explore many-body quantum states of topological FBs.

Beyond the quantum Hall effect that we have discussed, high-order topological phases have also been predicted in organic topological insulators. The OTIs have advantages of long spin coherence time and high tunability in structures, which may stimulate new physics if combining with nontrivial topological properties. It is worth to mention that Pan *et al.* observed topological flat band in hydrogen-bond organic framework [285]. Although some promising MOFs have been successfully synthesized in experiments. The evidence of topological characters, such as nontrivial topological edge states and quantized conductivity has yet not to be observed. In the future, efforts could be devoted to the growth of high-quality samples and measurement of topological properties. Going beyond, other intriguing quantum states related to electron-hole coupling such as superconductivity and charge density wave are remained to be explored.

5. Tip enhanced spectroscopy

STM not only can provide atomically resolved images of nanostructure in real space, but also is capable of manipulating single atoms or molecules at atomic scale, which make it a powerful tool for nanoscience research [286–292]. In order to further improve the chemical sensitivity of STM systems and enable the investigations on single-molecule optoelectronics, the STM system is combined with optical detections, which give birth to tip-enhanced spectroscopy techniques. Three types of tip-enhanced spectroscopy techniques are widely adopted, namely, STM induced luminescence (STML), tip-enhanced photoluminescence (TEPL) and tip-enhanced Raman scattering (TERS). In the following sections, we will focus on the experimental setup and theoretical background of these three techniques as well as associated typical scientific progresses. Note that, due to the limitation of article length, we will focus on the tip-enhanced spectroscopy techniques developed based on UHV and low-temperature (LT) STM systems, which can offer sub-nanometer or even atomic resolution of optical imaging.

5.1. Description on the experimental setup for optical detection

The guideline for the instrumental design of photon collection units in tip-enhanced spectroscopy techniques is to achieve a collection angle as large as possible and also to enable convenient operation on optical alignment. While the LT-UHV-STM system is an important platform for the investigation of single-molecule optoelectronics, the optical objective that is widely used in light collection in ambient conditions cannot be directly applied to a LT-UHV-STM system. This is because of two reasons: (1) There is no available commercial objective designed for both UHV and variable temperature (4∼420 K, *i.e.*, liquid helium temperature to system baking temperature) conditions; and (2) it is very challenging to place a commercial objective in the space-limited scanning stage and align the associated optical components inside a UHV chamber. In this way, how to design UHV-compatible light collection system is crucial for the realization of LT-UHV-STM system based tip-enhanced spectroscopy.

To overcome the above difficulties, as shown in Fig. 39, three types of setups are utilized to realize the light collection: parabolic mirror configuration, optical fiber configuration, and double-lens configuration [293–295]. For the parabolic mirror and the double-lens configurations, the light emission from the STM junction is

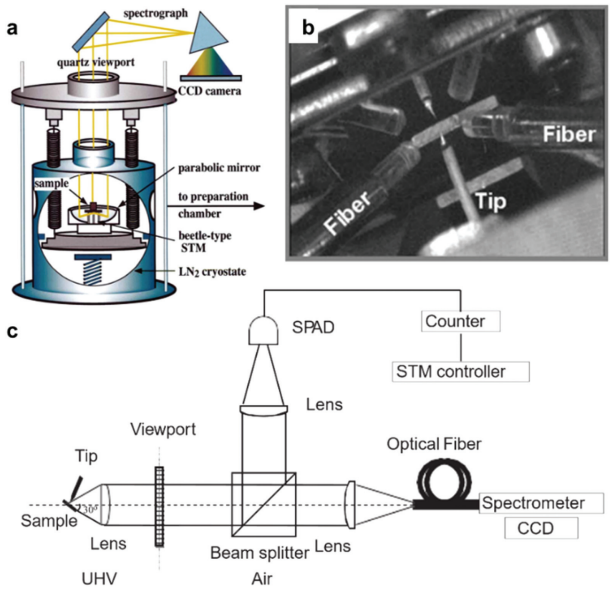

Fig. 39. Schematic of three types of photon collection setups. (a) Parabolic mirror configuration [293]. (b) Optical fiber configuration [294]. (c) Double-lens configuration [295]. Reproduced with permission [293–295]. Copyright 2001, Elsevier; Copyright 2007, 2013, AIP Publishing.

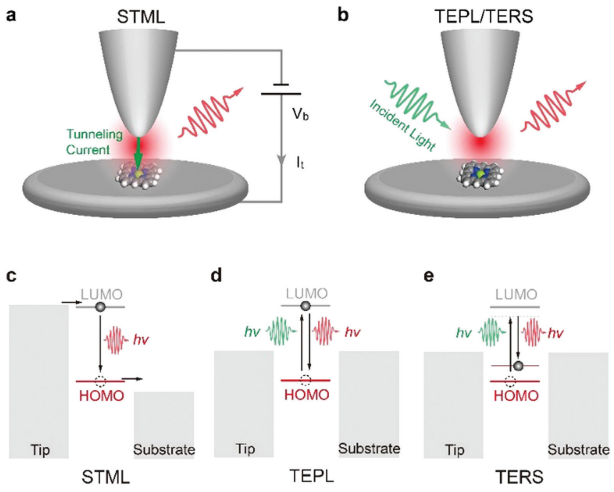

Fig. 40. Schematics for (a) STML and (b) TEPL/TERS techniques. Microscopic processes for the (c) STML, (d) TEPL, and (e) TERS.

first converted to parallel rays *via* the mirror or the lens, which can then pass through the UHV viewport to the optics outside the UHV chamber. For the fiber configuration, the light emission is directly collected *via* the optical fiber, which is then connected to the spectrometer outside the UHV chamber.

Researchers use the photon collection system with parabolic mirror configuration to investigate the plasmonic emission from metallic surfaces [296,297], metal clusters [293], as well as quantum dots on metal surfaces [298]. Such a geometry is advantageous in the absence of chromatic aberration as well as a large collected solid angle (with a resultant large collection efficiency, *e.g.*, ~60%) that is ideal to ensure efficient detection of photons. Nevertheless, the precise adjustment for an optimal focus is relatively difficult.

An alternative way to collect the photons emitted from the STM junction is feeding the light into optical fibers, which are positioned in close proximity to the junction. Such a configuration has been adopted to study the light emission spectra from semiconductor surfaces [299] and orbital symmetries of surface states [300]. Nevertheless, in this configuration, the collected solid angle is limited and the optimal positioning the fiber with respect to the STM tip is quite difficult.

Double-lens configuration can provide suitable hemisphere coverage of solid angles (*e.g.*, corresponding to a typical collection efficiency of 10%-20%) with the technical advantage of simple alignment [295,301,302]. Thus, such a configuration becomes a popular choose for the development of tip-enhanced spectroscopy in UHV conditions, which is widely used to investigate the optoelectronic properties of molecules[303] and two-dimensional materials [304].

The selection of photo detectors is also crucial for the efficient optical detection. As detailed in previous literatures [303,305], avalanche photo detectors (APDs) and charge-coupler devices (CCDs) are usually used in various modes of tip-enhanced spectroscopy measurements. An APD possesses single-photon sensitivity, a fast response in tens of picosecond and a high quantum efficiency in visible-light range, which is usually used in the measurements such as photon maps, excitation voltage sweeps, and photon correlation measurements. On the other hand, a CCD is an electronic sensor that converts light to digital signals and can act as a camera to record optical spectra in combination with a spectrograph.

5.2. Descriptions on the microscopic process

In this section, we will briefly introduce the microscopic processes for different tip-enhanced spectroscopy techniques.

STML, which marries STM with electroluminescence measurements, relies on a two-step excitation process. As shown in Fig. 40a and c, charge carriers are first injected from the metal electrodes to the sample, generating localized electronic excitations that subsequently undergo radiative recombination to produce luminescence. Therefore, the STML intensity is closely related to the quantum efficiency for the radiation process $\eta = \Gamma_{rad}/\Gamma_{tot}$, where Γ_{rad} and Γ_{tot} are the radiative rate and total decay rate, respectively [306]. To achieve intense electroluminescence in an STM junction, specific conditions must be satisfied: (1) the quantum emitters should be electronically decoupled from the metal substrate to avoid fluorescence quenching; (2) energy levels of the emitter should lie within the bias window spanned by the Fermi levels of the tip and substrate to allow carrier injection and subsequent exciton generation; and (3) carrier injection rates and lifetimes of molecular excited states should be balanced for efficient exciton generation. Since the lateral resolution of conventional STM can reach ~1 Å due to the quantum tunneling effect [307], the dye molecule is excited *via* highly localized tunneling electrons. The radiation process is significantly enhanced due to effective plasmon-exciton couplings under appropriate plasmonic resonance conditions. Note that, the dye molecule in STM junction is very close to the metal electrodes, which can introduce pronounced non-radiative energy dissipation and resultant fluorescence quenching (*i.e.*, causing η to approach zero). Nevertheless, thanks to the effective plasmon-exciton coupling, the strong plasmonic enhancement on the radiative process can surpass the non-radiative dissipation and “quench” the fluorescence quenching [308].

On the other hand, by illuminating the STM junction with laser beams, the optical response properties of the sample can be obtained using TEPL and TERS techniques. The incident light is confined in the nanocavity formed by the tip and substrate due to the plasmon resonance effect [309] and lightning-rode effect [310] generating a strongly enhanced and spatially confined local electromagnetic fields near the tip apex. The localized plasmonic field in STM junction is not only important for the enhancement of the weak signals from single emitters, but also crucial for achieving

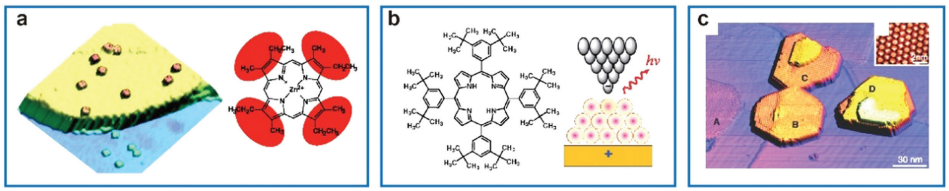

Fig. 41. (a) Electronic decoupling by a thin Al_2O_3 film on the NiAl(110) surface [316]. (b) Electronic decoupling by organic multilayer on metal surface [317]. (c) Electronic decoupling by a thin NaCl film on a metal surface [318]. Reproduced with permission [316–318]. Copyright 2003, American Association for the Advancement of Science; Copyright 2004, 2005, American Physical Society.

sub-molecular spatial resolution. Usually, the local field enhancement can be roughly estimated through the equation $|E_{loc}|/|E_{inc}| \approx (2R+d)/d$, where R is the radius of tip apex and d is the gap distance. The lateral spatial confinement of the can thus be approximated from $\sqrt{Rd}$, especially when $R>>d$. Therefore, by decreasing the tip radius (R) and the gap distance (d), an exceptionally localized electromagnetic field can be generated, pushing the resolution of TEPL and TERS to the Ångström scale. The plasmonic enhancement for the radiation process of the TEPL and TERS is reflected in the enhancement on the quantum efficiency (η) and the electric field ($|E_{Loc}|^2/|E_0|^2$). Therefore, the associated enhancement factors can be approximately expressed as $(|E_{Loc}|/|E_0|)^2 \times \eta$ for TEPL and $(|E_{Loc}|/|E_0|)^4$ for TERS, respectively. As a result, the optical signals from a single molecule, either it is excited by the electrons or photons, can be detected with high sensitivities owing to the dramatically enhanced and strongly confined local plasmonic field within the STM junction.

5.3. Scanning tunneling microscope induced luminescence

STML technique combines tunneling electron excitation with the local plasmonic enhancement of luminescence and offers a unique platform for the real-space investigation on the optoelectronic properties of nanostructures at nanoscale. One of the very original intentions of developing the STML technique is to achieve nanoscale electrically-driven photon sources [38,311], such as single-molecule photon sources.

In the beginning, lots of studies investigated the luminescence from molecules directly adsorbed on metallic surfaces. Nevertheless, these luminescence intensities were later found to be originated from plasmonic emission mediated by local density of molecular electronic states, rather than the intrinsic electronic transition from molecular electronic states [312–315], because the molecular emission is quenched due to the electron transfer between the molecule and the substrate.

In order to blocks the electron transfer between the chromophore and the substrate and realize the light emission from the intrinsic molecular electronic transition, two electronic decoupling strategies have been employed. The most widely used strategy is to physically introduce an insulating spacer between the molecule and metal substrate, *e.g.*, oxides [316], molecular multilayers [317], and halides [318], as shown in Fig. 41. In 2003, Qiu and co-workers first investigated electroluminescence from individual Zn(II)-etioporphyrin I molecules adsorbed on an ultrathin alumina film grown on a NiAl(110) surface and achieved the vibrationally resolved fluorescence from charged molecular states (Fig. 41a) [316]. In 2004, Dong and co-workers demonstrated the molecular fluorescence associated with intrinsic HOMO-LUMO transitions from multi-monolayer porphyrin molecules (Fig. 41b) [317]. In 2005, Cavar and co-workers showed electro-fluorescence and phosphorescence from fullerene molecular nanocrystals grown on ultrathin sodium chloride (NaCl) layers (Fig. 41c) [318].

The other strategy is to chemically modify the luminescent molecule by adding spacer groups to the chromophores [319,320]. As shown in Fig. 42a, such an electronic self-decoupling effect has been demonstrated by chemically adding tripodal anchors to the porphyrin chromophore [321]. The rigid tripodal anchor not only serves as a decoupling spacer but also controls the orientation of the chromophore molecule. Tetrapodal perylene molecules were later synthesized and studied, as shown in Fig. 42b, which can realize the self-decoupling effect regardless of the molecular adsorption configuration and can better align the transition dipole of the emitters along the vertical direction that would favor strong plasmonic enhancement [322]. On the other hand, molecular wires containing emitting chromophores were synthesized on surface and suspended between the STM tip and the substrate, as shown in Fig. 42c. The chromophores can be electronically decoupled from the substrate by progressively lifting the molecule wire, which can then produce molecule fluorescence with a narrow spectra linewidth down to ~2.5 meV [323].

Another key issue to realize the molecular electroluminescence in a STM junction is the energy matching between the nanocavity plasmon mode and the molecular intrinsic fluorescence. Since the size of the STM junction (*e.g.*, 1-2 nm) is much smaller than the light wavelength in visible range, nanocavity plasmons become the necessary "mediator" that can couple the molecular exciton to the far-field photons. Indeed, the presence of appreciable plasmonic fields inside the STM junction is found crucial for the generation of molecular fluorescence. In other word, by tuning the cavity plasmonic mode to be "bright" or "dark," defined by the photon emitting ability of the tip on a metal surface, the molecular electroluminescence in STM junction is found to be switched "on" or "off" correspondingly [324]. In addition, by spectrally tuning the frequency of plasmon modes and associated energy matching, not only can the molecular fluorescence band be selectively enhanced, but also the hot electroluminescence from highly excited vibronic states is generated [325]. Therefore, the efficient electronic decoupling and energy-matching plasmonic enhancement are the two key issues to achieve pronounced molecular electroluminescence with the STML technique.

STM induced electroluminescence from single molecules can help to explore optoelectronic phenomena occurring at the single-molecule level. In 2010, Chen and co-worker first demonstrate sub-molecular resolved electroluminescence imaging of a charged single magnesium porphine molecule [326]. The patterns in photon imaging are resolved as two orthogonal vibronic transitions, whose transition probabilities are dominated by the symmetry of the positions of the STM tip and the molecular transition dipole.

The ability of STML technique to resolve sub-molecular optical feature of a single molecule can help to study the intermolecular dipole−dipole interactions in real space. In 2016, Zhang and co-workers used sub-nanometer resolved fluorescence imaging to map the spatial distribution of different energy states due to the excitonic coupling [327]. The observed patterns for excitons of different states in a dimer indicate that the behavior of the coherent dipole-dipole coupling well resembles the σ and π orbitals in a molecule, as shown in Fig. 43a, revealing the local optical responses and their correlations with transition dipole orientations

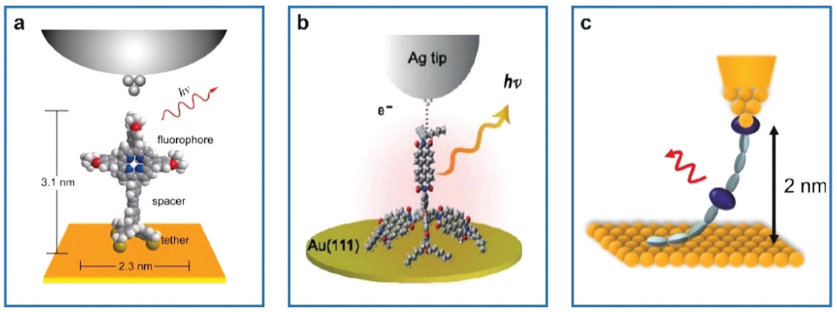

Fig. 42. (a) Schematic configuration of the porphyrin molecule with tripodal anchors [321]. (b) Schematic configuration of the tetrapodal perylene molecules [322]. (c) Schematic configuration of synthesized molecular wires containing chromophore molecule [323]. Reproduced with permission [321–323]. Copyright 2013, American Chemical Society; Copyright 2016, American Physical Society; Copyright 2019, AIP Publishing.

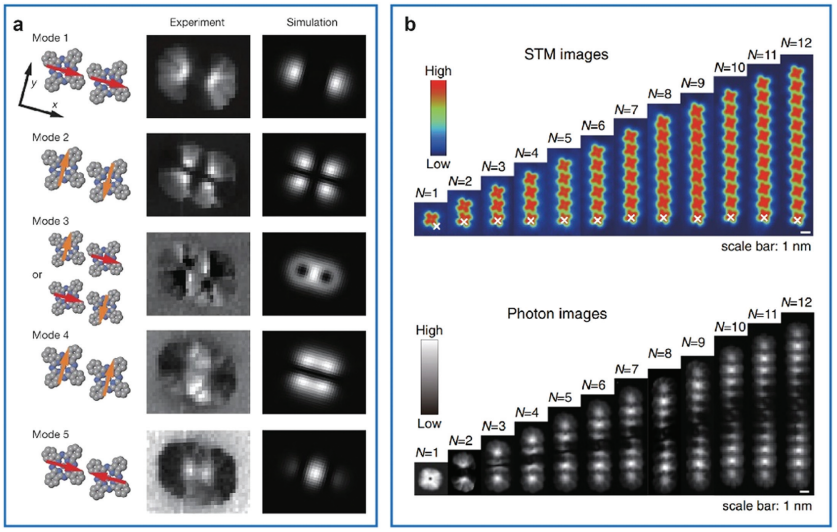

Fig. 43. (a) Visualizing coherent intermolecular dipole–dipole coupling in real space [327]. (b) Single-photon superradiance from constructed nonbonded phthalocyanine molecular chains [328]. Reproduced with permission [327,328]. Copyright 2016, Springer Nature; Copyright 2019, American Physical Society.

and phase relations. Furthermore, in 2019, Luo and co-workers investigated the emission behaviors of single-photon superradiant states from constructed nonbonded phthalocyanine molecular chains, as shown in Fig. 43b. Dumbbell-like patterns in sub-nanometer resolved fluorescence imaging directly reveal the coherent nature of the coupling associated with superradiant states and second-order photon correlation measurements demonstrate single-photon emission. The nanocavity plasmon is found to have a negligible effect on the intrinsic coherence established by the intermolecular dipole-dipole coupling, but it dramatically modifies the superradiance behavior, specifically on linewidth narrowing and intensity evolution [328].

STML technique is also used in the real-space investigation on intermolecular energy transfer at single-molecule level. In 2016, Imada and co-workers demonstrated the energy transfer in heterogeneous molecular dimers in real space [329], as shown in Fig. 44a. A reciprocating resonance energy transfer is observed when exciting the highly-lying electronic state of the acceptor molecule, which results in backward energy transfer to the first excited electronic state of the donor and final funnelling to the first excited electronic state of the acceptor. In 2021, Cao and co-workers explored the energy funnelling behaviors within donor−intermediate−acceptor multichromophoric architectures assembled on a surface. The role of intermediate molecules was studied in promoting, blocking or directing resonant energy transfer processes [330], as shown in Fig. 44b. In 2022, Kong and co-workers demonstrated incoherent-to-coherent transition in the energy transfer process in real space by constructing well-defined donor–acceptor model systems with controlled separations [331], as shown in Fig. 44c. Spatially resolved fluorescence imaging helps to reveal the occurrence of wavelike quantum-coherent energy transfer, which is found to be dipole-orientation dependent. Furthermore, the coherent energy transfer is about 3 times more efficient than the incoherent transfer in a one-step transfer process, highlighting its advantage in the transfer process in large molecular networks.

5.4. Tip-enhanced photoluminescence

The push for higher spatial resolution has always been one of the main driving goals for the development of near-field optical microscopy ever since its birth. The first target is to overcome the diffraction limit in far-field microscopy. Due to wave nature of light, best achievable spatial resolution in far-field optical microscope is about $\lambda/2$ (λ is the wavelength of light) because of diffraction. In 1928, E. H. Synge proposed an idea of using a small subwavelength aperture to scan over a sample placed in close proximity for nano-imaging [332], although it is not technically possible at that time. The advent of STM in the early 1980s provides the necessary micro-positioning technology for Synge's original idea, which facilitates the invention of the scanning near-field optical microscope (SNOM) later. In 1984, both Pohl *et al.* from IBM and Lewis *et al.* from Cornell University separately developed metal-coated tapered fiber probes with a small hole at the apex of the probe and invented the aperture SNOM [333,334], which enables the spatial resolution of about 20−50 nm that is far beyond the

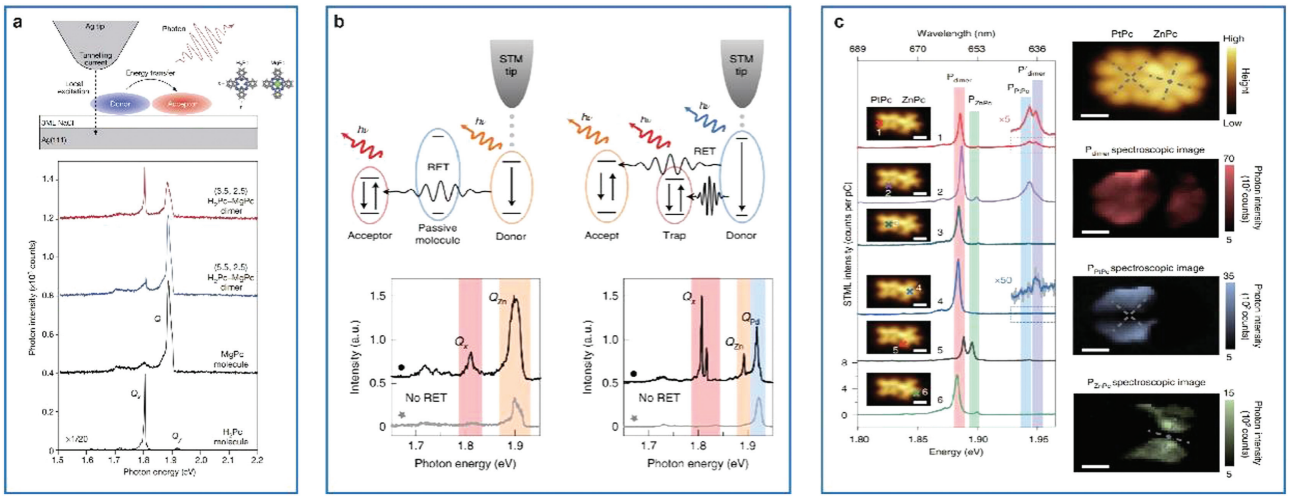

Fig. 44. Typical advances in the STML studies on intermolecular energy transfer and interactions. (a) Resonance energy transfer in heterogeneous molecular dimers [329]. (b) Energy funneling within constructed multichromophore architectures [330]. (c) Dipole-orientation-dependent quantum-coherent energy transfer in a constructed phthalocyanine heterodimer [331]. Reproduced with permission [329–331]. Copyright 2016, 2021, 2022, Springer Nature.

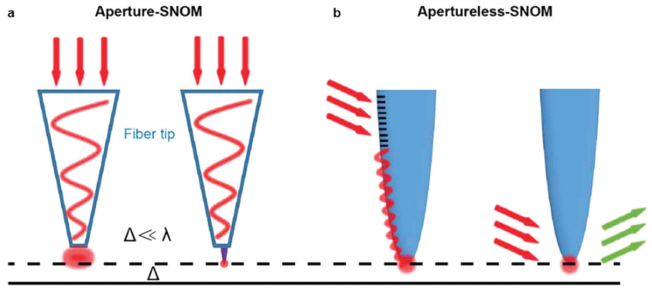

Fig. 45. Illustration of different types of aperture SNOM and scattering SNOM devices. (a) Aperture SNOM. (b) Scattering SNOM. Reproduced with permission [335]. Copyright 2019, CC-BY 4.0.

diffraction limit in visible light range. Since then, the field of near-field optics started to flourish. In 1993, Betzig and Chichester optimized the aperture SNOM system, improved the sensitivity to single-molecule level, and achieved the detection of the orientation of each molecular dipole [37]. Note that, parallel to the development of aperture SNOM, another type of SNOM, apertureless SNOM, also gradually becomes popular, in which a sharp and apertureless probe is used as either a scattering center or a light source [335], as shown in Fig. 45.

The spatial resolution achieved with aperture SNOM is generally limited by the dimensions of the aperture employed, while the spatial resolution with the apertureless SNOM is usually determined by the curvature radius of the tip apex. To pursuit for even higher spatial resolution, researchers further modify the tip with plasmonic nanostructures and combine the SNOM with the localized surface plasmons, which can evidently compress the mode volume of light and extract local optical responses.

In 2004, Frey and co-workers used a “tip-on-aperture” SNOM probe, consisting of a sharp Aluminum tip mounted on a conventional fiber probe, to collect the fluorescence from dyes bound to the end of DNA [336], as shown in Fig. 46a. The spatial resolution is about 10 nm and the orientation of dyes can be distinguished. In 2006, Anger and co-workers attached a gold nanoparticle with a diameter of ~80 nm to the end of a pointed optical fiber probe, and presented the theoretical and experimental studies on the fluorescence enhancement and quenching of a single molecule as a function of the distance to the laser-irradiated gold nanoparticle [337], as shown in Fig. 46b. By varying the distance between molecule and gold particle, the authors demonstrated the continuous evolution from fluorescence enhancement to fluorescence quenching. With the distance decreases, the enhanced local field leads to the excitation enhancement whereas the boosted nonradiative energy transfer to the gold particle results in the decrease of the quantum yield and associated fluorescence quenching. The maximum fluorescence enhancement is obtained at a molecule−particle distance of ~5 nm, yielding a corresponding spatial resolution of ~65 nm. In the same year, Kuhn and coworkers fabricated a uncoated heat-pulled fiber tip attached by a single gold nanoparticle (diameter 100 nm) and studied the coupling between a single molecule and a single gold nanoparticle [338], as shown in Fig. 46c. The molecular fluorescence intensity is enhanced by ~20 times and the excited state lifetime is simultaneously shorten by 20-fold. The spatial resolution of the near-field image is about 65 nm, which is evidently improved, compared with the typical confocal fluorescence image. In 2012, Hoppener and co-workers fabricated gold nanoparticle dimer or trimer antenna structures on fiber tips and demonstrated the cascading enhancement effect of local fields [339]. The authors first used a self-similar dimer antenna consisting of 80 and 40 nm gold nanoparticles and achieved a fluorescence enhancement of ~20 times and a near-field spatial resolution of ~25 nm. When changing to a trimer antenna consisting of 80, 40, and 20 nm gold nanoparticles, the fluorescence enhancement reached up to ~40 times and the spatial resolution is improved to 15 nm.

Despite of these above progresses, the lateral resolution for photoluminescence from typical plasmonic cavities reported was still around 10 nm. The further improvement in spatial resolution is limited by the competition between the field enhancement and the fluorescence quenching when the plasmonic structure is positioned in close proximity to the emitter. In 2020, Yang and co-workers overcome the above difficulty and demonstrated sub-nanometer-resolved single-molecule near-field photoluminescence imaging [308], as shown in Fig. 47. Three key elements have been identified to contribute to this achievement: (1) the tip should be plasmon-active with its tip apex featuring an atomistic protrusion, (2) the single molecule should be electronically decoupled from a plasmonic substrate through a dielectric spacer of atomic-scale thickness, and (3) the junction geometry should be precisely controlled in three dimensions with sub-nanometer precision. All these aspects allow to generate a strong and highly confined NCP field for the massive excitation and emission enhancement. With such junction design and control, the molecular fluorescence is

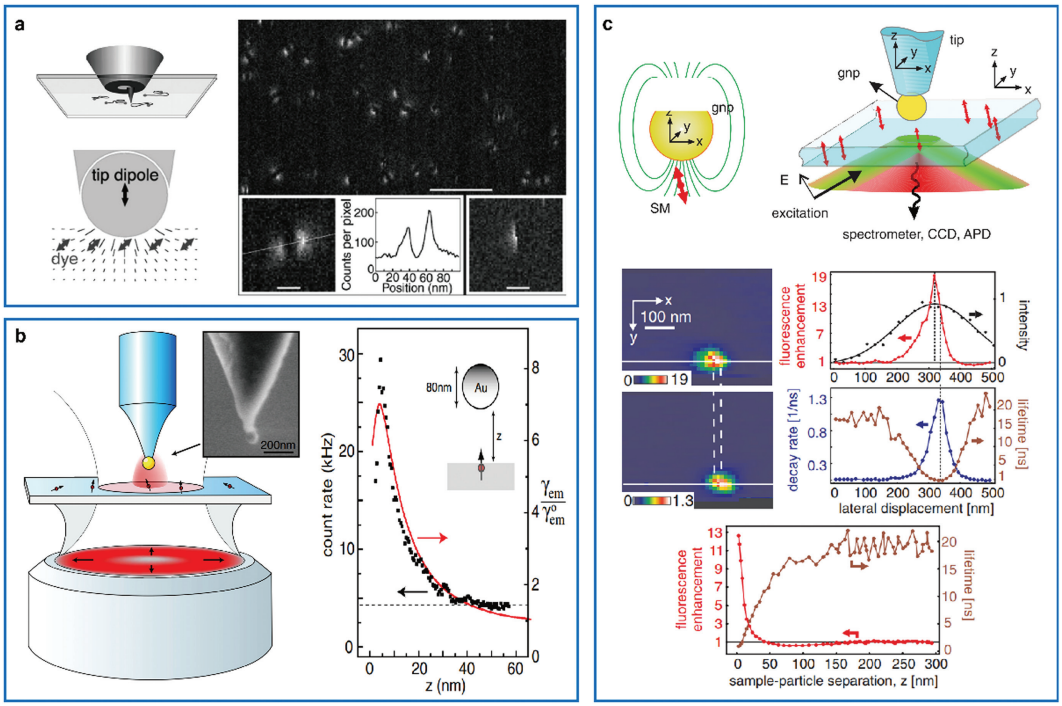

Fig. 46. (a) Near-field study on dye molecules with a "tip-on-aperture" probe [336]. (b) Enhancement and quenching of single-molecule fluorescence investigated *via* a fiber tip attached with a gold nanoparticle [337]. (c) Investigation on enhancement of single-molecule fluorescence using a gold nanoparticle as an optical nanoantenna [338]. Reproduced with permission [336–338]. Copyright 2004, 2006, American Physical Society.

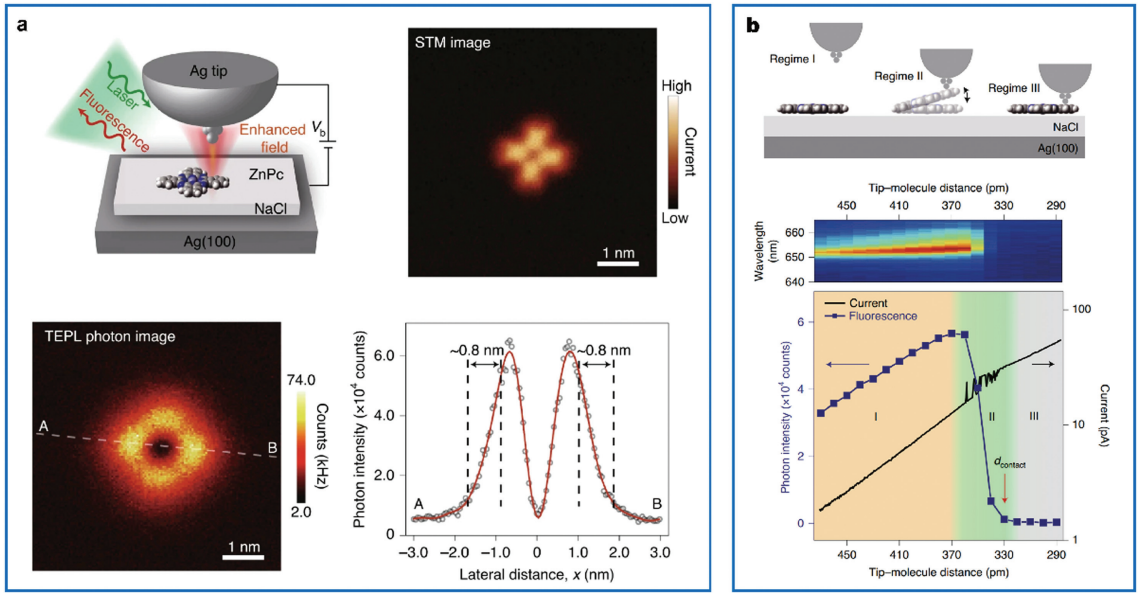

Fig. 47. (a) Sub-nanometer resolution in tip-enhanced photoluminescence imaging. (b) Revealing the photophysics of molecular photoluminescence in a plasmonic nanocavity by tracking the evolution of TEPL intensities at different tip–molecule distances. Reproduced with permission [308]. Copyright 2020, Springer Nature.

found to exhibit a monotonically enhancing behavior, rather than becoming quenched, as the tip approaches the molecule to the point of contact. The spatially and spectrally resolved spectroscopic imaging with sub-nanometer resolution can provide quantitative information about the interactions and mechanisms in coupled plasmon−molecule systems beyond the single-molecule level.

5.5. Tip-enhanced Raman spectroscopy

Tip-enhanced Raman spectroscopy (TERS) is a powerful spectroscopic microscopy technique that combines SPM with Raman spectroscopy [340–344]. This technique primarily exploits the localized field enhancement at the metal tip or in the plasmonic nanocavities to detect Raman scattering signals from the local chemical groups of the molecules. Comparing with the Raman signal of single molecules obtained with conventional far-field measurement, the enhancement factor obtained with TERS technique can generally reach as high as $\sim 10^6$-10^{12} [345]. The enhancement mechanisms of TERS can be categorized into two kinds: the physical enhancement and the chemical enhancement. The physical enhancement effect results from the local electromagnetic field enhancement due to the surface plasmonic resonance, and the enhance-

ment of TERS signal is proportional to the fourth power of the local field enhancement [306,346,347], reaching about 10^6-10^8. The chemical enhancement effect is caused by the interactions between the molecule and the metal surface, which involves three kinds of microscopic processes [348]: the redistribution of electron cloud of the molecule when it is adsorbed on the metal surface [349], the formation of molecule-metal complex through the strong chemical interaction between the molecule and the substrate [350], and the photo-induced charge transfer process when the excitation light energy is close to the energy difference between the LUMO (or HOMO) orbitals of the molecule and the Fermi level of the metal [351]. All these three processes can significantly change the polarizability of the molecules and result in the chemical enhancement with the magnitude generally in the order of 10-100.

In 2000, four different research groups, Zenobi [352], Anderson [353], Kawata [354], and Pettinger [355], independently developed the TERS technique, opening up a new era of spectro-microscopy technology for the exploration of nanoscale materials and structures. In 2003, the Novotny group first achieved the TERS imaging of a single-walled carbon nanotube for the G' band vibrational mode under ambient conditions. The TERS experiments showed a spatial resolution of 25 nm, which exceeded the resolution of simultaneously collected AFM images [356]. In 2008, the Pettinger group developed a TERS system under UHV conditions and obtained the TERS imaging of a single BCB dye molecule adsorbed on Au substrate with a resolution of 15 nm [357]. In 2009, the Kawata group used an AFM tip to apply controlled pressures to carbon nanotubes and adenine nanocrystals, and achieved a spatial resolution of 4 nm by analyzing the spectral shifts of characteristic Raman peaks [358].

The spatial resolution of TERS imaging relies on the confinement of the plasmonic field, which is very sensitive to the stability of the STM system. In 2013, Dong group further developed a TERS system that is based on a UHV-LT-STM system, which significantly improves the stability of the junction and the control over of tip−molecule distances. They demonstrated a subnanometer resolution (0.5 nm) of TERS imaging over a single porphyrin molecule for the first time [40], as shown in Fig. 48a. With such a high spatial resolution of the developed TERS technology, they can achieve the chemical identification of adjacent different porphyrin molecules adsorbed on the surface, and even distinguish the adsorption configurations of the adsorbed molecules [359], as shown in Fig. 48b. In 2016, Van Duyne group used TERS spectra to investigate two distinct adsorption configurations of porphyrin molecules on a Cu(111) surface under room temperature and UHV conditions. As shown in Fig. 48c, the spatial resolution of ~0.26 nm was achieved through the line scanning analysis of characteristic vibrational modes [360]. In 2019, Jiang group also developed single-molecule TERS techniques based on UHV-LT-STM system and investigated different adsorption configurations of rhodamine molecules on an Ag(100) surface, achieving a spatial resolution of 0.5 nm [361], as shown in Fig. 48d.

The spatial resolution of TERS can be further improved to single-chemical-bond level. In 2019, two different research groups (Apkarrian group [362] and Dong group [363]) independently developed the Ångström-resolved TERS technique based on UHV-LT-STM systems operated at the liquid-helium temperatures (below 10 K). As shown in Fig. 49a, Apkarian group demonstrated the TERS imaging of a single CoTPP molecule on the Cu(111) surface with a spatial resolution of 1.67 Å, showing different features in spatial distributions for different vibrational modes. As shown in Fig. 49b, Dong group demonstrated the full TERS imaging of different vibrational modes for a single porphine molecule adsorbed on the Ag(100) surface with a spatial resolution of 1.5 Å. Furthermore, they proposed a new methodology for the determination of single molecular chemical structures, named as Scanning Raman Picoscopy (SRP), through a Lego-like building process from the TERS images [363]. It is important to note that, such a single-bond resolution of TERS can be not only showcased for planar molecules lying flat on surfaces, but also applicable for the upstanding molecules. As shown in Fig. 49c, through the analysis of the TERS spectra of individual melamine molecules vertically adsorbed on a Cu(100) surface, one can not only specify two N–H bonds at the top and other two N–H bonds at the bottom becoming dehydrogenated upon chemisorption on Cu(100), but can also track the breaking of one top N–H bond and the formation of a new N–H bond on the cyanuric ring, resulting in the tautomerization process through photon-induced hydrogen transfer [364]. In 2022, Dong group further applied the TERS technique to a vertically adsorbed single carbon monoxide (CO) on the Cu(100) substrate and investigated the tip-induced bond weakening, tilting and hopping of the single CO molecule on surface [365], as shown in Fig. 49d.

By combining the Ångström-resolved TERS with STM and nc-AFM, the structure and chemical heterogeneities of surface species can be further in-situ identified, enabling to directly monitor single-bond breaking and making processes inside a molecule under the nanocavity plasmon field. As shown in Figs. 50a and b, the joint STM-AFM-TERS strategy provides a comprehensive characterization of electronic states, skeleton structures and chemical vibrations, giving an univocal determination of the heterogeneities of molecules at the single-bond limit [366]. The intact pentacene (α) on the Ag(110) surface undergoes sequential transformations into two new species (β and γ) under plasmon fields. The AFM image in Fig. 50c shows that the pentacene-α has two protrusions at the central benzene ring, while the pentacene-β and pentacene-γ lose one and two protrusions, respectively. Such changes imply the two C-H bonds at the central benzene ring have broken sequentially. Optimized geometries of three pentacene species are shown in Fig. 50e. Direct evidence for C-H bond breaking should come from the changes of C-H vibrational modes. Fig. 50d records the real-space changes of the C-H stretching mode at 2800-2900 cm^{-1}, which shows two spots for pentacene-α. The absence of one and both spots for pentacene-β and pentacene-γ confirms the C-H bond breaking at the central benzene ring. In particular, it is found the C-H bond breaking under plasmon field takes place quickly within ~10 s. To capture such rapid changes, a high-speed TERS method was developed by using a highly-sensitive avalanche photodiode (APD) to collect the Raman photons, as shown in Fig. 50b. This method with APD has the potential to capture nanosecond dynamics by recording the change of the Raman photons. Furthermore, the joint STM-AFM-TERS strategy can be used to determine the intramolecular isotope effects [367]. As shown in Fig. 50f, by comparing the TERS spectra and maps of pentacene-H and its fully deuterated form pentacene-D, it can reveal that the isotopic effects not only changes the frequencies of intrinsic vibration modes but also alters the spatial distribution of various vibration modes in real-space.

Moreover, the Ångström-resolved TERS has also been widely used for local chemical identification of electrochemical and 2D-material studies. For example, Ren's group reported a series of studies on site-specific catalytic properties of bimetallic systems [368–370]. Recently, Jiang's group revealed that the bilayer borophene shows high oxidation resistance in contrast to highly reactive borophene monolayers, as shown in Figs. 51a and b [371]. Wu's group analyzed the vibrational characteristics of various silicene phases, as well as defects and domain boundaries, to gain a comprehensive understanding of their structural properties [372]. Jorio's group performed TERS spectroscopic imaging on the superlattice in reconstructed twisted bilayer graphene and identified strain solitons as well as topological points with the nuanced im-

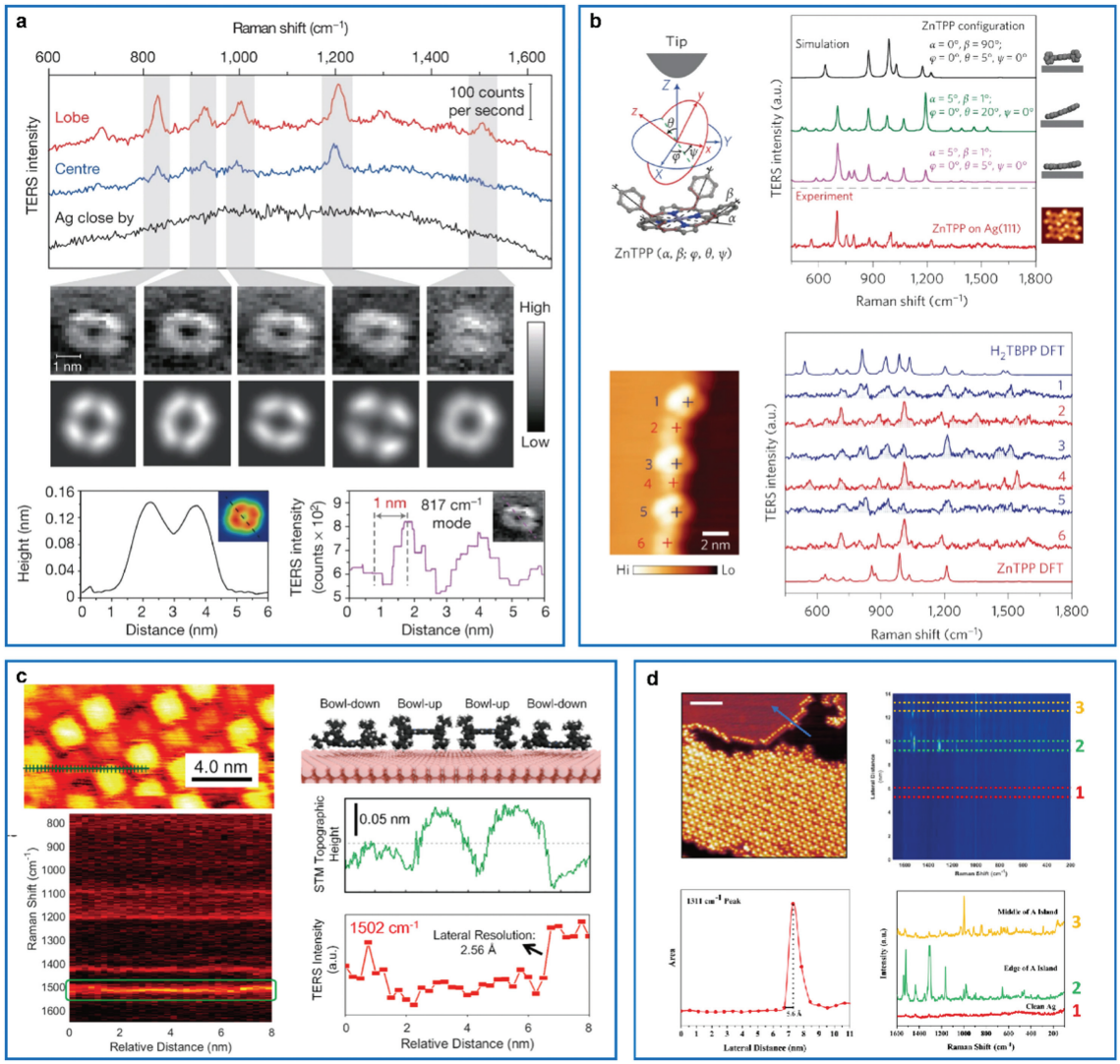

Fig. 48. (a) Sub-nanometer resolved TERS imaging for different vibrational modes of a porphyrin molecule on Ag(111) [40]. (b) TERS spectra acquired at different adjacent molecules at the step edge and their comparison with corresponding simulated spectra [359]. (c) TERS line scanning analysis of intensity variations in specific vibrational modes for porphyrin molecules with different adsorption configurations [360]. (d) Multiple configurations of rhodamine molecules on Ag(100) surface and corresponding TERS measurements [361]. Reproduced with permission [40,359–361]. Copyright 2013, 2015, Springer Nature; Copyright 2016, 2020, American Chemical Society.

pact of electron-phonon coupling on Raman intensity and peak line width (Figs. 51c–f)) [373].

Therefore, tip-enhanced spectroscopy technique stands as a formidable and versatile technique, enabling in-depth exploration of optoelectronic properties and chemical structures of diverse systems at the atomic scale. Its remarkable ability to uncover minute details makes it potential to study intricate surface interactions, design novel materials and explore complex biological systems at the atomic level. However, there still remain challenges for tip-enhanced spectroscopy technique to become a routine analytical technique, such as the tip stability, numerical aperture of the illumination and collection optics, detection efficiency, Raman scattering cross section and unavoidable far-field background in crystalline materials, which requires more advanced experimental setups and techniques to be overcome [374].

6. Applying machine learning in studying surface-supported molecules and nanostructures

As a subset of surface chemistry, on-surface molecular reaction and assembly remain labor intensive and often require tedious work to optimize the synthetic route and to analysis the data. Traditional protocols of data acquisition and analysis heavily rely on human inspection and inevitably suffer from subjectivity and ambiguity. Machine learning (ML) technologies have recently become one of the most exciting and promising tools in materials science. In contrast to the traditional research paradigms, ML approaches excel at extracting important features, patterns or trends from the data, and understanding the underlying relationship for predictions and data generations [375–377]. The ML approaches can make decisions for experimental planning and even automated experiments [378–380]. Dirven by the exponential growth of computing power and the rising existing data both from experiments and computations, ML models can be trained more efficiently but less time-consuming, leading to significant progress in important subcategories including computer vision, deep learning and natural language processing.

ML methods have the potential to revolutionize chemical researches because of its capability to process complex tasks and make precise predictions. We have already witnessed a surge of interest and investments from different fields of chemical researches. There are a few recent reviews providing overview of the emerg-

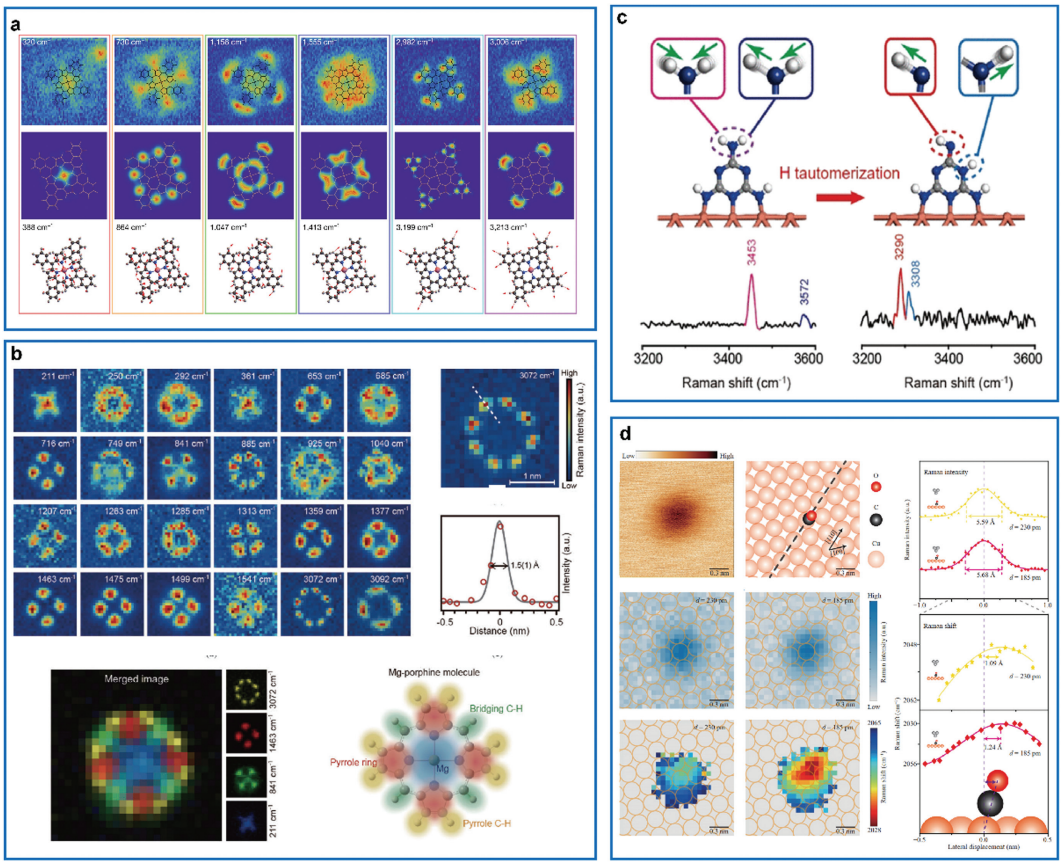

Fig. 49. (a) Ångström-resolved TERS imaging of different vibrational normal modes for CoTPP on Cu(111). Reproduced with permission [362]. (b) Reconstructing the chemical structure of a single molecule by scanning Raman picoscopy [363]. (c) Raman detection of bond breaking and making of a chemisorbed up-standing single molecule at single-bond level [364]. (d) Tip-induced bond tilting of a single CO molecule on Cu(100) [365]. Reproduced with permission [362–365]. Copyright 2019, Springer Nature; Copyright 2019, CC-BY 4.0; Copyright 2021, American Chemical Society; Copyright 2022, CC-BY 4.0.

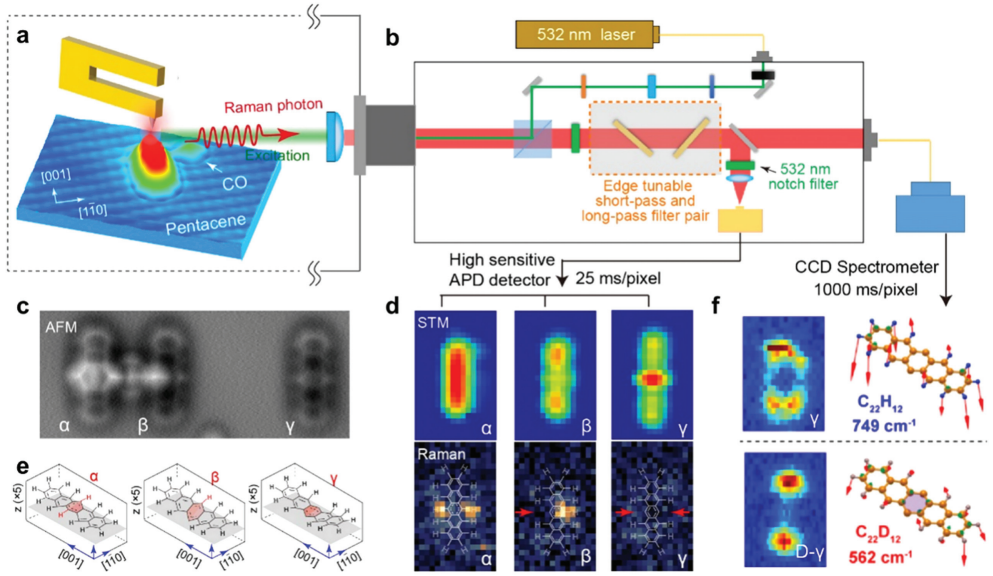

Fig. 50. Characterizing chemical reactions within a molecule at the single-bond limit. (a) Schematic diagram of characterizing pentacene species on the Ag(110) surface with the joint STM-AFM-TERS method. (b) TERS optical setup diagram. (c) AFM images, (d) STM images and the simultaneously acquired Raman images for the C–H stretching vibration recorded by APD, (e) Optimized geometries of three pentacene species [366]. (f) TERS imaging and calculated atomic vibrations of the corresponding vibrational mode of γ and D-γ, respectively [367]. Reproduced with permission [366,367]. Copyright 2021, American Association for the Advancement of Science; Copyright 2023, American Chemical Society.

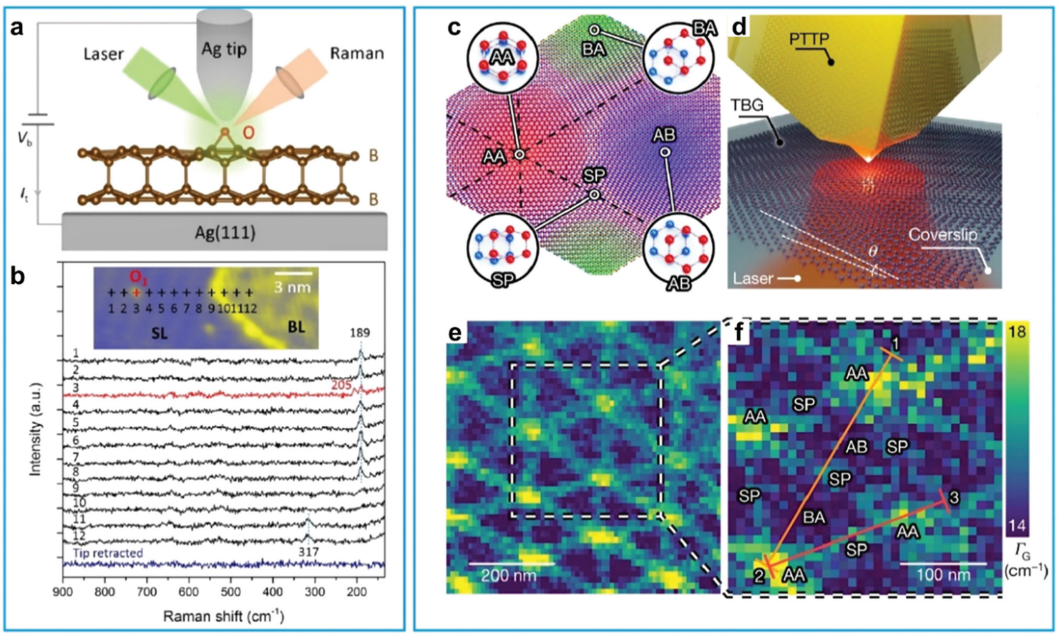

Fig. 51. (a) Schematic diagram of TERS characterizing bilayer (BL) two-dimensional boron on the Ag(111) surface. (b) Line-track TERS measurements along the dashed line in the inset STM image across an oxygen adatom on single-layer (SL) borophene [371]. (c) Schematics of the superlattice in reconstructed twisted bilayer graphene, including neighboring AB- and BA-stacked domains, strain solitons (SP) and topological points (AA). (d) Schematics of TERS measurements. (e) TERS intensity mapping of the G'-band mode. (f) TERS linewidth mapping of the G-band for the close-up of the boxed region in (e) [373]. Reproduced with permission [371,373]. Copyright 2021, Springer Nature; Copyright 2023, CC-BY 4.0.

ing opportunities at the intersection of ML methods and scientific areas, for instance, reviews highlight applying ML technologies in electron microscopy and SPM [381–383], using ML in materials properties prediction and data mining [384,385], leveraging artificial intelligence in quantum, atomistic, and continuum systems [386]. Most recently, the combination of ML and robotics has resulted in self-driven robotic chemist which aims to autonomous materials discovery [387,388]. In this part of the review, we will focus on the recent applications of ML methods in studying nanoobjects of single molecules and atoms on surfaces. This section will be divided into three pillars: (a) Detection and classification of molecular image, (b) Autonomous molecular imaging, (c) autonomous atom/molecule manipulation and nanofabrication. We hope to provide an overview of the recent developments of ML in surface-supported nano-species and the associated characterizations, but also encourage more engagements in applying these exciting tools in chemical researches.

6.1. Detection and classification of molecular image

The chemical and physical properties of molecules are determined by the combination and arrangement of their constituting atomic species. Yet, there are very few techniques which are able to resolve molecules down to single-molecule or even atomic level. SPM is best known for the real-space imaging of remarkable spatial resolution. The development of STM and AFM, has been widely used for characterizing the structural and electronic/magnetic properties of nanomaterials and molecules with unprecedented resolutions. Moreover, the widespread adoption of commercialized SPMs has significantly contributed to advances in the fields of surface self-assembly and on-surface synthesis [59,232].

However, the data analysis of molecular images obtained by high-resolution SPMs still heavily relies on human inspection, which is often subjective and error-prone although labor-intensive. ML techniques have been widely applied to deal with image and video tasks by extracting meaningful information. Using computers to derive intelligent understandings from data of images is also called computer version, a multidisciplinary field broadly considered as a subset of artificial intelligence and machine learning. Noteworthy, one should distinguish computer version from image processing which mainly involves signal processing but is not concerned with understanding the content of an image [389]. Typical tasks of computer version include object detection (concerning the position of objects in the image), object classification (the category of the object), key points detection (the key points for the object), object segmentation (pixels belong to the object) and image generation (style transfer or super resolution).

Recently, there have been increasing interest in applying ML methods for the automated analysis of single molecules or atoms from SPM images [390]. For instance, Ziatdinov and coauthors have applied computer vision to recognize the adsorption geometries of molecular assemblies on surfaces (Fig. 52a) [391]. Li *et al.* developed a deep learning framework based on computer vision for the classification of molecules with different chirality (Fig. 52b) [392]. Subsequently, the work on image classification by ML allowing for the recognition of the scanning tunneling tip states was demonstrated (Fig. 52c) [393]. The detection of different molecules can be used for the statistical analysis.

Although there are different models and algorithms for computer vision tasks on molecular images, *e.g.*, relying on the Zernike moments of the template images [394]. Convolutional neural networks (CNN) based ML models represent the most commonly considered ones because of their high performances in computer vision tasks and the relatively low cost (a fraction of second with the Faster RCNN algorithm). As displayed in Fig. 53, a general workflow for recognition of molecules in SPM images may consist of five main modules [395]. Starting from standard experimental image acquisition, the molecules of interest can be initially assessed by unsupervised algorithms. The procedure of the assessment is not necessary while still recommended, because it not only provides ideas on whether the target images are classifiable but also

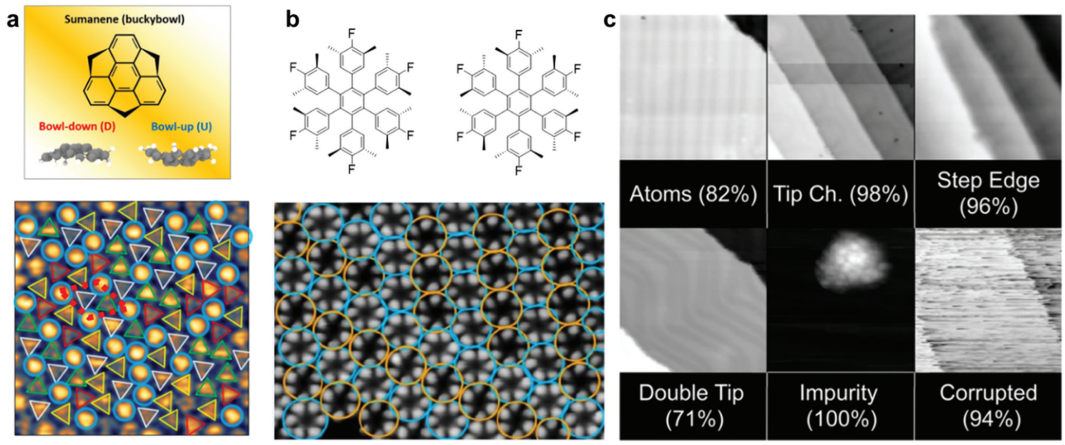

Fig. 52. Typical examples of applying computer vision in analyzing SPM images. (a) Molecular structure of Sumanene and two adsorption configurations. Visual inspection of different conformational and rotational states of the STM image [391]. (b) Molecular structures of the L-handed and R-handed molecules, and the ML inference results of analyzing STM molecular images [392]. (c) Classifying the tip states from STM imaging, the confidence thresholds of the convolutional neural networks are shown at the bottom of each class [393]. Reproduced with permission [391–393]. Copyright 2017, CC-BY 4.0; Copyright 2019, AIP Publishing; Copyright 2021, American Chemical Society.

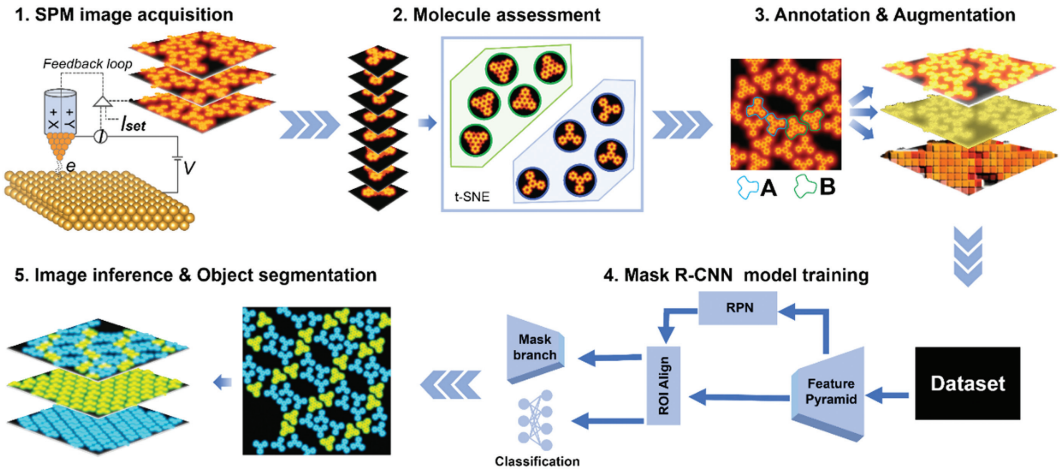

Fig. 53. Workflow of a ML Framework for the detecting and classification of molecular images. The workflow consists of image data acquisition, the assessment and annotation of the target molecules, dataset preparation and ML model training [395]. Reproduced with permission [395]. Copyright 2022, John Wiley and sons.

helps to pick out the ambiguous data for model training. To enrich the dataset and improve the model performance, data augmentations are routinely applied. Then, the labeled data will be provided to the ML model for training, and finally the well-trained model which has a good performance and generalization will be used to infer results. A notable CNN-based algorithm is Faster R-CNN for its much-improved efficiency for pixelwise objection detection, *i.e.*, semantic segmentation. Moreover, a further extension of the algorithm, mask R-CNN allows for instance segmentation of images or videos, *i.e.*, outputting masks of pixelwise accuracy for each identified species.

Similar workflow can be applied to arbitrary goals of molecule recognition. Yuan *et al.* developed a ML framework for molecular keypoint recognitions of STM images [396]. They employed the YOLO algorithm and labelled molecules with their keypoints, *i.e.*, the points track the molecular backbone. YOLO is a one-stage object detector based on CNN, using a single neural network to predict the bounding boxes and the class probabilities for these boxes. Therefore, it is faster and more efficient than the two-stage counterparts like R-CNN which composes a first stage to identify regions of interest and the second one for object classification in each region. The authors used the YOLO model to predict the keypoints of molecules, as marked by the blue dots in Fig. 54a and b. Consequently, structural properties like the symmetry of the molecules can be easily recognized through drawing the connections between the keypoints. Moreover, additional structural statistics were obtained with the predicted keypoints. Another application of this ML framework is to discover the lengths of polyphenylene chains fabricated from on-surface synthesis (Fig. 54c). This automated analysis alleviates the conventional human inspections which tend to be subject and error-prone.

In addition to inferring STM images of organic molecules, ML model was applied to identify the Bravais lattice of two-dimensional materials from the STM images [397]. Although the ML model was built on simulated STM images, it correctly predicts seven experimental images of two-dimensional materials out of nine. High-resolution AFM images contain few electronic contrasts but molecular bond information in contrast to STM images. Recently, success has been shown in the identification of the atomic structures of interfacial water/ionic hydrates by building ML models on high-resolution AFM images [398].

6.2. Autonomous molecular imaging

We have seen the successes achieved by using ML techniques to infer molecules or atoms in real-space microscopic images. Yet, constant manual supervisions are needed to achieve the required high resolutions in experiments. This calls for fully automated SPM

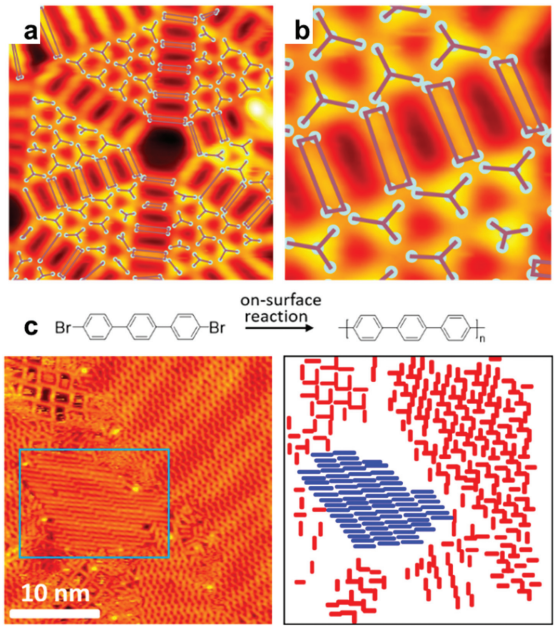

Fig. 54. Using ML to identity molecules and their keypoints from STM images. (a, b) The adopted YOLO model detects the molecules and identifies their keypoints (blue points). (c) On-surface synthesis leads to oligomers of different lengths. The different oligomers can be recognized by the ML model [396]. Reproduced with permission [396]. Copyright 2023, CC-BY 4.0.

which is able to perform routine operations such as approaching/withdrawing the probe, conditioning the tip state and tuning the scanning parameters, as well as achieve decision making and experiment planning. To realize the fully automated SPMs in molecular imaging, there have been increasing efforts towards this direction in recent years [399–401].

One of the most tedious but routine work in acquiring high-resolution SPM images lies in the tip conditions. The quality of the SPM images crucially depends on the atomic-scale morphology of the tip, and imaging artefacts like the "double-image" are frequently produced with a blunt tip. It is also challenging to prepare a perfect tip for performing STS since the electronic states from the tip will be convoluted into the experimental spectra. Common methods of tip conditioning consist of controlled tip indentation into the sample, and applying voltage pulses across the tip and sample. These processes typically need to be repeated a number of times to improve the tip quality, and still the tip quality may change from time to time depending on the imaging systems and tasks, or tip itself. Therefore, early works on autonomous molecular/atomic imaging targets at automated optimization of the tip states [402,403]. In this context, Rashidi *et al.* employed ML approaches to automatically detect and recondition the quality of the STM tip (Fig. 55a) [400]. The tip quality was assesses by evaluating images of silicon surfaces with known atomic defects though a CNN trained ML model. The tip conditioning was performed *in situ* by controlled tip indentation with the surface until a sharp tip as verified by the ML model was achieved. This ML based method has demonstrated its usefulness in the patterning of a binary atomic wire on silicon surface, showing its prospect in atomic atomic-precision nanofabrication.

Automated tip conditioning was also developed for STS, a technique that measures the differential conductance across the gap between the sample and tip, directly accessing the local density of states of the sample. Wang *et al.* demonstrated applying machine learning models to identify the point STS spectra for making decision on performing tip conditioning on clean surfaces (Fig. 55b) [404]. They used 1789 labeled dI/dV spectra to train ML models which then evaluated the states of the tip from the spectroscopic data. The quality of the tip is classified as five levels from grade 0 denoting good to grade 4 denoting bad. The tip of poor quality will be automatedly conditioned on a bare surface area that is determined by a height-based segmentation algorithm of the topographic images.

The capability of vertical atomic and molecular manipulation of SPM enables decorating at the tip apex with single atom or molecule. Such tip functionalization allows for constructing artificial atomic/molecular lattices [406] as well as additional characterizations such as magnetic property sensing [42,407] and force and charge measurements at single-bond resolution [408,409]. Therefore, it is desirable to achieve automated tip functionalization with known molecules or atoms. Alldritt *et al.* have developed a software package which is able to terminate the end of a STM/AFM tip with a CO molecule [405]. The software package combines ML models with automated software control of the experimental hardware for tip functionalization. As indicated in Fig. 55c, it works by the workflow of determining which molecules on a surface are carbon monoxide, controlling the tip position to perform procedures of tip functionalization, and assessing the tip quality with a ML model. The quality of CO functionalization is determined by solving a binary classification problem with the convolutional neural network (CNN) model. After training with the labeled database, the CNN model is used to evaluate the tip state by reviewing over images after tip changes.

The above-mentioned examples employing ML in molecular imaging accomplish improved efficiency of data analysis or data acquisition as well as the reduction of human operations. However, fully automated SPMs without human intervention were not realized. The vast majority of the constructed ML models are suitable for specific tasks but difficult to implement for general use. To realize self-driving autonomous SPM operation, an artificial intelligence framework aiming for driving autonomous continuous SPM data acquisition was demonstrated [401]. The framework named as DeepSPM functions by intelligently selecting scanning region, driving the SPM for acquiring molecular images, image assessment and making decision to store the image or modify the SPM parameters (Fig. 56a). Then, it continuously proceeds with the next loop iteration without the necessity of human intervention. The image is first assessed by measuring apparent height distributions, and then passed to a convolutional neural network for classification of the tip quality. Notably, DeepSPM leverages the deep reinforcement learning (RL) agent to condition the state of the probe, which allows for optimizing the data acquisition by intelligent selection of conditioning parameters for tip conditioning. In their tests, the number of conditioning steps by the RL agent is ∼28% smaller than when the conditioning actions are selected randomly. Finally, they demonstrated a continuous running time of 86 hours on a low-temperature STM setup to image magnesium phthalocyanine molecules on an Ag(100) surface. The scanning area covers over 1 μm^2, a total of more than 16000 images were saved and regions of different labels are shown in Fig. 56b. The implementation of RL optimizes the tip preparation protocol in an unsupervised, self-driven fashion. This opens the avenue to scalable atomically precise nano-fabrication as will be reviewed in the following.

6.3. Autonomous atom/molecule manipulations and nanofabrication

Reinforcement learning (RL) can be used to optimize atomic-scale manipulation, opening door to the constructions of complex molecular/atomic structures and quantum materials. RL or deep RL learns through trial-and-error by receiving positive and negative feedbacks without the need of pre-labeled training data. Therefore, one just needs to set the task to the ML model instead of specifying how to solve the task. For instance, Leinen *et al.* showed

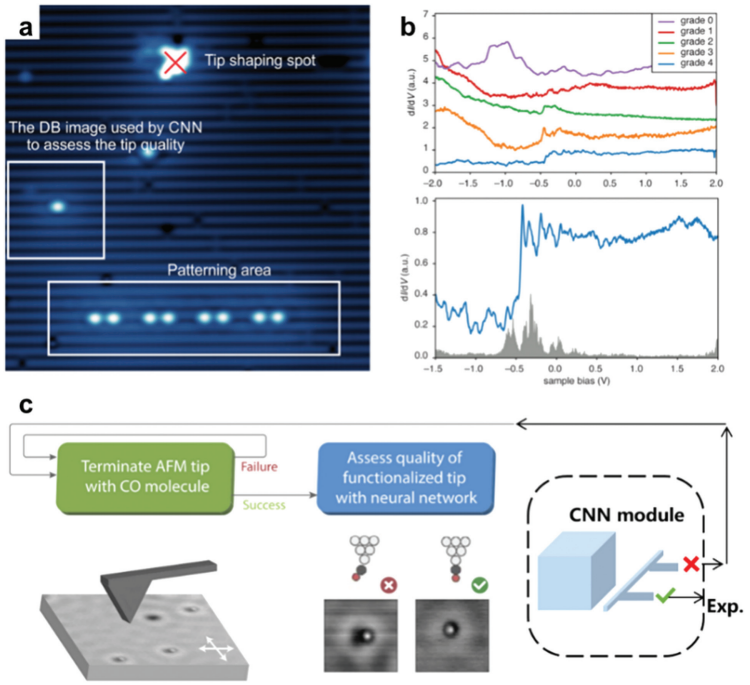

Fig. 55. Applying ML in SPM tip conditioning. (a) STM image of a silicon surface showing different areas for tip shaping, quality assessment and building binary atomic wire [400]. (b) Upper: STS spectra manually evaluated and assigned with different grades (from 0 to 4, meaning from poor to good). Lower: Importance of each data points on the classification of STS curves using a random forest ML model. The blue STS curve is classified as grade 4 and presented as reference [404]. (c) Schematic flowchart of the autonomous tip preparation procedure for functionalizing the SPM tip with CO [405]. Reproduced with permission [400,404,405]. Copyright 2018, 2021, American Chemical Society; Copyright 2022, CC-BY 4.0.

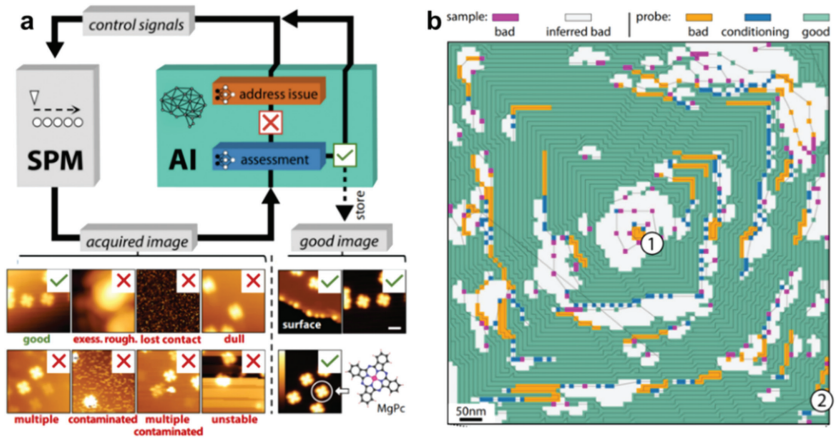

Fig. 56. (a) Schematic of the autonomous AI-driven SPM framework (DeepSPM). The framework employs ML models to autonomously determine the imaging region and acquire STM images, assess the image quality, and uses a deep reinforcement learning agent to condition the tip. (b) Example of long-term autonomous operation of DeepSPM. The green blocks denote valid regions scanned with a good tip, the magenta blocks indicate bad regions due to roughness, the orange ones show bad tips were detected, blue ones point to where tip-conditioning actions were performed, and gray regions suggest regions deemed bad [401]. Reproduced with permission [401]. Copyright 2020, CC-BY 4.0.

using RL approach in control of the SPM apparatus for removing molecules autonomously off a metal surface from a supramolecular structure [410]. Thanks to the self-adaptive nature through learning from new experiments, DL based manipulation intelligently selects parameters for manipulation tasks resulting in improved performance than manipulations with fixed parameters. The strategy can be transferred to fabricate complex quantum nanomaterial.

Beyond lifting nanoobjects, Chen *et al.* employed deep reinforcement learning (DRL) to control the atom manipulation process and built artificial atomic lattice [411]. In the task of atom manipulation, the goal is to move an adatom to a target position, which has been defined with a reward $r_t(s_t, a_t, s_{t+1})$ (Fig. 57a). Here, s_t, a_t and s_{t+1} denote state at time step t, action defined by policy π and state at time step $t+1$, respectively. The agent sequentially performs actions to alter the state s_t of this environment, and the information of (s_t, a_t, r_t, s_{t+1}) is used for training the DRL algorithm. Here, the DRL agent learns to manipulate Ag adatoms on Ag(111) surfaces with optimal precision. By further integrating with path-planning algorithms, they have achieved autonomous construction of an artificial kagome lattice composing 42-atom (Fig. 57b).

Additionally, RL approach has recently learned to control molecular movement of a single polar molecule triggered by a STM tip [412]. The investigated molecule possesses an intrinsic dipole moment, which allows for directional molecular manipulations *via* the localized electric field generated across the STM tip-sample junction. In this work, the RL agent learns by analyzing the STM image

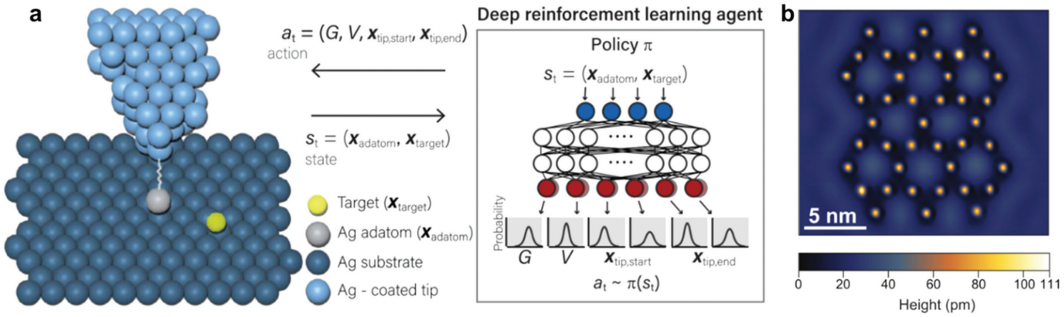

Fig. 57. (a) Atom manipulation controlled by the DRL agent. The agent learns a policy π for choosing actions a_t that maximize a sum over reward signals $r_t(s_t, a_t, s_{t+1})$. The action a_t contains information of the conductance G, bias V, and the 2D tip position at the start (end) of the manipulation $x_{tip,\,start}$ ($x_{tip,\,end}$). S_t includes coordinates of the current position of the adatom x_{adatom} and the target position x_{target}. (b) An artificial Kagome lattice constructed by a trained DRL agent together with path-planning algorithms [411]. Reproduced with permission [411]. Copyright 2022, CC-BY 4.0.

and extracting the position and orientation of the molecule before and after tip manipulation, those data representing the state information fed to the RL model. Applying voltage pulses at different tip positions around the center of the molecule for manipulation denote actions. The reward is defined by the distance between the molecule and the target destination after tip manipulation. Finally, after model training with around half a day, the RL agent is able to drive the molecule toward arbitrary positions and paths defined by a path-planning algorithm. A relatively complex moving trajectory resembling the shape of a fish was used to demonstrate the high performance of the well-trained RL agent. Moreover, the decisions made by the RL agent provide physical insight into the behaviors of polar molecules under an electric field.

In principle, the RL algorithm could be applied to any goal without a priori knowledge of the physical and chemical properties of the molecules or atoms. The combination of RL approach and SPM techniques furnishes a highly promising strategy for controllable molecular movements for applications such as molecular machine and nanofabrication.

7. Summary

Surface chemistry has proved to be an effective approach towards the preparation of numerous nanomaterials with appealing catalytic, electronic, magnetic and optical properties. Particularly, many materials are difficult to be obtained *via* the conventional organic synthesis in solution phase due to limited solubility and high reactivity, but can be precisely fabricated *via* the on-surface chemical synthesis with the atomic precision. Surface chemistry has grown to be a key subject and lies at the heart of an already significant range of researches covering fields such as quantum information, microelectronics, catalysts, and materials science.

It is highly challenging to fully obtain energy, time, and space information with currently used characterization approaches. For instance, acquiring non-planar molecular backbones using qplus AFM is particularly difficult. The ultimate goal is the integration of existing techniques and the creation of new methods to visualize and identify surface species at the femtosecond and subangstrom scale. Meanwhile, most vacuum-based techniques are unable to characterize surface properties and processes under realistic working conditions. To address this, new operando approaches are needed for real catalysis reactions and functional electronic devices. The combination of experimental techniques and artificial intelligence (AI) holds great promise for advancing the next generation of characterization methods.

Declaration of competing interest

The authors declare that they have no known competing financial interests or personal relationships that could have appeared to influence the work reported in this paper.

CRediT authorship contribution statement

Xin Li: Writing – original draft. **Zhen Xu:** Writing – original draft. **Donglei Bu:** Writing – original draft. **Jinming Cai:** Writing – original draft. **Huamei Chen:** Writing – original draft. **Qi Chen:** Writing – original draft. **Ting Chen:** Writing – original draft. **Fang Cheng:** Writing – original draft. **Lifeng Chi:** Writing – original draft. **Wenjie Dong:** Writing – original draft. **Zhenchao Dong:** Writing – original draft. **Shixuan Du:** Writing – original draft. **Qitang Fan:** Writing – original draft. **Xing Fan:** Writing – original draft. **Qiang Fu:** Writing – original draft. **Song Gao:** Writing – original draft. **Jing Guo:** Writing – original draft. **Weijun Guo:** Writing – original draft. **Yang He:** Writing – original draft. **Shimin Hou:** Writing – original draft. **Ying Jiang:** Writing – original draft. **Huihui Kong:** Writing – original draft. **Baojun Li:** Writing – original draft. **Dengyuan Li:** Writing – original draft. **Jie Li:** Writing – original draft. **Qing Li:** Writing – original draft. **Ruoning Li:** Writing – original draft. **Shuying Li:** Writing – original draft. **Yuxuan Lin:** Writing – original draft. **Mengxi Liu:** Writing – original draft. **Peinian Liu:** Writing – original draft. **Yanyan Liu:** Writing – original draft. **Jingtao Lü:** Writing – original draft. **Chuanxu Ma:** Writing – original draft. **Haoyang Pan:** Writing – original draft. **JinLiang Pan:** Writing – original draft. **Minghu Pan:** Writing – original draft. **Xiaohui Qiu:** Writing – original draft. **Ziyong Shen:** Writing – original draft. **Qiang Sun:** Writing – original draft. **Shijing Tan:** Writing – original draft. **Bing Wang:** Writing – original draft. **Dong Wang:** Writing – original draft. **Li Wang:** Writing – original draft. **Lili Wang:** Writing – original draft. **Tao Wang:** Writing – original draft. **Xiang Wang:** Writing – original draft. **Xingyue Wang:** Writing – original draft. **Xueyan Wang:** Writing – original draft. **Yansong Wang:** Writing – original draft. **Yu Wang:** Writing – original draft. **Kai Wu:** Writing – original draft. **Wei Xu:** Writing – original draft. **Na Xue:** Writing – original draft. **Linghao Yan:** Writing – original draft. **Fan Yang:** Writing – original draft. **Zhiyong Yang:** Writing – original draft. **Chi Zhang:** Writing – original draft. **Xue Zhang:** Writing – original draft. **Yang Zhang:** Writing – original draft. **Yao Zhang:** Writing – original draft. **Xiong Zhou:** Writing – original draft. **Junfa Zhu:** Writing – original draft. **Yajie Zhang:** Writing – review & editing, Writing – original draft, Supervision, Funding acquisition. **Feixue Gao:** Writing – review & editing, Writ-

ing – original draft, Supervision. **Yongfeng Wang:** Writing – review & editing, Writing – original draft, Supervision, Project administration, Funding acquisition.

References

[1] A. Glebov, A.P. Graham, A. Menzel, J.P. Toennies, J. Chem. Phys. 106 (1997) 9382–9385.
[2] K. Andersson, A. Nikitin, L.G.M. Pettersson, A. Nilsson, H. Ogasawara, Phys. Rev. Lett. 93 (2004) 196101.
[3] Y. Liu, M. Yang, J. Lu, et al., Chin. Chem. Lett. 33 (2022) 368–373.
[4] N. Katsonis, H. Xu, R.M. Haak, et al., Angew. Chem. Int. Ed. 47 (2008) 4997–5001.
[5] A. Hodgson, S. Haq, Surf. Sci. Rep. 64 (2009) 381–451.
[6] G.A. Kimmel, J. Matthiesen, M. Baer, et al., J. Am. Chem. Soc. 131 (2009) 12838–12844.
[7] L. Dong, P.N. Liu, N. Lin, Acc. Chem. Res. 48 (2015) 2765–2774.
[8] Y. Xie, C. Liu, L. Cheng, et al., Chin. Chem. Lett. 33 (2022) 4649–4654.
[9] M. Chen, J. Shang, Y.F. Wang, et al., ACS Nano 11 (2017) 134–143.
[10] H. Cao, S. De Feyter, Nat. Commun. 9 (2018) 3416.
[11] Z. Xu, J. Liu, S.M. Hou, Y.F. Wang, Nanomaterials 10 (2020) 2393.
[12] Y.R. Shen, V. Ostroverkhov, Chem. Rev. 106 (2006) 1140–1154.
[13] Y.F. Wang, M.J. Zhong, J. Li, et al., Chin. Chem. Lett. 33 (2022) 1074–1076.
[14] X. Zhang, N. Li, H. Wang, et al., ACS Nano 11 (2017) 8511–8518.
[15] X. Dai, L. Liu, Z. Ji, Q. Meng, Y. Zou, Chin. Chem. Lett. 34 (2023) 107239.
[16] J.Y. Park, L.R. Baker, G.A. Somorjai, Chem. Rev. 115 (2015) 2781–2817.
[17] Z. Wang, Q. Hong, B. Miao, et al., Chin. Chem. Lett. 35 (2024) 108458.
[18] P. Bellotti, M. Koy, M.N. Hopkinson, F. Glorius, Nat. Rev. Chem. 5 (2021) 711–725.
[19] Q. Liang, G. Feng, H. Ni, et al., Chin. Chem. Lett. 34 (2023) 108006.
[20] H.A. Lee, E. Park, H. Lee, Adv. Mater. 32 (2020) 1907505.
[21] E. Billeter, Z. Łodziana, A. Borgschulte, J. Phys. Chem. C 125 (2021) 25339–25349.
[22] G. Song, Y. Wang, D.Q. Tan, IET Nanodielectrics 5 (2022) 1–23.
[23] D.N.G. Krishna, J. Philip, Appl. Surf. Sci. Adv. 12 (2022) 100332.
[24] Y. Bai, M. Hao, S. Ding, P. Chen, L. Wang, Adv. Mater. 34 (2022) 2105958.
[25] D. Huang, T.A. Webb, C.L. Song, et al., Nano Lett. 16 (2016) 4224–4229.
[26] A.P. Bartók, S. De, C. Poelking, et al., Sci. Adv. 3 (2017) e1701816.
[27] Y.F. Geng, P. Li, J.Z. Li, et al., Coord. Chem. Rev. 337 (2017) 145–177.
[28] T. Niu, W. Zhou, D. Zhou, et al., Adv. Mater. 31 (2019) 1902606.
[29] X. Zhang, N. Xue, C. Li, et al., ACS Nano 13 (2019) 1385–1393.
[30] J. Lawrence, G.C. Sosso, L. Đorđević, et al., Nat. Commun. 11 (2020) 2103.
[31] T.S. Seifert, S. Kovarik, D.M. Juraschek, et al., Sci. Adv. 6 (2020) eabc5511.
[32] R.T. Hannagan, G. Giannakakis, R. Réocreux, et al., Science 372 (2021) 1444–1447.
[33] K.M. Roccapriore, Q. Zou, L. Zhang, et al., ACS Nano 15 (2021) 11806–11816.
[34] T. Qin, D. Guo, J. Xiong, et al., Angew. Chem. Int. Ed. 62 (2023) e202306368.
[35] Y. Xie, K. Sattari, C. Zhang, J. Lin, Prog. Mater. Sci. 132 (2023) 101043.
[36] G. Binnig, H. Rohrer, C. Gerber, E. Weibel, Phys. Rev. Lett. 49 (1982) 57–61.
[37] E. Betzig, R.J. Chichester, Science 262 (1993) 1422–1425.
[38] R. Berndt, R. Gaisch, J. Gimzewski, et al., Science 262 (1993) 1425–1427.
[39] H.J. Lee, W. Ho, Science 286 (1999) 1719–1722.
[40] R. Zhang, Y. Zhang, Z.C. Dong, et al., Nature 498 (2013) 82–86.
[41] P. Ruffieux, S. Wang, B. Yang, et al., Nature 531 (2016) 489–492.
[42] G. Czap, P.J. Wagner, F. Xue, et al., Science 364 (2019) 670–673.
[43] H. Imada, M. Imai-Imada, K. Miwa, et al., Science 373 (2021) 95–98.
[44] S. Yuan, Y. Zhou, T. Gao, et al., Chin. Chem. Lett. 35 (2024) 108404.
[45] A. Gaita-Ariño, F. Luis, S. Hill, E. Coronado, Nat. Chem. 11 (2019) 301–309.
[46] E. Moreno-Pineda, W. Wernsdorfer, Nat. Rev. Phys. 3 (2021) 645–659.
[47] H. Kurebayashi, J.H. Garcia, S. Khan, J. Sinova, S. Roche, Nat. Rev. Phys. 4 (2022) 150–166.
[48] J. Chakhalian, J.W. Freeland, G. Srajer, et al., Nat. Phys. 2 (2006) 244–248.
[49] A. Fernando, K.L.D.M. Weerawardene, N.V. Karimova, C.M. Aikens, Chem. Rev. 115 (2015) 6112–6216.
[50] R.N. Li, N. Li, H. Wang, et al., Chem. Commun. 54 (2018) 9135–9138.
[51] J.M.D. Coey, Nat. Mater. 18 (2019) 652–656.
[52] S. Song, J. Su, M. Telychko, et al., Chem. Soc. Rev. 50 (2021) 3238–3262.
[53] D.G. de Oteyza, T. Frederiksen, J. Phys.: Condens. Matter 34 (2022) 443001.
[54] H. Zhang, J. Lu, Y. Zhang, et al., Chin. Chem. Lett. 34 (2023) 107450.
[55] O.V. Yazyev, Rep. Prog. Phys. 73 (2010) 056501.
[56] S.S. Yan, J.Y. Wang, Z.Y. Pan, et al., Chin. Chem. Lett. 33 (2022) 3263–3266.
[57] S. Clair, D.G. de Oteyza, Chem. Rev. 119 (2019) 4717–4776.
[58] T. Wang, J.F. Zhu, Surf. Sci. Rep. 74 (2019) 97–140.
[59] R.S.K. Houtsma, J. de la Rie, M. Stöhr, Chem. Soc. Rev. 50 (2021) 6541–6568.
[60] Y. Zheng, C. Li, C. Xu, et al., Nat. Commun. 11 (2020) 6076.
[61] T. Wang, P. Angulo-Portugal, A. Berdonces-Layunta, et al., J. Am. Chem. Soc. 145 (2023) 10333–10341.
[62] S. Mishra, D. Beyer, K. Eimre, et al., Nat. Nanotechnol. 15 (2020) 22–28.
[63] N. Krane, E. Turco, A. Bernhardt, et al., Nano Lett. 23 (2023) 9353–9359.
[64] T. Wang, S. Sanz, J. Castro-Esteban, et al., Nano Lett. 22 (2022) 164–171.
[65] J. Kondo, Prog. Theor. Phys. 32 (1964) 37–49.
[66] M.J. Zhong, Q.M. Wu, L. Ma, et al., Chin. Chem. Lett. 34 (2023) 107813.
[67] H.O. Frota, Phys. Rev. B 45 (1992) 1096–1099.
[68] J. Li, S. Sanz, J. Castro-Esteban, et al., Phys. Rev. Lett. 124 (2020) 177201.
[69] X. Su, C. Li, Q. Du, et al., Nano Lett. 20 (2020) 6859–6864.
[70] S. Mishra, G. Catarina, F. Wu, et al., Nature 598 (2021) 287–292.
[71] T.A. Costi, Phys. Rev. Lett. 85 (2000) 1504–1507.
[72] N. Roch, S. Florens, T.A. Costi, W. Wernsdorfer, F. Balestro, Phys. Rev. Lett. 103 (2009) 197202.
[73] J.J. Parks, A.R. Champagne, T.A. Costi, et al., Science 328 (2010) 1370–1373.
[74] J. Li, S. Sanz, M. Corso, et al., Nat. Commun. 10 (2019) 200.
[75] H.Y. Gao, J.H. Franke, H. Wagner, et al., J. Phys. Chem. C 117 (2013) 18595–18602.
[76] K.A. Simonov, N.A. Vinogradov, A.S. Vinogradov, et al., J. Phys. Chem. C 118 (2014) 12532–12540.
[77] K.A. Simonov, N.A. Vinogradov, A.S. Vinogradov, et al., ACS Nano 9 (2015) 8997–9011.
[78] P.A. Held, H.Y. Gao, L. Liu, et al., Angew. Chem. Int. Ed. 55 (2016) 9777–9782.
[79] T. Wang, H. Lv, L. Feng, et al., J. Phys. Chem. C 122 (2018) 14537–14545.
[80] T. Wang, J. Huang, H. Lv, et al., J. Am. Chem. Soc. 140 (2018) 13421–13428.
[81] M. Hollerer, D. Lüftner, P. Hurdax, et al., ACS Nano 11 (2017) 6252–6260.
[82] K. Biswas, J.I. Urgel, K. Xu, et al., Angew. Chem. Int. Ed. 60 (2021) 25551–25556.
[83] T. Wang, A. Berdonces-Layunta, N. Friedrich, et al., J. Am. Chem. Soc. 144 (2022) 4522–4529.
[84] N. Pavliček, A. Mistry, Z. Majzik, et al., Nat. Nanotechnol. 12 (2017) 308–311.
[85] S. Mishra, D. Beyer, K. Eimre, et al., J. Am. Chem. Soc. 141 (2019) 10621–10625.
[86] J. Su, M. Telychko, P. Hu, et al., Sci. Adv. 5 (2019) eaav7717.
[87] S. Mishra, K. Xu, K. Eimre, et al., Nanoscale 13 (2021) 1624–1628.
[88] E. Turco, A. Bernhardt, N. Krane, et al., JACS Au 3 (2023) 1358–1364.
[89] E.H. Lich, Phys. Rev. Lett. 62 (1989) 1201–1204.
[90] M.E. Sandoval-Salinas, A. Carreras, D. Casanova, Phys. Chem. Chem. Phys. 21 (2019) 9069–9076.
[91] J. Su, W. Fan, P. Mutombo, et al., Nano Lett. 21 (2021) 861–867.
[92] S.J. Cyvin, J. Brunvoll, B.N. Cyvin, J. Math. Chem. 4 (1990) 47–54.
[93] W.L. Wang, O.V. Yazyev, S. Meng, E. Kaxiras, Phys. Rev. Lett. 102 (2009) 157201.
[94] S. Mishra, X. Yao, Q. Chen, et al., Nat. Chem. 13 (2021) 581–586.
[95] K. Biswas, D. Soler, S. Mishra, et al., J. Am. Chem. Soc. 145 (2023) 2968–2974.
[96] M. Solà, Front. Chem. 1 (2013) 00022.
[97] S.W. Slayden, J.F. Liebman, Chem. Rev. 101 (2001) 1541–1566.
[98] A. Konishi, Y. Hirao, M. Nakano, et al., J. Am. Chem. Soc. 132 (2010) 11021–11023.
[99] B.S. Rabinovitch, F.S. Looney, J. Chem. Phys. 23 (2014) 2439–2440.
[100] J. Li, S. Sanz, N. Merino-Díez, et al., Nat. Commun. 12 (2021) 5538.
[101] K. Biswas, J.I. Urgel, M.R. Ajayakumar, et al., Angew. Chem. Int. Ed. 61 (2022) e202114983.
[102] A. Sánchez-Grande, J.I. Urgel, L. Veis, et al., J. Phys. Chem. Lett. 12 (2021) 330–336.
[103] S. Mishra, D. Beyer, R. Berger, et al., J. Am. Chem. Soc. 142 (2020) 1147–1152.
[104] C.N. Yeh, J.D. Chai, Sci. Rep. 6 (2016) 30562.
[105] J.I. Urgel, H. Hayashi, M. Di Giovannantonio, et al., J. Am. Chem. Soc. 139 (2017) 11658–11661.
[106] M. Zugermeier, M. Gruber, M. Schmid, et al., Nanoscale 9 (2017) 12461–12469.
[107] R. Zuzak, R. Dorel, M. Kolmer, et al., Angew. Chem. Int. Ed. 57 (2018) 10500–10505.
[108] F. Eisenhut, J. Krüger, D. Skidin, et al., Nanoscale 10 (2018) 12582–12587.
[109] L. Colazzo, M.S.G. Mohammed, R. Dorel, et al., Chem. Commun. 54 (2018) 10260–10263.
[110] J.I. Urgel, S. Mishra, H. Hayashi, et al., Nat. Commun. 10 (2019) 861.
[111] F. Eisenhut, T. Kühne, F. García, et al., ACS Nano 14 (2020) 1011–1017.
[112] R. Zuzak, M. Kumar, O. Stoica, et al., Angew. Chem. Int. Ed. 63 (2024) e202317091.
[113] J. Hachmann, J.J. Dorando, M. Avilés, G.K.L. Chan, J. Chem. Phys. 127 (2007) 134309.
[114] S. Mishra, S. Fatayer, S. Fernández, et al., ACS Nano 16 (2022) 3264–3271.
[115] M. Di Giovannantonio, K. Eimre, A.V. Yakutovich, et al., J. Am. Chem. Soc. 141 (2019) 12346–12354.
[116] G.D. Nguyen, H.Z. Tsai, A.A. Omrani, et al., Nat. Nanotechnol. 12 (2017) 1077–1082.
[117] P.H. Jacobse, R.D. McCurdy, J. Jiang, et al., J. Am. Chem. Soc. 142 (2020) 13507–13514.
[118] C. Li, Y. Liu, Y. Liu, et al., CCS Chem. 5 (2022) 695–703.
[119] M. Di Giovannantonio, J.I. Urgel, U. Beser, et al., J. Am. Chem. Soc. 140 (2018) 3532–3536.
[120] M. Di Giovannantonio, Q. Chen, J.I. Urgel, et al., J. Am. Chem. Soc. 142 (2020) 12925–12929.
[121] F. Kang, L. Sun, W. Gao, Q. Sun, W. Xu, ACS Nano 17 (2023) 8717–8722.
[122] W. Xiong, J. Lu, J. Geng, et al., Appl. Surf. Sci. 609 (2023) 155315.
[123] P. Cui, Q. Zhang, H. Zhu, et al., Phys. Rev. Lett. 116 (2016) 026802.
[124] S. Kawai, K. Takahashi, S. Ito, et al., ACS Nano 11 (2017) 8122–8130.
[125] D.Y. Li, X. Qiu, S.W. Li, et al., J. Am. Chem. Soc. 143 (2021) 12955–12960.
[126] Z. Zeng, D. Guo, T. Wang, et al., J. Am. Chem. Soc. 144 (2022) 723–732.
[127] W.H. Soe, C. Manzano, A. De Sarkar, N. Chandrasekhar, C. Joachim, Phys. Rev. Lett. 102 (2009) 176102.
[128] C. Sánchez-Sánchez, T. Dienel, A. Nicolaï, et al., Chem. Eur. J. 25 (2019) 12074–12082.
[129] C. Sánchez-Sánchez, A. Nicolaï, F. Rossel, et al., J. Am. Chem. Soc. 139 (2017) 17617–17623.

[130] I. Izydorczyk, O. Stoica, M. Krawiec, et al., Chem. Commun. 58 (2022) 4063–4066.
[131] N. Friedrich, P. Brandimarte, J. Li, et al., Phys. Rev. Lett. 125 (2020) 146801.
[132] K. Sun, O.J. Silveira, S. Saito, et al., ACS Nano 16 (2022) 11244–11250.
[133] J. Lawrence, A. Berdonces-Layunta, S. Edalatmanesh, et al., Nat. Chem. 14 (2022) 1451–1458.
[134] J. Li, P. Brandimarte, M. Vilas-Varela, et al., ACS Nano 14 (2020) 1895–1901.
[135] Q. Sun, L.M. Mateo, R. Robles, et al., J. Am. Chem. Soc. 142 (2020) 18109–18117.
[136] Y. Zhao, K. Jiang, C. Li, et al., J. Am. Chem. Soc. 142 (2020) 18532–18540.
[137] J.P. Calupitan, A. Berdonces-Layunta, F. Aguilar-Galindo, et al., Nano Lett. 23 (2023) 9832–9840.
[138] M. Corso, D.G. de Oteyza, Nat. Nanotechnol. 15 (2020) 421–423.
[139] B. Cirera, A. Sánchez-Grande, B. de la Torre, et al., Nat. Nanotechnol. 15 (2020) 437–443.
[140] J. Lawrence, P. Brandimarte, A. Berdonces-Layunta, et al., ACS Nano 14 (2020) 4499–4508.
[141] D.J. Rizzo, G. Veber, T. Cao, et al., Nature 560 (2018) 204–208.
[142] O. Gröning, S. Wang, X. Yao, et al., Nature 560 (2018) 209–213.
[143] W.P. Su, J.R. Schrieffer, A.J. Heeger, Phys. Rev. Lett. 42 (1979) 1698–1701.
[144] H. González-Herrero, J.I. Mendieta-Moreno, S. Edalatmanesh, et al., Adv. Mater. 33 (2021) 2104495.
[145] Y. He, N. Li, I.E. Castelli, et al., Phys. Rev. Lett. 128 (2022) 236401.
[146] Q. Du, X. Su, Y. Liu, et al., Nat. Commun. 14 (2023) 4802.
[147] S. Mishra, D. Beyer, K. Eimre, et al., Angew. Chem. Int. Ed. 59 (2020) 12041–12047.
[148] J. Shang, Y. Wang, M. Chen, et al., Nat. Chem. 7 (2015) 389–393.
[149] F. Cheng, X.J. Wu, Z. Hu, et al., Nat. Commun. 9 (2018) 4871.
[150] Z. Tao, T. Wang, D. Wu, et al., Chem. Commun. 54 (2018) 7010–7013.
[151] J. Liu, Q. Chen, K. Cai, et al., Nat. Commun. 10 (2019) 2545.
[152] L. Feng, T. Wang, Z. Tao, et al., ACS Nano 13 (2019) 10603–10611.
[153] G. Galeotti, F. De Marchi, E. Hamzehpoor, et al., Nat. Mater. 19 (2020) 874–880.
[154] J. Hieulle, S. Castro, N. Friedrich, et al., Angew. Chem. Int. Ed. 60 (2021) 25224–25229.
[155] S. Cheng, Z. Xue, C. Li, et al., Nat. Commun. 13 (2022) 1705.
[156] Y. Zhao, K. Jiang, C. Li, et al., Nat. Chem. 15 (2023) 53–60.
[157] G. Zhu, Y. Jiang, Y. Wang, et al., J. Am. Chem. Soc. 145 (2023) 7136–7146.
[158] D.J. Rizzo, G. Veber, J. Jiang, et al., Science 369 (2020) 1597–1603.
[159] R.D. McCurdy, A. Delgado, J. Jiang, et al., J. Am. Chem. Soc. 145 (2023) 15162–15170.
[160] M. Bockrath, D.H. Cobden, J. Lu, et al., Nature 397 (1999) 598–601.
[161] Z.K. Tang, L. Zhang, N. Wang, et al., Science 292 (2001) 2462–2465.
[162] M. Koch, F. Ample, C. Joachim, L. Grill, Nat. Nanotechnol. 7 (2012) 713–717.
[163] R.E. Blackwell, F. Zhao, E. Brooks, et al., Nature 600 (2021) 647–652.
[164] H. Chen, Y. Chen, H. Zhang, et al., Chin. Chem. Lett. 33 (2022) 523–526.
[165] E.C.H. Wen, P.H. Jacobse, J. Jiang, et al., J. Am. Chem. Soc. 144 (2022) 13696–13703.
[166] S. Wang, L. Talirz, C.A. Pignedoli, et al., Nat. Commun. 7 (2016) 11507.
[167] S. Jiang, T. Neuman, A. Boeglin, F. Scheurer, G. Schull, Science 379 (2023) 1049–1054.
[168] Q. Sun, X.L. Yao, O. Groning, et al., Nano Lett. 20 (2020) 6429–6436.
[169] M. Kolmer, A.K. Steiner, I. Izydorczyk, et al., Science 369 (2020) 571–575.
[170] R. Zuzak, J. Castro-Esteban, M. Engelund, et al., ACS Nano 17 (2023) 2580–2587.
[171] C.X. Ma, J.F. Wang, H.H. Ma, et al., J. Am. Chem. Soc. 145 (2023) 10126–10135.
[172] Y. Li, A.T. Ngo, A. DiLullo, et al., Nat. Commun. 8 (2017) 946.
[173] D.M. Eigler, E.K. Schweizer, Nature 344 (1990) 524–526.
[174] D.J. Choi, N. Lorente, J. Wiebe, et al., Rev. Mod. Phys. 91 (2019) 041001.
[175] A.A. Khajetoorians, D. Wegner, A.F. Otte, I. Swart, Nat. Rev. Phys. 1 (2019) 703–715.
[176] R. Wiesendanger, Rev. Mod. Phys. 81 (2009) 1495.
[177] M. Ternes, New J. Phys. 17 (2015) 063016.
[178] A.J. Heinrich, J.A. Gupta, C.P. Lutz, D.M. Eigler, Science 306 (2004) 466–469.
[179] N. Tsukahara, K. Noto, M. Ohara, et al., Phys. Rev. Lett. 102 (2009) 167203.
[180] S. Baumann, F. Donati, S. Stepanow, et al., Phys. Rev. Lett. 115 (2015) 237202.
[181] S. Loth, M. Etzkorn, C.P. Lutz, D. Eigler, A.J. Heinrich, Science 329 (2010) 1628–1630.
[182] S. Baumann, W. Paul, T. Choi, et al., Science 350 (2015) 417–420.
[183] W. Paul, K. Yang, S. Baumann, et al., Nat. Phys. 13 (2016) 403–407.
[184] P. Willke, W. Paul, F.D. Natterer, et al., Sci. Adv. 4 (2018) eaaq1543.
[185] J.L. Lado, A. Ferrón, J. Fernández-Rossier, Phys. Rev. B 96 (2017) 205420.
[186] Y. Tokura, W.G. van der Wiel, T. Obata, S. Tarucha, Phys. Rev. Lett. 96 (2006) 047202.
[187] K. Yang, W. Paul, F.D. Natterer, et al., Phys. Rev. Lett. 122 (2019) 227203.
[188] J.R. Gálvez, C. Wolf, F. Delgado, N. Lorente, Phys. Rev. B 100 (2019) 035411.
[189] K. Yang, Y. Bae, W. Paul, et al., Phys. Rev. Lett. 119 (2017) 227206.
[190] L.M. Veldman, L. Farinacci, R. Rejali, et al., Science 372 (2021) 964–968.
[191] Y. Bae, K. Yang, P. Willke, et al., Sci. Adv. 4 (2018) eaau4159.
[192] L.M. Vandersypen, I.L. Chuang, Rev. Mod. Phys. 76 (2005) 1037.
[193] P. Neumann, J. Beck, M. Steiner, et al., Science 329 (2010) 542–544.
[194] M.T. Madzik, S. Asaad, A. Youssry, et al., Nature 601 (2022) 348–353.
[195] B. Stipe, M. Rezaei, W. Ho, Phys. Rev. Lett. 81 (1998) 1263.
[196] F.D. Natterer, F. Patthey, H. Brune, Phys. Rev. Lett. 111 (2013) 175303.
[197] P. Willke, Y. Bae, K. Yang, et al., Science 362 (2018) 336–339.
[198] J. Kim, K. Noh, Y. Chen, et al., Nano Lett. 22 (2022) 9766–9772.
[199] L. Farinacci, L.M. Veldman, P. Willke, S. Otte, Nano Lett. 22 (2022) 8470–8474.
[200] K. Yang, P. Willke, Y. Bae, et al., Nat. Nanotechnol. 13 (2018) 1120–1125.
[201] A.J. Heinrich, W.D. Oliver, L.M.K. Vandersypen, et al., Nat. Nanotechnol. 16 (2021) 1318–1329.
[202] D.D. Awschalom, R. Hanson, J. Wrachtrup, B.B. Zhou, Nat. Photonics 12 (2018) 516–527.
[203] K. Yang, W. Paul, S.H. Phark, et al., Science 366 (2019) 509–512.
[204] J.T. Muhonen, J.P. Dehollain, A. Laucht, et al., Nat. Nanotechnol. 9 (2014) 986–991.
[205] Y. Wang, M. Haze, H.T. Bui, et al., npj Quantum Inf. 9 (2023) 48.
[206] E. Kawakami, P. Scarlino, D.R. Ward, et al., Nat. Nanotechnol. 9 (2014) 666–670.
[207] B. Chen, J. Geng, F. Zhou, et al., Appl. Phys. Lett. 114 (2019) 041102.
[208] X. Zhang, C. Wolf, Y. Wang, et al., Nat. Chem. 14 (2022) 59–65.
[209] S. Bayliss, D. Laorenza, P. Mintun, et al., Science 370 (2020) 1309–1312.
[210] X. Zhang, J. Reina-Gálvez, C. Wolf, et al., ACS Nano 17 (2023) 16935–16942.
[211] P. Willke, T. Bilgeri, X. Zhang, et al., ACS Nano 15 (2021) 17959–17965.
[212] S. Kovarik, R. Robles, R. Schlitz, et al., Nano Lett. 22 (2022) 4176–4181.
[213] R. Kawaguchi, K. Hashimoto, T. Kakudate, et al., Nano Lett. 23 (2022) 213–219.
[214] Y. Wang, Y. Chen, H.T. Bui, et al., Science 382 (2023) 87–92.
[215] C.L. Kane, E.J. Mele, Phys. Rev. Lett. 95 (2005) 226801.
[216] A.K. Geim, K.S. Novoselov, Nat. Mater. 6 (2007) 183–191.
[217] M.S. Xu, T. Liang, M.M. Shi, H.Z. Chen, Chem. Rev. 113 (2013) 3766–3798.
[218] P. Miró, M. Audiffred, T. Heine, Chem. Soc. Rev. 43 (2014) 6537–6554.
[219] M. Acerce, D. Voiry, M. Chhowalla, Nat. Nanotechnol. 10 (2015) 313–318.
[220] B.A. Bernevig, T.L. Hughes, S.C. Zhang, Science 314 (2006) 1757–1761.
[221] M. Konig, S. Wiedmann, C. Brune, et al., Science 318 (2007) 766–770.
[222] A.H. Castro Neto, F. Guinea, N.M.R. Peres, K.S. Novoselov, A.K. Geim, Rev. Mod. Phys. 81 (2009) 109–162.
[223] M.Z. Hasan, C.L. Kane, Rev. Mod. Phys. 82 (2010) 3045–3067.
[224] F. Yang, L. Miao, Z.F. Wang, et al., Phys. Rev. Lett. 109 (2012) 016801.
[225] S.F. Wu, V. Fatemi, Q.D. Gibson, et al., Science 359 (2018) 76–79.
[226] H. Tasaki, Phys. Rev. Lett. 69 (1992) 1608–1611.
[227] A. Mielke, J. Phys. A: Math. Gen. 25 (1992) 4335–4345.
[228] E. Tang, J.W. Mei, X.G. Wen, Phys. Rev. Lett. 106 (2011) 236802.
[229] S. Mukherjee, A. Spracklen, D. Choudhury, et al., Phys. Rev. Lett. 114 (2015) 245504.
[230] Y.Y. Zong, S.Q. Xia, L.Q. Tang, et al., Opt. Express 24 (2016) 8877–8885.
[231] X.H. Liu, C.Z. Guan, S.Y. Ding, et al., J. Am. Chem. Soc. 135 (2013) 10470–10474.
[232] L. Dong, Z.A. Gao, N. Lin, Prog. Surf. Sci. 91 (2016) 101–135.
[233] H. Sun, S.J. Tan, M. Feng, J. Zhao, H. Petek, J. Phys. Chem. C 122 (2018) 18659–18668.
[234] Q. Xue, N. Xue, J. Li, et al., J. Phys. Chem. C 124 (2020) 7790–7796.
[235] C.Y. Yuan, N. Xue, Y.J. Zhang, et al., J. Clust. Sci. 32 (2021) 327–330.
[236] C.K. Lyu, Y.F. Gao, Z.A. Gao, et al., Angew. Chem. Int. Ed. 61 (2022) e202204528.
[237] Q. Zhong, K. Niu, L. Chen, et al., J. Am. Chem. Soc. 144 (2022) 8214–8222.
[238] R.N. Li, X. Zhang, N. Xue, et al., Acta Phys. Chim. Sin. 38 (2022) 2011060.
[239] A. Kumar, K. Banerjee, A.S. Foster, P. Liljeroth, Nano Lett. 18 (2018) 5596-5602.
[240] Z.L. Shi, N. Lin, J. Am. Chem. Soc. 131 (2009) 5376–5377.
[241] M. Abel, S. Clair, O. Ourdjini, M. Mossoyan, L. Porte, J. Am. Chem. Soc. 133 (2011) 1203–1205.
[242] T. Lin, G.W. Kuang, X.S. Shang, P.N. Liu, N. Lin, Chem. Commun. 50 (2014) 15327–15329.
[243] R.N. Li, N. Xue, X. Zhang, et al., J. Phys. Chem. C 125 (2021) 5581–5586.
[244] Z.F. Wang, Z. Liu, F. Liu, Phys. Rev. Lett. 110 (2013) 196801.
[245] Z. Liu, Z.F. Wang, J.W. Mei, Y.S. Wu, F. Liu, Phys. Rev. Lett. 110 (2013) 106804.
[246] N.H. Su, W. Jiang, Z.F. Wang, F. Liu, Appl. Phys. Lett. 112 (2018) 033301.
[247] H.J. Kim, C. Li, J. Feng, J.H. Cho, Z.Y. Zhang, Phys. Rev. B 93 (2016) 041404.
[248] Z.F. Wang, N. Su, F. Liu, Nano Lett. 13 (2013) 2842–2845.
[249] L.Z. Zhang, Z.F. Wang, B. Huang, et al., Nano Lett. 16 (2016) 2072–2075.
[250] J. Zhang, A. Shchyrba, S. Nowakowska, et al., Chem. Commun. 50 (2014) 12289–12292.
[251] L.H. Yan, O.J. Silveira, B. Alldritt, et al., ACS Nano 15 (2021) 17813–17819.
[252] S.H. Zhang, M. Kang, H.Q. Huang, et al., Phys. Rev. B 99 (2019) 100404.
[253] Y.X. Gao, Y.Y. Zhang, J.T. Sun, et al., Nano Res. 13 (2020) 1571–1575.
[254] J. Zhou, Q. Sun, J. Am. Chem. Soc. 133 (2011) 15113–15119.
[255] J.I. Urgel, M. Schwarz, M. Garnica, et al., J. Am. Chem. Soc. 137 (2015) 2420–2423.
[256] T.F. Wang, W.B. Huang, T. Sun, et al., ACS Appl. Mater. Interfaces 12 (2020) 46565–46570.
[257] W. Jiang, S.H. Zhang, Z.F. Wang, F. Liu, T. Low, Nano Lett. 20 (2020) 1959–1966.
[258] M.G. Kang, S.A. Fang, L.D. Ye, et al., Nat. Commun. 11 (2020) 4004.
[259] T.X. Li, S.W. Jiang, B.W. Shen, et al., Nature 600 (2021) 641–646.
[260] J.W. Rhim, K. Kim, B.J. Yang, Nature 584 (2020) 59–63.
[261] Y. Choi, H. Kim, Y. Peng, et al., Nature 589 (2021) 536–541.
[262] H.Y. Li, S.W. Li, E.C. Regan, et al., Nature 597 (2021) 650–654.
[263] X. Wang, C.X. Xiao, H. Park, et al., Nature 604 (2022) 468–473.
[264] Z.Y. Lin, J.H. Choi, Q. Zhang, et al., Phys. Rev. Lett. 121 (2018) 096401.
[265] Z.H. Liu, M. Li, Q. Wang, et al., Nat. Commun. 11 (2020) 4002.
[266] T.Y. Yang, Q. Wan, J.P. Song, et al., Quantum Front. 1 (2022) 14.
[267] S. Lisi, X. Lu, T. Benschop, et al., Nat. Phys. 17 (2021) 189–193.
[268] T. Yilmaz, X. Tong, Z. Dai, et al., Commun. Mater. 2 (2021) 11.

[269] T. Kambe, R. Sakamoto, T. Kusamoto, et al., J. Am. Chem. Soc. 136 (2014) 14357–14360.
[270] W. Jiang, X. Ni, F. Liu, Acc. Chem. Res. 54 (2021) 416–426.
[271] W. Jiang, H. Huang, F. Liu, Nat. Commun. 10 (2019) 2207.
[272] B. Cui, X. Zheng, J. Wang, et al., Nat. Commun. 11 (2020) 66.
[273] Y. Jing, T. Heine, Nat. Mater. 19 (2020) 823–824.
[274] S. Ghosh, Y. Tsutsui, T. Kawaguchi, et al., Chem. Mater. 34 (2022) 736–745.
[275] L. Chen, M. Huang, B. Chen, et al., Chin. Chem. Lett. 33 (2022) 2867–2882.
[276] C.H. Liu, A. Wei, M.F. Cheung, D.F. Perepichka, Chem. Mater. 34 (2022) 3461–3467.
[277] I. Piquero-Zulaica, A. Sadeghi, M. Kherelden, et al., Phys. Rev. Lett. 123 (2019) 266805.
[278] L. Yan, O.J. Silveira, B. Alldritt, et al., Adv. Funct. Mater. 31 (2021) 2100519.
[279] Z.J. Xue, F.W. Gan, H. Liu, et al., CCS Chem. 4 (2022) 1405–1413.
[280] S. Baidya, S. Kang, C.H. Kim, J. Yu, Sci. Rep. 9 (2019) 13807.
[281] Z.F. Wang, Z. Liu, F. Liu, Nat. Commun. 4 (2013) 1471.
[282] G. Koller, S. Berkebile, M. Oehzelt, et al., Science 317 (2007) 351–355.
[283] S. Ciuchi, R.C. Hatch, H. Höchst, et al., Phys. Rev. Lett. 108 (2012) 256401.
[284] L. Hernández-López, I. Piquero-Zulaica, C.A. Downing, et al., Nanoscale 13 (2021) 5216–5223.
[285] M. Pan, X. Zhang, Y. Zhou, et al., Phys. Rev. Lett. 130 (2023) 036203.
[286] C. Xie, Q.M. Wu, R.N. Li, et al., Chin. Chem. Lett. 27 (2016) 807–812.
[287] Y.J. Zhang, P.L. Liao, J.L. Kan, et al., Phys. Chem. Chem. Phys. 17 (2015) 27019–27026.
[288] Y. He, Y.J. Zhang, I.P. Hong, et al., Nanoscale 6 (2014) 10779–10783.
[289] J. Yang, X. Liu, Q. Dong, et al., Chin. Chem. Lett. 33 (2022) 177–185.
[290] Z. Yin, L. Xie, W. Yin, et al., Chin. Chem. Lett. 35 (2024) 108628.
[291] X. Zhao, A. Adijiang, D. Xiang, Chin. Chem. Lett. 34 (2023) 108381.
[292] G. Gong, M. Li, N. Sun, et al., Chin. Chem. Lett. 35 (2024) 108705.
[293] N. Nilius, A. Cörper, G. Bozdech, N. Ernst, H.J. Freund, Prog. Surf. Sci. 67 (2001) 99–121.
[294] N.J. Watkins, J.P. Long, Z.H. Kafafi, A.J. Mäkinen, Rev. Sci. Instrum. 78 (2007) 053707.
[295] L.G. Chen, C. Zhang, R. Zhang, X.L. Zhang, Z.C. Dong, Rev. Sci. Instrum. 84 (2013) 066106.
[296] R. Berndt, R.R. Schlittler, J.K. Gimzewski, J. Vac. Sci. Technol. B Microelectron. Nanometer Struct.-Process. Meas. Phenom. 9 (1991) 573–577.
[297] Y. Suzuki, H. Minoda, N. Yamamoto, Surf. Sci. 438 (1999) 297–304.
[298] M.J. Romero, J. van de Lagemaat, I. Mora-Sero, G. Rumbles, M.M. Al-Jassim, Nano Lett. 6 (2006) 2833–2837.
[299] T. Tsuruoka, S. Ushioda, J. Electron Microsc. 53 (2004) 169–175.
[300] M. Sakurai, C. Thirstrup, M. Aono, Appl. Phys. A 80 (2005) 1153–1160.
[301] G. Hoffmann, J. Kröger, R. Berndt, Rev. Sci. Instrum. 73 (2002) 305–309.
[302] Z.B. Wu, Z.Y. Gao, X.Y. Chen, et al., Rev. Sci. Instrum. 89 (2018) 113705.
[303] K. Kuhnke, C. Große, P. Merino, K. Kern, Chem. Rev. 117 (2017) 5174–5222.
[304] L.E.P. López, A. Rosławska, F. Scheurer, S. Berciaud, G. Schull, Nat. Mater. 22 (2023) 482–488.
[305] Z.C. Dong, Y. Zhang, X. Tao, J.L. Yang, J.G. Hou, Chin. Sci. Bull. 54 (2009) 984–998.
[306] L. Novotny, B. Hecht, Principles of Nano-optics, Cambridge University Press, 2012.
[307] C.J. Chen, Introduction to Scanning Tunneling Microscopy, Oxford University Press on Demand, 1993.
[308] B. Yang, G. Chen, A. Ghafoor, et al., Nat. Photonics 14 (2020) 693–699.
[309] N. Behr, M.B. Raschke, J. Phys. Chem. C 112 (2008) 3766–3773.
[310] M. Urbieta, M. Barbry, Y. Zhang, et al., ACS Nano 12 (2018) 585–595.
[311] J.K. Gimzewski, B. Reihl, J.H. Coombs, R.R. Schlittler, Z. Phys. B: Condens. Matter 72 (1988) 497–501.
[312] G. Hoffmann, L. Libioulle, R. Berndt, Phys. Rev. B 65 (2002) 212107.
[313] Z.C. Dong, A.S. Trifonov, X.L. Guo, et al., Surf. Sci. 532–535 (2003) 237–243.
[314] F. Geng, Y. Zhang, Y. Yu, et al., Opt. Express 20 (2012) 26725–26735.
[315] C. Große, A. Kabakchiev, T. Lutz, et al., Nano Lett. 14 (2014) 5693–5697.
[316] X.H. Qiu, G.V. Nazin, W. Ho, Science 299 (2003) 542–546.
[317] Z.C. Dong, X.L. Guo, A.S. Trifonov, et al., Phys. Rev. Lett. 92 (2004) 086801.
[318] E. Cavar, M.C. Blum, M. Pivetta, et al., Phys. Rev. Lett. 95 (2005) 196102.
[319] F. Matino, G. Schull, F. Köhler, et al., Proc. Natl. Acad. Sci. U. S. A. 108 (2011) 961–964.
[320] N.L. Schneider, F. Matino, G. Schull, et al., Phys. Rev. B 84 (2011) 153403.
[321] S.E. Zhu, Y.M. Kuang, F. Geng, et al., J. Am. Chem. Soc. 135 (2013) 15794–15800.
[322] T. Ijaz, B. Yang, R. Wang, et al., Appl. Phys. Lett. 115 (2019) 173101.
[323] M.C. Chong, G. Reecht, H. Bulou, et al., Phys. Rev. Lett. 116 (2016) 036802.
[324] C. Zhang, R. Zhang, S. Jiang, et al., Appl. Phys. Lett. 100 (2012) 073111.
[325] Z.C. Dong, X.L. Zhang, H.Y. Gao, et al., Nat. Photonics 4 (2010) 50–54.
[326] C. Chen, P. Chu, C.A. Bobisch, D.L. Mills, W. Ho, Phys. Rev. Lett. 105 (2010) 217402.
[327] Y. Zhang, Y. Luo, Y. Zhang, et al., Nature 531 (2016) 623–627.
[328] Y. Luo, G. Chen, Y. Zhang, et al., Phys. Rev. Lett. 122 (2019) 233901.
[329] H. Imada, K. Miwa, M. Imai-Imada, et al., Nature 538 (2016) 364–367.
[330] S. Cao, A. Roslawska, B. Doppagne, et al., Nat. Chem. 13 (2021) 766–770.
[331] F.F. Kong, X.J. Tian, Y. Zhang, et al., Nat. Nanotechnol. 17 (2022) 729–736.
[332] E.H. Synge, Philos. Mag. 6 (1928) 356–362.
[333] D.W. Pohl, W. Denk, M. Lanz, Appl. Phys. Lett. 44 (1984) 651–653.
[334] A. Lewis, M. Isaacson, A. Harootunian, A. Muray, Ultramicroscopy 13 (1984) 227–231.
[335] J. Duan, Y. Li, Y. Zhou, Y. Cheng, J. Chen, Adv. Phys. X 4 (2019) 1593051.
[336] H.G. Frey, S. Witt, K. Felderer, R. Guckenberger, Phys. Rev. Lett. 93 (2004) 200801.
[337] P. Anger, P. Bharadwaj, L. Novotny, Phys. Rev. Lett. 96 (2006) 113002.
[338] S. Kühn, U. Håkanson, L. Rogobete, V. Sandoghdar, Phys. Rev. Lett. 97 (2006) 017402.
[339] C. Höppener, Z.J. Lapin, P. Bharadwaj, L. Novotny, Phys. Rev. Lett. 109 (2012) 017402.
[340] E.A. Pozzi, G. Goubert, N. Chiang, et al., Chem. Rev. 117 (2017) 4961–4982.
[341] M. Richard-Lacroix, Y. Zhang, Z.C. Dong, V. Deckert, Chem. Soc. Rev. 46 (2017) 3922–3944.
[342] X. Shi, N. Coca-López, J. Janik, A. Hartschuh, Chem. Rev. 117 (2017) 4945–4960.
[343] S. Mahapatra, L. Li, J.F. Schultz, N. Jiang, J. Chem. Phys. 153 (2020) 010902.
[344] T. Itoh, M. Prochazka, Z.C. Dong, et al., Chem. Rev. 123 (2023) 1552–1634.
[345] B. Yang, Y. Zhang, Y. Zhang, Z.C. Dong, Chin. J. Vac. Sci. Technol. 41 (2021) 835–849.
[346] E.Le Ru, P. Etchegoin, Principles of Surface-Enhanced Raman Spectroscopy and Related Plasmonic Effects, Elsevier, 2008.
[347] P. Alonso-González, P. Albella, M. Schnell, et al., Nat. Commun. 3 (2012) 684.
[348] X. Wang, S.C. Huang, S. Hu, S. Yan, B. Ren, Nat. Rev. Phys. 2 (2020) 253–271.
[349] P. Kambhampati, C. Child, M.C. Foster, A. Campion, J. Chem. Phys. 108 (1998) 5013–5026.
[350] N. Valley, N. Greeneltch, R.P. Van Duyne, G.C. Schatz, J. Phys. Chem. Lett. 4 (2013) 2599–2604.
[351] J.R. Lombardi, R.L. Birke, J. Phys. Chem. C 112 (2008) 5605–5617.
[352] R.M. Stöckle, Y.D. Suh, V. Deckert, R. Zenobi, Chem. Phys. Lett. 318 (2000) 131–136.
[353] M.S. Anderson, Appl. Phys. Lett. 76 (2000) 3130–3132.
[354] N. Hayazawa, Y. Inouye, Z. Sekkat, S. Kawata, Opt. Commun. 183 (2000) 333–336.
[355] B. Pettinger, G. Picardi, R. Schuster, G. Ertl, Electrochem. Jpn. 68 (2000) 942–949.
[356] A. Hartschuh, E.J. Sánchez, X.S. Xie, L. Novotny, Phys. Rev. Lett. 90 (2003) 095503.
[357] J. Steidtner, B. Pettinger, Phys. Rev. Lett. 100 (2008) 236101.
[358] T.A. Yano, P. Verma, Y. Saito, T. Ichimura, S. Kawata, Nat. Photonics 3 (2009) 473–477.
[359] S. Jiang, Y. Zhang, R. Zhang, et al., Nat. Nanotechnol. 10 (2015) 865–869.
[360] N. Chiang, X. Chen, G. Goubert, et al., Nano Lett. 16 (2016) 7774–7778.
[361] J.F. Schultz, L. Li, S. Mahapatra, et al., J. Phys. Chem. C 124 (2019) 2420–2426.
[362] J. Lee, K.T. Crampton, N. Tallarida, V.A. Apkarian, Nature 568 (2019) 78–82.
[363] Y. Zhang, B. Yang, A. Ghafoor, et al., Natl. Sci. Rev. 6 (2019) 1169–1175.
[364] R.P. Wang, B. Yang, Q. Fu, et al., J. Phys. Chem. Lett. 12 (2021) 1961–1968.
[365] X. Dong, B. Yang, R. Zhu, et al., Light Adv. Manuf. 3 (2022) 729–738.
[366] J. Xu, X. Zhu, S. Tan, et al., Science 371 (2021) 818–822.
[367] X. Zhu, J. Xu, Y. Zhang, et al., J. Am. Ceram. Soc. 145 (2023) 13839–13845.
[368] J.H. Zhong, X. Jin, L. Meng, et al., Nat. Nanotechnol. 12 (2017) 132–136.
[369] H.S. Su, X.G. Zhang, J.J. Sun, et al., Angew. Chem. Int. Ed. 57 (2018) 13177–13181.
[370] H.S. Su, H.S. Feng, Q.Q. Zhao, et al., J. Am. Chem. Soc. 142 (2020) 1341–1347.
[371] L. Li, J.F. Schultz, S. Mahapatra, et al., Angew. Chem. Int. Ed. 62 (2023) e202306590.
[372] S. Sheng, J.b. Wu, X. Cong, et al., Phys. Rev. Lett. 119 (2017) 196803.
[373] A.C. Gadelha, D.A.A. Ohlberg, C. Rabelo, et al., Nature 590 (2021) 405–409.
[374] S. Berweger, M.B. Raschke, Anal. Bioanal. Chem. 396 (2010) 115–123.
[375] M.I. Jordan, T.M. Mitchell, Science 349 (2015) 255–260.
[376] O. Vinyals, I. Babuschkin, W.M. Czarnecki, et al., Nature 575 (2019) 350–354.
[377] J. Fang, M. Xie, X. He, et al., Mater. Today Commun. 33 (2022) 104900.
[378] Y. Liu, A.N. Morozovska, E.A. Eliseev, et al., Patterns 4 (2023) 100704.
[379] N.J. Szymanski, B. Rendy, Y. Fei, et al., Nature 624 (2023) 86–91.
[380] Q. Zhu, F. Zhang, Y. Huang, et al., Natl. Sci. Rev. 9 (2022) nwac190.
[381] J.M. Ede, Mach. Learn.: Sci. Technol. 2 (2021) 011004.
[382] S.V. Kalinin, M. Ziatdinov, J. Hinkle, et al., ACS Nano 15 (2021) 12604–12627.
[383] S.V. Kalinin, C. Ophus, P.M. Voyles, et al., Nat. Rev. Methods Prim. 2 (2022) 11.
[384] D. Packwood, L.T.H. Nguyen, P. Cesana, et al., Mach. Learn. Appl. 8 (2022) 100265.
[385] K. Choudhary, B. DeCost, C. Chen, et al., npj Comput. Mater. 8 (2022) 59.
[386] X. Zhang, L. Wang, J. Helwig, et al., arXiv:2307.08423 (2023).
[387] M. Abolhasani, E. Kumacheva, Nat. Synth. 2 (2023) 483–492.
[388] J.M. Gregoire, L. Zhou, J.A. Haber, Nat. Synth. 2 (2023) 493–504.
[389] R. Szeliski, Computer Vision: Algorithms and Applications, Springer Nature, 2022.
[390] O.M. Gordon, P.J. Moriarty, Mach. Learn.: Sci. Technol. 1 (2020) 023001.
[391] M. Ziatdinov, A. Maksov, S.V. Kalinin, npj Comput. Mater. 3 (2017) 31.
[392] J. Li, M. Telychko, J. Yin, et al., J. Am. Chem. Soc. 143 (2021) 10177–10188.
[393] O. Gordon, P. D'Hondt, L. Knijff, et al., Rev. Sci. Instrum. 90 (2019) 103704.
[394] J. Hellerstedt, A. Cahlík, M. Švec, O. Stetsovych, T. Hennen, Softw. Impacts 12 (2022) 100301.
[395] Z. Zhu, J. Lu, F. Zheng, et al., Angew. Chem. Int. Ed. 61 (2022) e202213503.
[396] S. Yuan, Z. Zhu, J. Lu, et al., Molecules 28 (2023) 5387.
[397] K. Choudhary, K.F. Garrity, C. Camp, et al., Sci. Data 8 (2021) 57.
[398] B. Tang, Y. Song, M. Qin, et al., Natl. Sci. Rev. 10 (2023) nwac282.
[399] F.E. Kalff, M.P. Rebergen, E. Fahrenfort, et al., Nat. Nanotechnol. 11 (2016) 926–929.
[400] M. Rashidi, R.A. Wolkow, ACS Nano 12 (2018) 5185–5189.

[401] A. Krull, P. Hirsch, C. Rother, A. Schiffrin, C. Krull, Commun. Phys. 3 (2020) 54.
[402] R.A.J. Woolley, J. Stirling, A. Radocea, N. Krasnogor, P. Moriarty, Appl. Phys. Lett. 98 (2011) 253104.
[403] M. Muller, S.P. Jarvis, L. Guérinet, et al., Nanotechnology 28 (2017) 075302.
[404] S. Wang, J. Zhu, R. Blackwell, F.R. Fischer, J. Phys. Chem. A 125 (2021) 1384–1390.
[405] B. Alldritt, F. Urtev, N. Oinonen, et al., Comput. Phys. Commun. 273 (2022) 108258.
[406] S.E. Freeney, M.R. Slot, T.S. Gardenier, I. Swart, D. Vanmaekelbergh, ACS Nanosci. Au 2 (2022) 198–224.
[407] B. Verlhac, N. Bachellier, L. Garnier, et al., Science 366 (2019) 623–627.
[408] L. Gross, F. Mohn, P. Liljeroth, et al., Science 324 (2009) 1428–1431.
[409] B. Mallada, A. Gallardo, M. Lamanec, et al., Science 374 (2021) 863–867.
[410] P. Leinen, M. Esders, K.T. Schütt, et al., Sci. Adv. 6 (2020) eabb6987.
[411] I.J. Chen, M. Aapro, A. Kipnis, et al., Nat. Commun. 13 (2022) 7499.
[412] B. Ramsauer, G.J. Simpson, J.J. Cartus, et al., J. Phys. Chem. A 127 (2023) 2041–2050.